


UNIVERSITÁ DEGLI STUDI DI MILANO &
UNIVERSITÁ CATTOLICA DEL SACRO CUORE

SCUOLA DI DOTTORATO IN
FISICA, ASTROFISICA E FISICA APPLICATA

DIPARTIMENTO
MATEMATICA E FISICA

DOTTORATO DI RICERCA IN
FISICA, ASTROFISICA E FISICA APPLICATA
Ciclo XXVI

Time Resolved Optical Measurements on Carbon Nanotubes Structures for Photovoltaic Applications

Settore scientifico disciplinare FIS/03

Coordinatore: Prof. Marco Bersanelli
Tutore: Dott.ssa Stefania Pagliara

Tesi di Dottorato di:
Stefano Ponzoni

Anno Accademico 2013-2014

To my parents

Contents

Introduction and outline

Carbon nanotubes are an allotropic form of carbon that can be viewed as hollow cylinders of graphite sheets. Typical nanotubes diameters are in the nanometer range whilst their lengths can be up to centimeters. They can exist in both their single-walled form (SWCNT), in which only one graphite sheet is rolled along the tube circumference, or in their multi-walled form (MWCNT) which is characterized by the presence of multiple concentrically nested SWCNT. Since from their discovery in 1991 by Iijima [1] carbon nanotubes have been subjected to an intense theoretical and experimental investigation by the scientific community. This interest arises from their unique structural and electronic properties which are intimately related to the high ratio between their lengths and diameters. Carbon nanotubes can be looked as quasi-one dimensional crystals with translational periodicity along the tube axis. Quantum confinement effects along the diameter deeply alter the electronic structure and properties of a carbon nanotube with respect to the ones found in two dimensional graphene or in three dimensional graphite crystals, despite the same sp^2 hybridization state of the chemical bonds. For example carbon nantubes can show a metallic or semiconducting character depending on the unit cell geometry. Perhaps one of the most striking manifestation of the quasi-one dimensionality of SWCNT is the presence of Van Hove singularities in their electronic density of states (DOS). The presence of such peaked structures in the DOS reflects in the optical properties of SWCNT. Typical optical absorption spectra of SWCNT show characteristic peaks due to interband transitions between the Van Hove singularities. Thanks to the similar energy dispersion relations of the valence and conduction states electron-electron correlation effects lead to the formation of excitons which actually dominate the optical absorption properties of SWCNT even at room temperature. Exciton binding energies in the order of 300 meV are common in SWCNT since the electronic screening effects are reduced in quasi-one dimensional systems and exciton transitions can be found even in metallic SWCNT [2]. The excitons transition energies depend on the nanotube diameter and on the unit cell rotational and translational symmetries and can be found within a wide spectral

range from the infrared to the blue part of the visible spectrum. Thanks to these intriguing optical properties carbon nanotubes are currently investigated as possible building blocks for optoelectronic devices. Recently in the quest for overcoming the intrinsic limitations of the conventional Silicon based solar cells Carbon based devices have been proposed. Fullerenes and semiconducting nanocristals donor/acceptor assemblies [3] are investigated as light harvesting elements whilst Graphene has the potentiality to replace the conventional metallic oxides transparent electrodes with its exceptionally high electrical conductivity and wide band transparency [4]. Among the various approaches SWCNT and MWCNT based solar cells are currently investigated and could represent a cheap and viable alternative to the current technology. SWCNT and MWCNT are able to generate photocurrents and their use as light harvesting elements in electrochemical or hybrid solid state devices has already been demonstrated by many investigators. SWCNT can enhance the device light absorbance and extend the useful wavelength range below the Silicon interband absorption threshold and above the wavelengths where surface recombination quenches the efficiency of commercial devices. An alternative approach aims to the replacement of conventional transparent conducting electrodes. Due to the high carriers mobility and long scattering times metallic SWCNT, doped SWCNT or MWCNT could efficiently collect and transport the photoexcited carriers in nanostructured systems. Despite the promising results the processes of charge carriers excitation dissociation and transport in carbon nanotubes and in carbon nanotubes based devices, which occur in an ultrafast time scale, are not fully understood. The main aim of this thesis is to clarify the physical mechanisms underlying these phenomena in view of their importance from both a theoretical standpoint and in optoelectronic devices design. Time resolved pump-probe optical spectroscopy is an invaluable tool for the investigation of the out of equilibrium properties of matter. Its applications range from the real time following of fast reaction dynamics in molecular systems to the study of photoexcited carriers dynamics and photoinduced charge transfer in condensed matter. The ultrafast optical properties of carbon nanotubes are subjected to intensive studies. Despite these efforts a complete and coherent comprehension of the photoexcited carriers dynamics in SWCNT and MWCNT has not been yet reached. The complex exciton radiative and nonradiative relaxation phenomena, as well as their eventual dissociation in free charge carriers, depend on a number of intrinsic and

extrinsic factors such as the tube types, tube bundling and chemical environment. Moreover, at high levels of photoexcitation exciton-exciton interactions became significant and processes such as exciton-exciton annihilation take place. Much of the ongoing experimental efforts focus on the study of the transient dynamics in isolated tubes and the out of equilibrium properties of SWCNT and MWCNT aggregates are not commonly investigated. Even if the these studies proved invaluable for the understanding of dynamic and static optical properties of carbon nanotubes form both a practical and theoretical point of view, we point out that, up to now, in viable optoelectronic devices architectures carbon nanotubes aggregates are used therefore a deeper understanding of the transient properties of nanotubes aggregates is needed. For this reason, in this thesis, we study the carriers dynamics in three different carbon nanotubes systems with potential application in solar cell technology. The outline of this thesis is the following

- In chapter 1 a theoretical overview of carbon nanotubes properties with particular emphasis on their static and transient optical properties is given. The possible applications of carbon nanotubes in solar cell technology are also briefly summarized. The experimental technique and setup is described.

- In chapter 2 the results of transient transmittivity experiments performed on aligned multi walled carbon nanotubes are reported and discussed with the aim of investigate the differences of their electronic structure with respect of the graphite one. This chapter is an adapted version of the article published in the Elsevier journal *Carbon* [5].

- In chapter 3 the results of transient reflectivity experiments performed on aligned single walled carbon nanotubes are reported and discussed with the aim of investigate the role of defects on the transient optical properties and relaxation dynamics. This chapter is an adapted version of the article published in the Elsevier journal *Thin Solid Films* [6] and is an extension of one of our previous articles published in *Carbon* [7].

- In chapter 4 the results of transient transmittivity experiments performed on metallic and semiconducting enriched ultrapure SWCNT films are reported and discussed with the aim of investigate the differences in the

carriers dynamics.

- In chapter 5 the results of transient reflectivity experiments performed on metallic enriched SWCNT/n-silicon hybrid solar cells are reported and discussed with the aim of clarify the role of SWCNT in the light harvesting process and gain information of the carriers dynamics at the interface. This chapter is an adapted version of an article recently submitted to the APS journal *Physical Review Letters*.

Chapter 1

Experimental and theoretical details

1.1 Single walled carbon nanotubes

1.1.1 SWCNT crystal and electronic structure

Single walled carbon nanotubes (SWCNT) can be thought as hollow cylinders of graphene ribbons rolled up along one particular direction. Since their diameters range from 3Åto several nanometers [8] and their lengths are typically in the micrometer or millimeter range, they can be considered as a quasi−one dimensional crystals with translational periodicity along the tube axis. The crystal structure of carbon nanotubes is closely related to the graphene structure. Graphene is single layer of graphite in which each carbon atom forms 3 planar, strong, covalent bond by sp^2 hybridization among s, p_x and p_y orbitals. The σ covalent bond between sp_2 hybridized orbitals is highly directional and the three bonds are equally spaced in their plane by 120 angles, whereby carbon atoms arrange themselves in a hexagonal honeycomb planar lattice with a bond length of 1.42 Å. The unit cell of the graphene honeycomb lattice is spanned by two basis vectors $\vec{a_1}$ and $\vec{a_2}$, of length $|\vec{a_1}| = |\vec{a_2}| = a_0 = 2.461\mathring{A}$ and with a 60 degrees mutual angle. SWCNT are usually labeled in terms of their chiral indices (n_1,n_2) i. e. a pair of integers identifying the chiral vector

$C = n_1\vec{a_1} + n_2\vec{a_2}$along which the graphene ribbon is rolled up. As shown in fig.1.1 in carbon nanotubes, the graphene ribbon is rolled up in such a way that the graphene lattice vector $\vec{C}$ becomes the circumference of the tube.

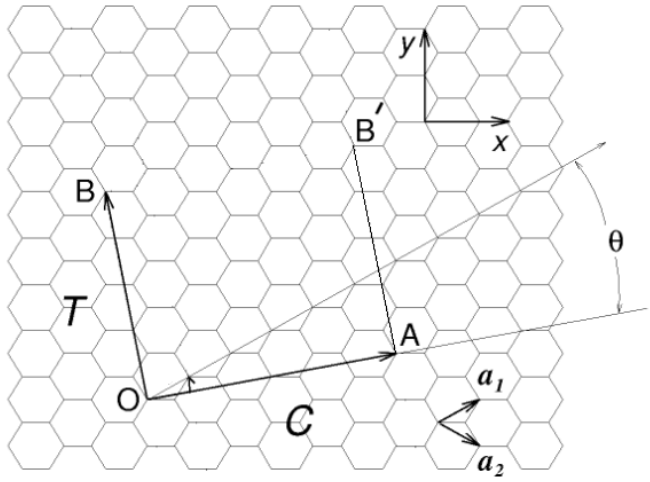

Figure 1.1: Graphene lattice with chiral vector $\overline{OA} = \vec{C}$ for $(n_1, n_2) = (4, 2)$ carbon nanotube. The nanotube axis $\overline{OB}$ is also shown [9].

The chiral vector uniquely defines a particular tube and many properties, like electronic band structure, vary dramatically with it, even for tubes with similar diameters. Due to the six-fold rotational symmetry of the graphene lattice, all the possible SWCNT can be identified with a chiral vector between the (n,0) and the (n,n) directions, being n a positive integer. Tubes with chiral vectors in the latter direction are called armchair tubes whilst tubes with the former chiral vector direction are called zig-zag tubes. All tubes with chiral vectors between these two directions are called chiral nanotubes. The smallest graphene lattice vector $\vec{T}$ perpendicular to $\vec{C}$ defines the translational period along the tube axis and hence the nanotube unit cell length. The translational period can be determined from the chiral indices (n_1,n_2) by

$$\vec{T} = \frac{2n_1 + n_1}{d_r}\vec{a_1} - \frac{2n_1 + n_2}{d_r}\vec{a_2} = t_1\vec{a_1} + t_2\vec{a_2}$$

where d_r is the greatest common divisor between $(2n_1 + n_2)$ and $(2n_2 + n_1)$. $\vec{T}$ varies strongly with chirality and chiral tubes often have a very long unit cell. In a first approximation the electronic structure of SWCNT can be calculated starting from the graphene electronic structure and using the zone-folding approach. This method is essentially based on the confinement of the carriers in a small stripe of graphene. The band structure is found by looking at the energy dispersion relation of an ideal, plane, infinite graphene layer in some particular directions imposed by confinement and nanotube chirality. Along the cylinder wall the σ sp^2 bonds form the hexagonal network while π bonds, from p_z carbon orbital, point perpendicular to the nanotube surface. The σ states are at high energy, with respect to the Fermi energy. The bonding and antibonding π bands cross at the Fermi energy, being responsible for most of the nanotube optical and transport properties. The coincidence of the starting and ending point of the chiral vector on the nanotube surface defines the periodic boundary conditions along its direction for the Bloch wavefunctions. The conditions reads $\vec{K_\perp} \cdot \vec{C} = 2\pi m$ where $\vec{K}_\perp$ is the Bloch electron wavevector along the chiral vector direction, and $m \in Z$. The reciprocal lattice vectors are found, by definition, from $\vec{R}_i \cdot \vec{K}_j = 2\pi\delta_{ij}$ where $\vec{R}_i$ is a direct lattice vector. Therefore the reciprocal lattice vectors for the nanotube unit cell are

$$\begin{cases} \vec{C} \cdot \vec{k}_\perp = 2\pi \\ \vec{C} \cdot \vec{k}_z = 0 \\ \vec{T} \cdot \vec{k}_\perp = 0 \\ \vec{T} \cdot \vec{k}_z = 2\pi \end{cases}$$

where $\vec{k}_z$ is the wavevector along the nanotube axis $\vec{T}$. The solutions, in terms of the graphene reciprocal lattice vectors, $\vec{b}_1$ $\vec{b}_2$, are

$$\vec{k}_\perp = \frac{1}{q}\left(t_1\vec{b}_2 - t_2\vec{b}_1\right) \qquad \vec{k}_z = \frac{1}{q}\left(n_2\vec{b}_1 - n_1\vec{b}_2\right)$$

Where q is the number of graphene hexagonal cells in the nanotube unit cell. $q = \frac{2\left(n_1^2+n_2^2+n_1n_2\right)}{d_R}$ Two wavevectors which differ by a reciprocal lattice vector are equivalent. Since t_1 and t_2, by definition, do not have a common divisor except the unity, the first graphene reciprocal lattice vector that can be constructed from $\vec{k}_\perp$ is $q\vec{k}_\perp = t_1\vec{b}_2 + t_2\vec{b}_1$ and therefore none of the $\mu\vec{k}_\perp$ (

where $\mu = 1...q-1$) are Graphene reciprocal lattice vectors. The q wavevectors $\mu\vec{k}_\perp$ (with $\mu = 0...q-1$) are the nonequivalent and allowed crystal momentum values for the Bloch electrons in the chiral vector direction which arise from the imposed periodic boundary condition. Because of the translational symmetry given by $\vec{T}$, in an ideal endless nanotube, the allowed wavevector along the $\vec{k}_z$ direction are continuous values. The length of nanotube first Brillouin zone along the axis is $\frac{2\pi}{|\vec{T}|}$.

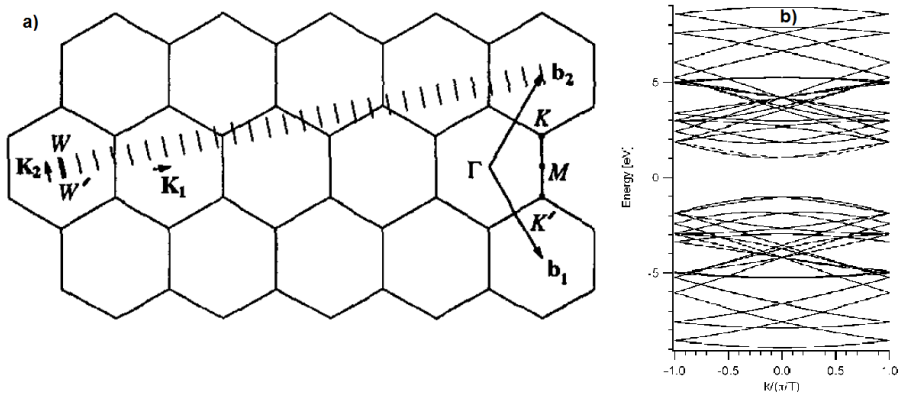

Figure 1.2: (a)WW' is the first Brillouin zone for a (4,2) carbon nanotube. Each parallel segment is at a different allowed value of $\vec{k}_\perp$ [9]. b) Band structure for a $(4,2)$ semiconducting nanotube. $\pi/T = 2.78 \times 10^9\ m^{-1}$. The 28 pairs of bands correspond to the 28 cuts of graphene energy dispersion relation as shown in (a). For the graphene energy dispersion relation the approximation of symmetric π and π^* bands is assumed.

The zone folding approach gives the one dimensional energy dispersion relation of the nanotube by making the substitution of the allowed wavevectors into graphene energy dispersion relation. For the $\pi - \pi^*$ bands we have

$$E_\mu(k) = E_g\left(k\frac{\vec{k}_z}{\left|\vec{k}_z\right|} + \mu\vec{k}_\perp\right)$$

with $\mu = 0...q-1$ and $\frac{\pi}{T} < k < \frac{\pi}{T}$. Each μ value gives a different band. The resulting q-pairs of energy dispersion curves correspond to the cross section of the two dimensional energy surface shown in fig.1.2b, where cuts are made

on the lines $k\frac{\vec{k}_z}{|\vec{k}_z|} + \mu\vec{k}_\perp$. These lines are shown on fig.1.2 for a $(4,2)$ chiral tube. If for a particular (n_1, n_2) tube the cutting line passes through a k-point of the graphene Brillouin zone, its one dimensional energy bands have no energy gap. It can be shown that the density of states at K-points has a finite value for such a nanotube. Therefore it is metallic. If the cutting lines does not pass through a K-point the nanotube is semiconducting, with a finite energy gap between the valence and conduction bands. Using zone folding approach the armchair nanotubes (n, n) are always metallic while the zigzag nanotubes $(n, 0)$ are only metallic when n is a multiple of 3. Supposing that in a generic growth process SWCNTs are evenly produced among a (n_1, n_2) range, it follows that approximately one third are metallic and the other two thirds are semiconducting. Once the band structure of the SWCNT is known we can calculate the electronic density of states $n(E)$. $n(E)dE$ is the number of electronic states per unit volume with energy between E and $E + dE$. The density of states for μ one dimensional electronic bands of the nanotube is given by

$$n(E) = \frac{2}{L}\sum_{\mu}\int \delta(k - k_\mu)\left|\frac{\partial E_\mu(k)}{\partial k}\right|^{-1} dk$$

where k_μ are the roots of equation $E - E_\mu(k_\mu) = 0$ and L is the length of the 1-D Brillouin zone. $\left|\frac{\partial E_\mu(k)}{\partial k}\right|^{-1}$ diverges for every stationary point of the 1-D energy dispersion relation giving rise to the Van-Hove singularities. In the real case the density of states do not diverge however it is still very high at Van-Hove singularities points and therefore it dominates many physical properties as the optical absorption spectrum of the CNT, in particular optical absorption probability will be very high if the energy of incoming photons matches an allowed transition between singularities. The zone folding approach totally neglect the effect of the tube curved wall. One of the effects of the curved wall is the reduction of the interatomic distance for atoms with different azimuthal positions. For example the mutual distance of two atoms at opposite side of the CNT wall is reduced to d, while it is $\pi d/2$ on the unwrapped graphene sheet. Moreover quantum mechanical and symmetry arguments showing that, on a curved wall, the graphene σ states can partially mix with π states and form a new hybrid bond with partial sp^2 and partial sp^3 character. This effect made some changes at the zone-folding nanotube band structure and, for example, more sophisti-

cated calculation based on the DFT approach shows that, at low temperature, only armchair nanotubes maintain metallic properties. [10]. Additional deviation from the approximate zone-folding band structure can be due to the tube curvature along its axis and also from intertube interactions. In particular due to the Van der Walls forces SWCNT tend to arrange themselves in bundles with a two dimensional triangular lattice and with diameters between 10 an 20 nm (see ref [10, 11]). The bundling lead to an energy dispersion perpendicular to the nanotube axis as well.

1.1.2 Optical properties of SWCNT

In fig.1.3 a typical optical absorption spectrum for bundled SWCNT is shown. The spectra is characterized by a series of peaks which depends on the tubes chiralities above a featureless background.

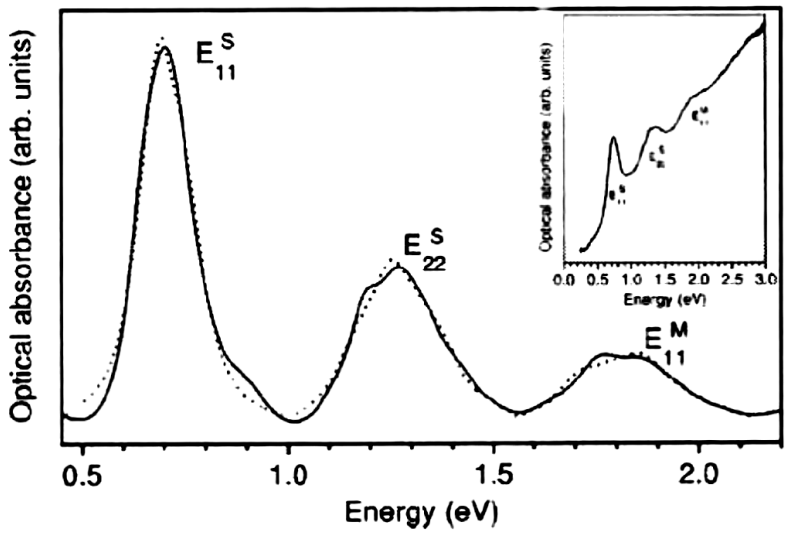

Figure 1.3: Optical absorption spectra from carbon nanotube bundle. The inset show the raw data before linear background subtraction [12].

As reported earlier, in an independent electron approximation, the optical properties of carbon nanotubes are dominated by interband transitions between

the valence and the conduction states arsing from the π and the π^* bands. In static optical spectroscopy measurements the transmittance or the reflectance of a sample is usually measured. If the sample reflectance can be neglected the transmittance is defined as the ratio

$$T(\omega) = \frac{I(\omega)}{I_0(\omega)} = e^{-\alpha z}$$

where I and I_0 are the transmitted and the incident light intensity at frequency ω, α is the absorption coefficient and z the distance covered by the light beam inside the sample. From transmittance measurements is possible to extract the optical absorption coefficient of the material which is related to the complex dielectric function $\epsilon = \epsilon_1 + i\epsilon_2$ by the relation

$$\alpha = \frac{\epsilon_2 \omega}{nc}$$

where n is the refractive index and c is the speed of light in vacuum. The imaginary part of the dielectric function, $\epsilon_2(\omega)$, plays a pivotal role in the interpretation of the transmittance and reflectance spectra. From $\epsilon_2(\omega)$ the real part of the dielectric function, $\epsilon_1(\omega)$, can be calculated using the Kramers-Kroenig transformations [13] and therefore the complete transmittance or reflectance spectrum can be predicted. The quantum theory of dielectric functions, in the dipole approximation, gives an expression for ϵ_2 that depends on the energy dispersion, $E_v(k)$ $E_c(k)$, of the valence states and the conduction states. [14] This expression written in Gaussian units reads

$$\epsilon_2 = \left(\frac{2\pi e}{m\omega}\right)^2 \sum_{c,v} \sum_{k} |M_{cv}(k)|^2 \, \delta\left(E_c(k) - E_v(k) - \hbar\omega\right)$$

This expression also depends on transition matrix element $M_{cv}(k)$. Neglecting the wavevector dependence of the matrix element and use the Dirac delta properties we get

$$\epsilon_2 = \left(\frac{2\pi e}{m\omega}\right)^2 |M_{cv}|^2 \int \frac{dS'_k}{\nabla_k \left(E_c(k) - E_v(k)\right)}$$

where the integral is done on the k-space surface defined by $E_c(k) - E_v(k) = \hbar\omega$. The surface integral is the joint density of states, $n_j(\omega)$. $n_j(E)dE$ represents the

number of electronic state per unit volume with energy between E and $E + dE$ that fulfill the energy conservation condition in an optical transition of energy $E = \hbar\omega$. Moreover due to the low momentum of optical photons with respect to the electron crystal momentum, and neglecting phonon-mediated second order process, only direct interbad transitions ($\Delta k \approx 0$) give rise to strong contribution in the surface integrals. Because of the Van Hove singularities in the electronic density of states, the joint density of states of carbon nanotubes is characterized by the presence of intense, sharp peaks. The dipole matrix element $M_{cv}(k)$ give a set of symmetry induced selection rules that depend on the relative polarization of the electric field vector with respect to the nanotube axis. It can be shown that for optical transitions, between valence and conduction bands, the total angular momentum conservation allows only transitions that fulfill the rules

$$\Delta\mu = 0 \qquad \text{for } \vec{E}||\vec{z}$$
$$\Delta\mu = \pm 1 \qquad \text{for } \vec{E}\perp\vec{z}$$

where $\vec{z}$ is the nanotube axis direction and μ is the band index given by zone folding method [10]. Theoretical considerations starting from a tight-binding description of graphene together with the additional constrains imposed by the SWCNT unit cell symmetry to the nantube wavefunctions show that the transition matrix elements for $\Delta\mu = \pm 1$ are, in general, smaller than $\Delta\mu = 0$ ones [15]. An additional quenching of the perpendicular-polarized optical absorption is due to the screening of the light electric field by the polarization charges induced on the CNT wall. This effect can be understood in a static approximation considering an infinitely long cylinder in an external electric field. For a field perpendicular to the cylinder axis charges are induced on the cylinder walls and the resulting polarization vector opposes the external electric field reducing its effective value [16,17]. These arguments lead to consider only optical transitions between the same valence and conduction subbands ($\Delta\mu = 0$) in the interpretation of static absorption spectra of single wall carbon nanotubes. These transitions are centered at the Van-Hove singularity energy where the joint density of states blow up. The allowed transitions between the same index subbands are labeled as E_{ii} with $i = 1..n$, where the index i increases with the transition energy. The optical transitions theory described so far do not take into account the coulombic interaction between the electon-hole pair generated upon absorption of a photon. Despite the high expected values for the on-axis

dielectric constant the quasi-one dimensional nature of SWCNT leads to an enhancement of the coulomb interaction between the electron-hole pair. This effect can be thought as due to the electric field between the electron-hole pairs which extends outside the tube boundary and thus is less screened than in a three dimensional solid [18]. The interaction between the electron and the hole pairs give rise to exciton levels which lie below the zone-folding band edges. A large theoretical and experimental effort has been undertaken in the past years in order to clarify the effect of the excitons in the optical properties of carbon nanotubes. It is now well established that the exciton binding energies, E_X, in SWCNT is remarkably high, being in the range of hundreds of mV. Exciton in carbon nanotubes are stable even at room temperature and are responsible for the sharp features observed in the optical absorption spectra which therefore takes place at an energy lower than the bandgp by E_X (fig.1.3). It is worth to note that even the majority of the spectral weight in the absorption spectrum is due to exciton transitions the interband transitions of electron holes pairs across the band edges is still possible, as remarkably demonstrated by A. D. Mohite et al. in [19] In this experiment the authors using a displacement photocurrent technique were able to detect the spectral signature of the exciton transition at ≈ 0.6 eV in a ≈ 1.3 diameter tube, together with the signature of the direct photoexcitation of carriers in the electron-hole continuum. (Fig.1.4).

The experiment used a ITO/SWCNT/SiO_2/p-Si multilayer structure in order to detect the photocurrent due to the direct excitation of electron-holes pairs in the SWCNT upon tunable pulsed-light illumination. In case of exciton excitation the photocurrent signal can be detected only if an external potential difference between the ITO and the p-Si contacts is applied. The applied field leads to the exciton dissociation via tunneling of the electrons in the SWCNT conduction band, giving rise to an external voltage dependent photocurrent signal. The energy bandgap for the interband transition is in the order of 0.9 eV and the exciton binding energy turns out to be $E_X \approx 0.3$eV. The excitonic transitions labeled as E_{22} (in a manner reminiscent of the transitions between zone-folding sub-bands) is a transition to the first exciton excited state and its energy level is embedded in the conduction band continuum such as the other higher lying excitonic states. The residual spectral weight of the direct interband excitation is responsible for part of the broad background in the optical absorption spectra of SWCNT.

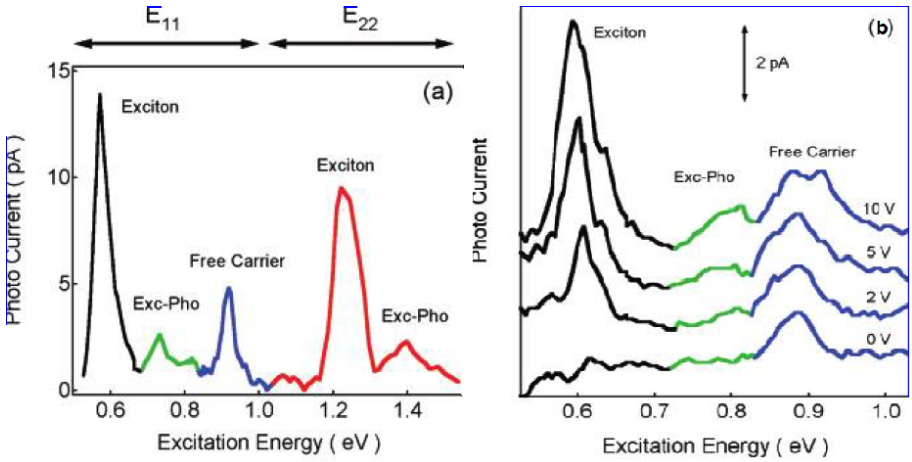

Figure 1.4: a) Photocurrent versus excitation energy for an individual nanotube measured with 20 V dc bias across the ITO/SWCNT/SiO_2/p-Si multylayer by Mohite *et al* b) Photocurrent versus excitation energy measured by Mohite *et al* near the E11 exciton transition for bias ranging from 0 to 10 V. The curves are offset for clarity. Adapted from [19].

1.2 Multi walled carbon nanotubes

Multi walled carbon nanotubes are essentially nested single walled carbon nanotubes. They are usually characterized by a large overall diameter which can be in the order of tens of nanometers. The large diameter tend to reduce their aspect ratio, i. e. the ratio between the diameter and the MWCNT tube length. The aspect ratio reduction leads to lower quantum confinement effects and MWCNT properties are usually considered similar to those of graphite. Anyway a number of differences between the physical properties of MWCNT and the graphene or graphite properties have emerged in the past few years. In particular MWCNT have been found to be able to generate a photocurrent upon visible light illumination [20]. This phenomenon has no direct analog in graphite or in graphene and can be ascribed to the complex interplay between the nested shell of the MWCNT. From the point of view of the electronic structure in the tight-binding model and gradient approximation [21], the result is that the

superposition of the coaxial nanotubes makes VHSs peaks to be smeared out and MWCNT are therefore similar to the highly oriented graphite (HOPG). This similarity is supported by the featureless optical absorption spectra usually found on large diameter MWCNT. DFT calculations, which take in account electron-electron interaction, performed on a few wall MWCNT shows variations of the DOS reminiscent of the VHS in the parent SWCNT as reported in fig.1.5.

Moreover in [22] the interaction between the two shells of a Double Walled Carbon Nanotube is considered and a static charge transfer from the outer shell to the inner one is found. Measurements of photocurrent and of electron energy loss spectra show that the electronic density of MWCNT is considerably different from that of HOPG and suggest the presence of singularities, due to the reduced dimensionality [20]. Other results from photoluminescence and static transmission measurements have been reported in which the VHSs seem to play a role in the MWCNT optical response pointing to remarkable differences between the HOPG and the MWCNT optical properties [23, 24].

1.3 Carbon nanotube based photovoltaics

Due to their peculiar electronic properties, their chemical stability and the large surface area carbon nanotubes are intensively investigated as possible components in nanostructured light energy harvesting assemblies. Early attempts using a photochemical cell demonstrate the capability of carbon nanotubes to generate a photocurrent upon light illumination [25] i.e. the possibility to generate electron-holes pairs and the availability of these carriers to undergo charge separation and transport processes. In the device builted by Barazzouk [25] (which is schematized in 1.6a, adapted from [25]) a carbon nanotube layer is deposited onto a transparent conducting electrode which is part of a photochemical cell. The cell electrolyte is a regenerative redox couple iodide/triiodide in an acetonitrile solution. The electrolyte provides the conductivity between the SWCNT film and a platinum counter electrode and also act as a photoexcited carriers scavenger. It is found by the investigators that a cathodic photocurrent is prompted generated by this cell upon light illumination. In fig.1.6b the external quantum efficiency, EQE (or equivalently the IPCE) spectra of the photocell is also reported. The EQE is defined as the percent ratio between the incident number of photons on the photocell area and the number of collected electron-

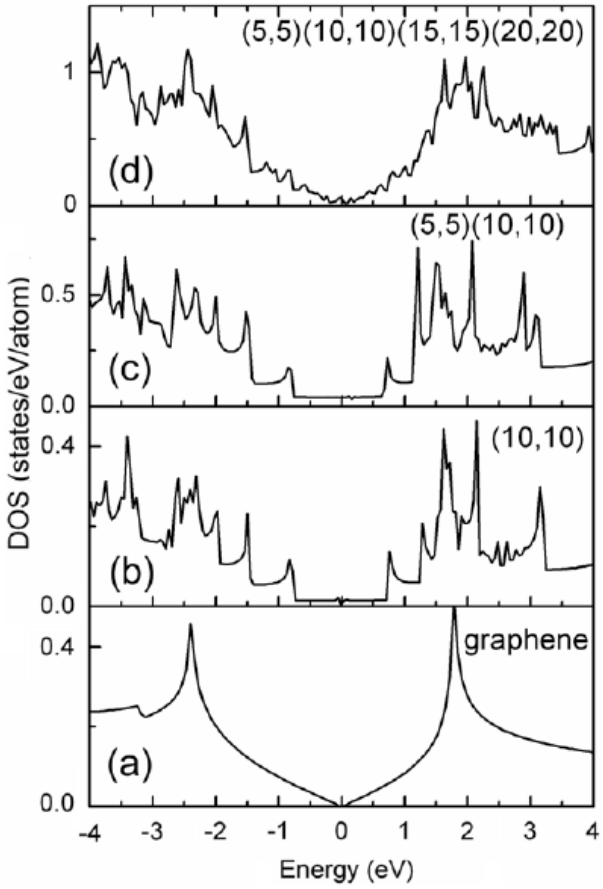

Figure 1.5: Electronic DOS calculated for a graphene sheet (a), a (10, 10) SWCNT (b), a (5, 5) (10, 10) DWCNT (c) and a (5, 5) (10, 10) (15, 15) (20, 20) 4WCNT (d). From [20].

holes pairs at the cell output terminals keeping a constant null potential across them.

The detected quantum efficiency was quite low, being at most at 0.15 %, but demonstrated the possibility of using carbon nanotubes as active light harvesting elements. Soon after a large number of investigator started testing carbon

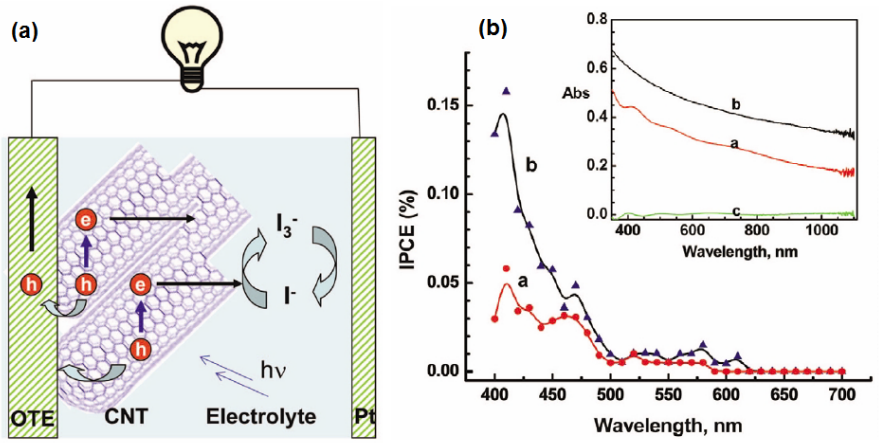

Figure 1.6: a) SWCNT electrochemical solar cell schematics. b) EQE spectra for the SWCNT based solar cell. The higher EQE (black line) is collected on a different devices with SnO_2 nanoparticles deposited onto the SWCNT film Adapted from [25].

nanotubes in a variety of devices and configuration. Up to now the research in CNT based solar devices mainly focuses on carbon nanotubes as substitutes for transparent and conductive electrodes, as charge collectors from light absorbing semiconducting polymers or dyes in organic solar cells and as light absorbing components. Thin film of metallic or doped semiconducting SWCNT are good candidates to replace the conducting transparent metallic oxides in both organic or inorganic solar cells due to their superior conductivity. In particular metallic carbon nanotubes show the capability to withstand large current densities due to their low electron-phonon coupling [26] and to have large carriers mobility [27]. Semiconducting carbon nanotubes can be turned metallic via molecular charge transfer dopants such as NOH_3 and other acceptor or donor molecules. The effect of the dopant adsorption is to inject or withdraw electrons from the SWCNT leading to a significant shift of the Fermi level up to the electrons or the holes VHS. The Fermi level shift plays also the important role of reducing the spectral weight of the excitonic transitions thought a state-filling effect. This is responsible for a dramatic change of the optical absorption spectra of doped SWCNT so both an increased conductivity and an increased transparency in the visible part

of the spectrum can be simultaneously archived. [28]. The exceptionally high carriers mobility in SWCNT makes them also possible candidates for charge acceptors and collectors in polymer based photovoltaic devices. These devices are constituted by a polymer/SWCNT bulk heterojunction and the photocurrent generation is based on exciton dissociation via interfacial charge transfer. The driving force of this process is the overall energy gain in the exciton dissociation through electron transfer from the LUMO of the photoexcited polymer to the LUMO of the semiconducting SWCNT or, similarly, through hole transfer from the HOMO of the excited SWCNT towards the HOMO of the polymer ([3] and references therein). Another possibility is to use the SWCNT themselves as photon absorbing elements because of their strong and tunable spectral response. In fig 1.7 the optical transition energy of SWCNT is displayed in funcion of their diameter (Kataura plot), together with the solar light spectrum. It is evident that an opportune mixture of SWCNT could, in principle, absorb energy in almost the whole solar spectrum.

In order to directly use SWCNT as light harvesting elements the exciton binding energy must be overcome by some mechanism and the resulting electron-holes pairs separated and collected. To this end several architectures have been proposed, among which the use of type-II heterojunctions between the SWCNT and another charge accepting materials such as C_{60} or Si-nanocrystals. ([3] and references therein)The underlying working mechanism of these devices is similar to the one of SWCNT/semiconducting polymers heterojunctions and is based on a band offset, at the heterojunction interface between the donor SWCNT and an electron acceptor, exceeding the exciton binding energy. This difference leads to the spontaneous breaking of the exciton and at the transfer of the electrons from the SWCNT to the acceptor.

Recently also CNT/n-Silicon heterojunction have been proposed [29]. In these devices a thin layer of carbon nanotubes is casted on a n-silicon wafer in order to create an heterojunction similar to the conventional p-n silicon solar cell. These devices have shown an exceptionally high power conversion efficiency up to 15 %. In fig.1.8 a schematic diagram of the heterojunction is shown together with its band scheme and the proposed mechanism for carriers generation and transport [29].

At first glance, charge separation will occur due to the high built-in electric field which inject an hole drift current in the nanotube layer and electrons in

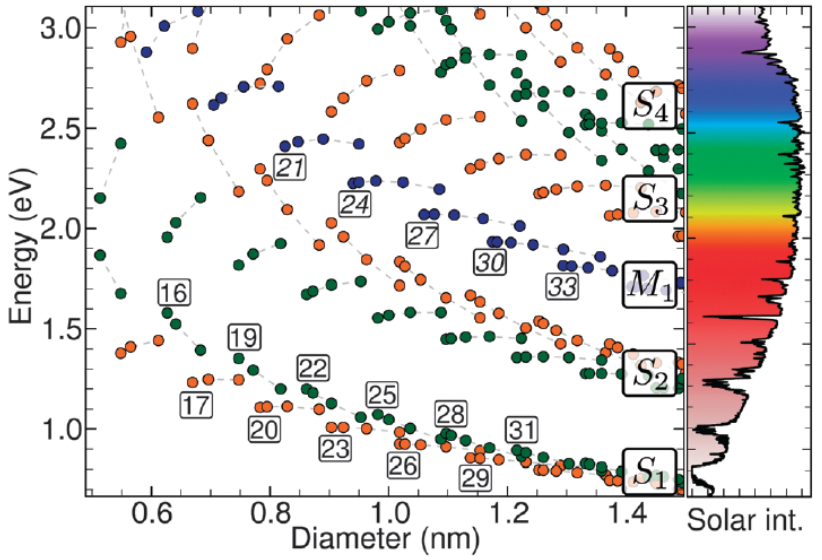

Figure 1.7: Optical transitions energies versus the SWCNT diameter. The labels S_n or M_n indicate the subband index for the optical transitions in semiconducting or metallic tubes. It is worth to note that even considering excitonic effects the overall dependence on tube diameter still holds and only a rigid shift of the transitions energies occurs. In the right inset the solar radiation spectra at the Earth surface is displayed. From [3].

the n-Silicon substrate. This architecture combines the high diffusion length of Silicon with the high mobility of carbon nanotubes. Moreover the production process is easily scalable and the production cost is lower than for conventional p-n cells. Despite these promising result the underlying charge separation mechanism is not fully understood and the role of the carbon nanotubes as light absorbing elements or simply as a transparent conductive electrode is still matter of debate [30]. Recent EQE measurements on semiconducting SWCNT/n-Si cells have demonstrated photocurrent generation on an extended spectral range with respect to a commercial p-n silicon cell [31]. This point toward an active role of the SWCNT in the carriers generation and to the possibility of efficient exciton dissociation even in these simple devices. Since the processes of charge

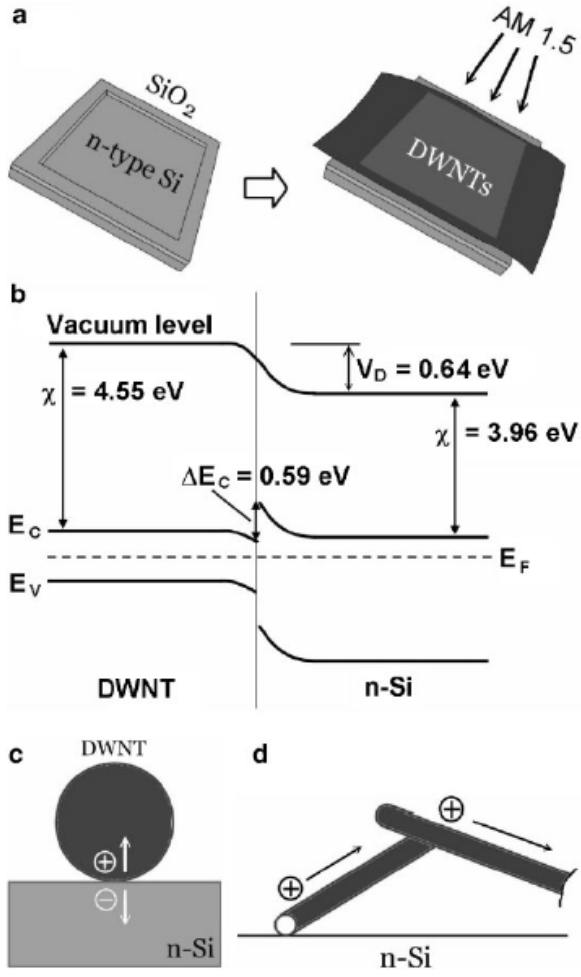

Figure 1.8: a) Illustration of the double walled CNT/n-Si cell. b) Band scheme at the heterojunction interface. c) and d) illustration of the carriers separation and transport. From [29].

generation and separation occurs on an ultrafast time scale in chapter five we use time-resolved pump-probe optical spectroscopy to investigate the underlying working mechanism of a metallic enriched SWCNT/n-Si heterojunction.

1.4 Ultrafast spectroscopy of carbon nanotubes

Ultrafast optical spectroscopy techniques are widely used to study the dynamics and the kinetics of scattering and relaxation processes of excited carriers in solid state systems. These processes typically take place in a few femtosecond to some picosecond time interval, so they are outside from time scale accessible to conventional electronic instruments. In order to overcome this limitation pump-probe techniques are employed. In time resolved pump-probe optical experiments an intense light pulse pumps the sample in an excited state whilst a weaker pulse probes the transient variation of its optical properties, such as transmittivity or reflectivity, at a selectable delays from the excitation. The capability of generating a few femtoseconds light pluses, with mode-locked lasers, and to precisely control their relative delays allows to follow the transient relaxation overcoming the detector speed limit. It can be shown that in a time resolved transient transmittivity experiment, performed on centrosimmetric materials, the detected signal I_{pp} is dominated by the third order nonlinear polarization of the medium $P^{(3)}$.

$$I_{PP}\left(\omega_{pr},\tau\right)=2\omega_{pr}Im\int_{-\infty}^{+\infty}E_{pr}\left(t'\right)P^{3}\left(\tau,t'\right)dt' \tag{1.1}$$

where ω_{pr} is the frequency of the probe pulse, E_{pr} is its electric field envelope function and τ is the relative time delay between the pump and the probe pulses. If the processes involving the carrier relaxation dynamics are slower than the dephasing times of the polarization the optical transients are due to a variation of the frequency dependent absorption coefficient $\alpha\left(\omega\right)$ and thus to a variation of the complex part of the dielectric function ϵ_2.[1] Using the density matrix

[1]The absorption coefficient depends explicitly on the refractive index n which contains also the real part of the dielectric function. Anyway the real and the complex part of the dielectric function are linked together by the Kramers-Kroenig transformations which prescribes the causality of the optical process. Even if these transformations written in the usual form [13] holds only for linear systems a modified version can be obtained for nonlinear systems as well (see for example [32]).

formalism and considering only transitions between two particular states $|1\rangle$ and $|2\rangle$ the variation reads

$$\Delta\epsilon_2(\omega) = \frac{2\pi e}{m_e\omega}|M_{21}|^2\left[(1-\rho_{22})\Delta\rho_{11} - \rho_{11}\Delta\rho_{22}\right] \tag{1.2}$$

where M_{21} is the transition dipole matrix element and ρ_{ii} are the population of the two states. In case of small population of the excited state ($\rho_{11} << \rho_{22}$) the variation of the absorption coefficient is

$$\Delta\alpha(\omega) = \frac{2\pi e}{m_e n(\omega) c}|M_{21}|^2\left[\Delta\rho_{11} - \Delta\rho_{22}\right] \tag{1.3}$$

where the variation of the refractive index is also neglected. This incoherent limit of the absorption variation is frequently used as starting point for the interpretation of transient absorption spectra [33]. This formula describes a saturation of the optical transition and give an overall reduction of the absorption coefficient commonly referred as photobleaching. If more than two states are involved an additional optical transition may arise from the first excited state to another state at an higher energy. This process gives a transient increase of the absorption coefficient at the probe frequency, commonly refereed as photoabsorption. (Fig.1.9)

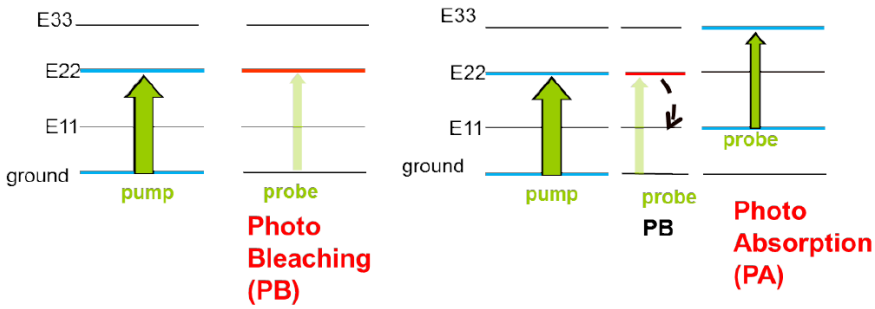

Figure 1.9: Schematic rapresentation of a photobleaching and a photoabsorption process in a 4 level system.

In carbon nanotubes the presence of strong exciton effects justify the use a multilevel approximation. Resonant excitation of higher lying excitonic states, such as E_{22} is followed by a rapid (< 100 fs) intersubband relaxation towards

the lowest exciton state, due to the strong interaction with phonons [34, 35]. It has also been proposed that the exciton levels in SWCNT belongs to an exciton manifold which will give an additional intersubband relaxation channel [36]. The intersubband relaxation dynamics was directly measured in isolated carbon nanotubes by Manzoni *et al.* [37] using a tunable 10 fs pulsed laser systems. The ground state relaxation dynamics was found in the order of 1 ps. This results conflicts with the relaxation times measured with time resolved photoluminescence experiments which are in the order of tens of nanoseconds. The huge difference can be due to nonradiative relaxation processes detectable only by the former technique.

If the excitation intensity is sufficiently high exciton-exciton interaction can take place. The interaction of two excitons can lead to an exciton-exciton annihilation process (EEA) in which one of the exciton rapidly relax transferring it energy to the other and promoting it to an higher excited state. The signature of this process was detected by several researchers using photoluminescence spectroscopy, and time resolved transient transmittivity [38, 39] In case of EEA the excite state population n_{ex}, being a two body process, follow a simple nonlinear rate equation which reads

$$\frac{dn_{ex}}{dt} = -\gamma n_{ex}^2 (t)$$

where γ is a time independent rate constant from which an annihilation rate in the order of 0.8 ps^{-1} can be calculated [38]. Other researcher fund an explicit time dependence for the rate constant γ in the form $\gamma = \gamma_0 t^{-1/2}$. This time dependance is expected from a diffusion limited EEA process in one dimensional systems [40] but the discrepancies between the two relaxation dynamics are still matter of debate [33].

On the other side metallic carbon nanotubes (MSWCNT) present both strong exciton and interband transitions and their transient optical properties are somewhat less studied. The excited carriers dynamics in this systems where investigated primary via time resolved photoemission spectroscopy [41] which can directly track the electron distribution and its relaxation kinetic in the vicinity of the Fermi level. Since the semiconducting tubes do not contribute to the electronic population at the fermi level this technique can, in principle, single out the dynamics of the metallic tubes even in a sample with the usual mix of semiconducting and metallic species. From the differential photoemission

spectra Hertel and Moos [41] found that electron-electron scattering processes in MSWCNT rapidly thermalize the photoexcited electron population on a 200 fs time scale. for longer delays the slower electron-phonon scattering processes cool the electron population until the thermal equilibrium with the lattice is reached. The coupling of a thermalized electron population with the lattice was described using the two-temperature model [42]

$$\begin{aligned} C_e \frac{dT_e}{dt} &= \nabla \left(k \nabla T_e \right) - H \left(T_e, T_l \right) + S \left(t \right) \\ C_l \frac{dT_l}{dt} &= H \left(T_e, T_l \right) \end{aligned} \quad . \tag{1.4}$$

Where $S\left(t\right)$ is the laser pulse energy, T_e and T_l are the electron and the lattice temperature, k is the electronic thermal conductivity, C_e and C_l are the electronic and lattice heat capacities. The coupling term $H\left(T_e, T_l\right)$ describes the interaction between the electronic and the phononic degrees of freedom which, for electronic and phononic temperature similar or smaller than the Debye temperature Θ_d reads [43]

$$H \left(T_e, T_l \right) = \frac{144 \zeta \left(5 \right) k_b \gamma}{h} \frac{\lambda}{\Theta_d^2} \left(T_e^5 - T_l^5 \right) \tag{1.5}$$

where ζ is the Reimann zeta function, k_b the Boltzmann constant, γ the electronic heat capacity coefficient, h the Planck constant and λ the electron-phonon mass enhancement factor. λ is related to the electron-phonon scattering time τ_{e-ph} [44]which for MSWCNT turns out to be in the order of 15 ps. This long scattering time is consistent with the extraordinary current-carrying capacity of MSWCNT and their long ballistic electron mean free path [45].

1.5 Experimental Setup

For the experiments reported in this thesis we employ two different pump-probe setups. The first one is a low fluence one-color setup. The second one is a fixed-probe energy tunable-pump energy setup operating in an high fluence regime. Both systems can operate in a reflectivity or transmttivity configuration. Due to the different configurations used in our experiments in this section we only report a general description of the setups an the actual configuration and settings of the laser systems will be specified in each chapter.

1.5.1 One-color low fluence setup

The low fuence setup is based on a mira 900 Ti:Sapphire mode-locked laser oscillator. The output pulses wavelength is centered at 795 nm (1.55 eV) and the FWHM time pulsewidth is of about 120 fs, with an output energy of 50 nJ per pulse. The laser oscillator is coupled with an intracavity APE pulseswitch which allow to regulate the repetition rate from 54.3 MHz to single shot. The pump pulse fluence can be regulated in a 0.1 - 1.0 mJ/cm^2 range with a conventional half-waveplate polarizer assembly. In fig.1.10 a schematic diagram of the experimental line is reported.

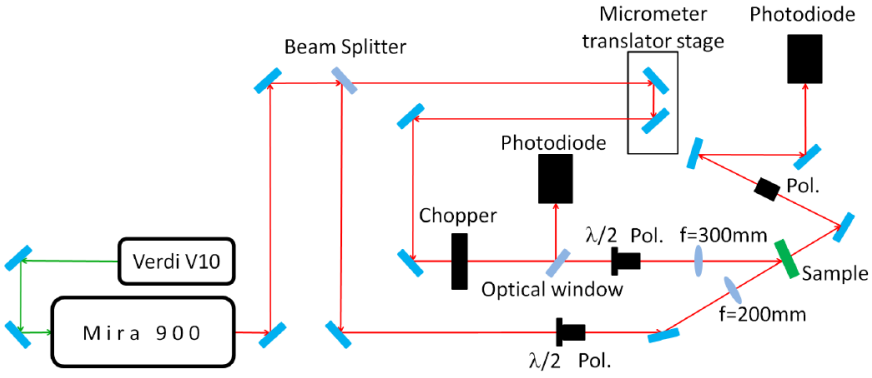

Figure 1.10: Schematic representation of the low fluence time resolved transmittivity setup

The spot sizes at the sample surface are 50 μm and 15 μm for the pump and the probe beams respectively and the minimum delay achievable with a the computer controlled delay stage is 0.66 fs. Both reflectivity or transmittivity signals can be acquired alternatively with Thorlabs det 210 A photodiode using a standard lock-in technique. The signal phase reference for the lock-in amplifier (signal recovery) is generated with a photodiode placed on a small reflex the pump beam after the optical chopper. Both the static transmittivity (or reflectivity) signal and its variation is extracted by the lock-in amplifier from the DC component of the probe beam and its in phase component. The high repetition rate (usually set at 540 KHz in order to avoid sample heating effects)

and the high chopping frequency of the pump beam ensure a signal resolution in the order of $\Delta I/I \approx 5 \times 10^{-6}$.

1.5.2 Two-color high fluence setup

The light source of this setup is an α-line amplified Ti:Sapphire laser system. The pulse wavelength is centered around 795 nm with a temporal width about 150 fs FWHM and an energy of ≈600 μJ per pulse. The repetition rate is 1 KHz, therefore the average output power is 0.6 W, and the peak power is 4×10^9 W. The 70 % of the output beam is directed in a traveling wave optical parametric amplifier (TOPAS), manufactured by Light Conversion, whist the remaining 30 % is further attenuated and used as a probe beam. The TOPAS output frequency can be tuned from 1150 to 1600 nm with an average output power of nearly 40 mW. In order to further extend the tunable range a pair of BBO nonlinear crystal are employed. With this configuration the pump photon energy can be tuned in the 575-800 nm and in the 290-400 nm intervals. Unwanted components at the fundamental TOPAS output frequencies are eliminated using a dispersive element and a set of filters. The pump fluence range depends on the used configuration but values between 2.5 and 20 mJ/cm^2 are commonly achievable. In fig.1.11 a schematic representation of the optical line is reported.

The spot sizes at the sample position are 100 μm and 50 μm for the pump and the probe respectively. Due to the low repetition rate of laser source the pump beam is chopped at 500 Hz and a boxcar integration technique is used to retrieve both the static value of the transmittivity (or reflectivity) signal and its variation. The instrument resolution is in the order of $\Delta I/I \approx 1 \times 10^{-4}$.

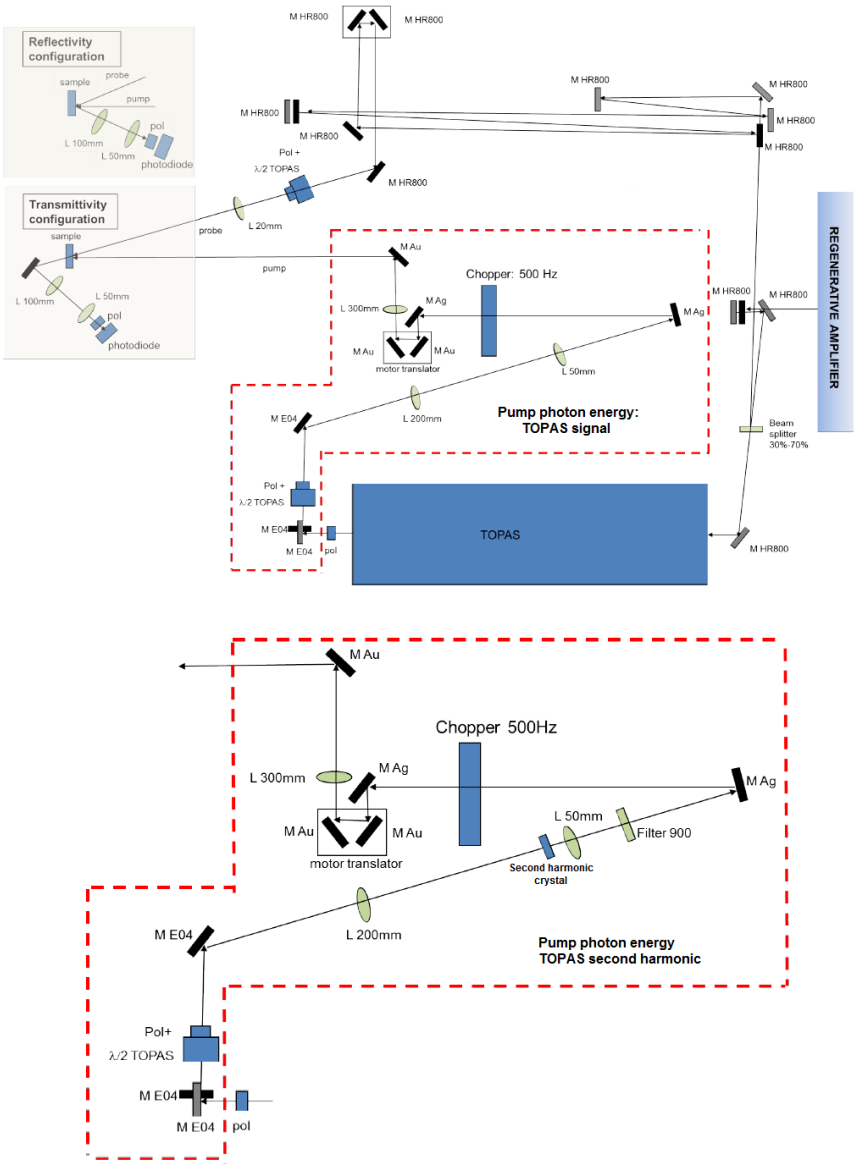

Figure 1.11: Schematic representation of the high fluence time resolved setup

Chapter 2

Probing the electronic structure of multi-walled carbon nanotubes by transient optical transmittivity

In this section an adapted version of the paper published in [5] is reported.

2.1 Abstract

High-resolution time resolved transmittivity measurements on horizontally aligned free-standing multi-walled carbon nanotubes reveal a different electronic transient behavior from that of graphite. This difference is ascribed to the presence of discrete energy states in the multishell carbon nanotube electronic structure. Probe polarization dependence suggests that the optical transitions involve definite selection rules. The origin of these states is discussed and a rate equation model is proposed to rationalize our findings.

2.2 Introduction

An understanding of the optical transitions and the underlying electronic structure of carbon nanotubes is of central importance to their characterization and integration within numerous opto-electronic applications. For single-walled carbon nanotubes (SWCNTs) the density of states, which is dependent on the nanotube chirality and dominated by multiple Van Hove singularities (VHSs), is well defined. The excitonic nature of the optical transitions has been explored in some detail [46], [37], [21]. Conversely, multi-walled carbon nanotubes (MWCNTs) represent a much more challenging electronic system and, as yet, no coherent understanding of their properties has been presented. The presence of multiple, concentrically nested nanotubes, each with differing chirality, greatly complicates the electronic structure of MWCNTs. Theoretical and experimental studies predict similarities between the electronic properties of highly oriented pyrolytic graphite (HOPG) and MWCNTs, however conflicting reports also suggest the presence of discrete states which make MWCNTs more similar to SWCNTs [47], [48]. Multiple shells enhance the electrical conductivity due to several distinct transport pathways [49–52]. Moreover a larger absorption cross-section results with high spectral absorbance over the entire visible spectrum [53–55]. MWCNTs are consequently extremely promising in photovoltaic applications, in particular when used in conjunction with various electron donor groups [51], [56]. Higher incident-photon-to-current efficiencies (IPCE) have been observed for MWCNTs compared to SWCNTs [51]. Key to such future applications, however, is a more detailed understanding of their underlying electronic and optical properties. Here, we employ time-resolved optical spectroscopy to critically compare the transient optical response of MWCNTs and HOPG. Highly aligned suspended MWCNT films have been employed to negate detrimental substrate contributions. Horizontal alignment ensures that the probed electronic structure is unaffected by variable sample features, such as nanotube curvature [7]. By performing monochromatic transient transmittivity experiments, in the near-infra-red (790 nm), we demonstrate the presence of discrete energy states in the MWCNT electronic structure. In this framework, the transient response is characterized by photo-bleaching (PB) and photo-absorption (PA) channels, as well as non-linear effects that we control by tuning the probe polarization. The dependence on the probe polarization un-

ambiguously shows that these states have a well- defined symmetry and that the optical transitions between these states respect precise selection rules. Two different interpretations are proposed and discussed to account for these states: the first concerns the presence of clusters in the nanotube walls. The second one hypothesizes a MWCNT electronic structure similar to that of SWCNTs and, although many questions remain still open, it appears more consistent with the experimental results here reported.

2.3 Experimental

2.3.1 sample preparation

The carbon nanotubes (CNTs) investigated were aligned, free-standing MWCNTs, synthesized by thermal chemical vapor deposition in a commercially available, cold-wall reactor (Aixtron Ltd.). Vertically aligned nanotube forests were grown on thermally oxidized Si substrates (200 nm SiO_2) coated with 10 nm Al_2O_x (magnetron sputtered) and 1 nm Fe (thermally evaporated). Bilayer catalysts were heated to 700 ^oC (5^oC/s) under 8 sccm C_2H_2 diluted in 192 sccm H_2 (25 mbar). Aligned, free-standing MWCNT thin films were fabricated by solid-state pulling at a rate of $\sim 10^{-2}$ m/s, as illustrated in fig.2.1a, employing a similar technique as reported elsewhere [57].

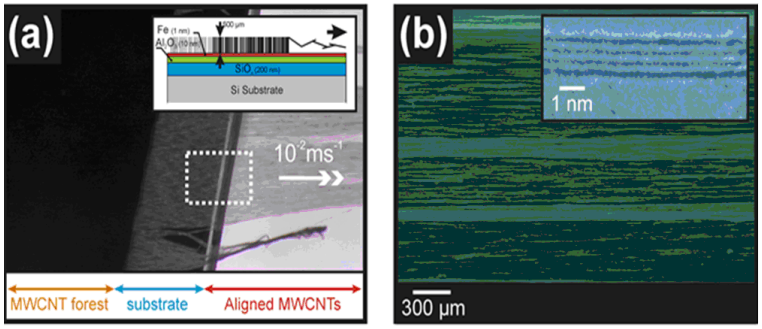

Figure 2.1: Optical micrograph of a vertically aligned MWCNT forest during membrane solid-state pulling. Insert: Cross-section schematic of a catalyst wafer.

MWCNT bundles were pulled mechanically from a pristine source nanotube

forest, several hundred micrometers in length, allowing us to obtain continuous yarns / thin films of high-purity MWCNTs. Fig.2.1a shows an optical micrograph of a vertically aligned MWCNT forest during membrane solid-state pulling. To ensure the probed characteristics are associated implicitly with the MWCNTs, no post-growth chemical processing was performed. In the inset, a cross-section schematic of a catalyst wafer is shown. Figure 2.1b shows a scanning electron micrograph (SEM) of the aligned, free-standing MWCNT film. High-resolution transmission electron microscopy (HR-TEM) clearly shows multiple graphitized side-walls (Fig.2.1, inset and Fig.2.2) with negligible amorphous carbon deposits and minimal bamboo-like sectioning.

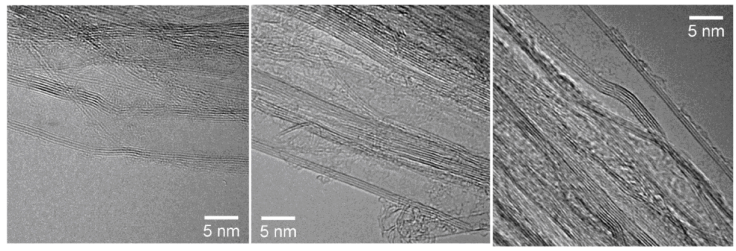

Figure 2.2: Typical high-resolution transmission electron micrographs highlighting the high-degree of graphitization and general absence of a-C

The as-grown MWCNTs were approximately 500 μm in length, 25 ± 13 (Standard Deviation) nm in diameter and consisted of typically 2-5 graphitic walls. In figure 2.3a the histograms, showing the outer diameter and number of graphitic walls (Inset) are reported. Highlighted areas denote the mean 1 S.D. Figure 2.3b shows a typical Raman spectra (Renishaw InVia, 633 nm excitation, 3 mW) of the film at multiple positions, evidencing the high sample uniformity.

X-ray photoelectron spectroscopy (XPS), Raman spectroscopy and HR-TEM confirm the high graphitic quality of the MWCNTs. Ultra violet photoelectron spectroscopy (UPS) was acquired in a ultra-high vacuum chamber using a conventional He discharge lamp ($h\nu = 21.2$ eV) and a hemispherical electron energy analyzer. The electron energy distribution curves were measured at room temperature in normal emission geometry, with an overall instrumental energy resolution of 0.1 eV. The binding energy scales are referred to the Fermi level of a gold polycrystal foil.

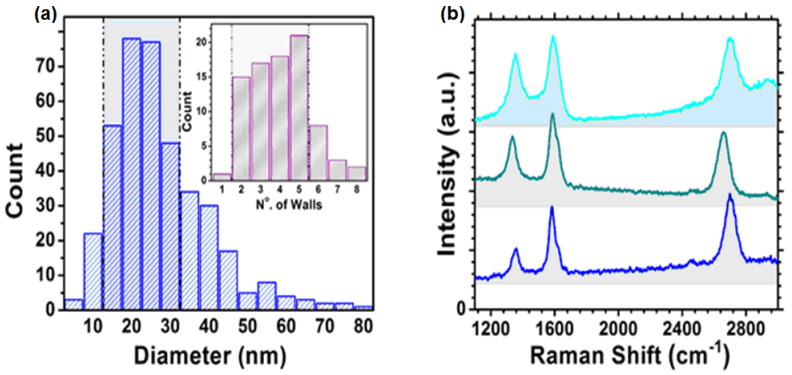

Figure 2.3: (a) Histograms showing the outer diameter and number of graphitic walls (Inset). Highlighted areas denote the mean 1 S.D. (b) Raman spectra (633 nm, 3 mW) of an as-grown MWCNT forest (top) and an extruded membrane (middle, bottom). Negligible variation was noted in the acquired spectra across samples.

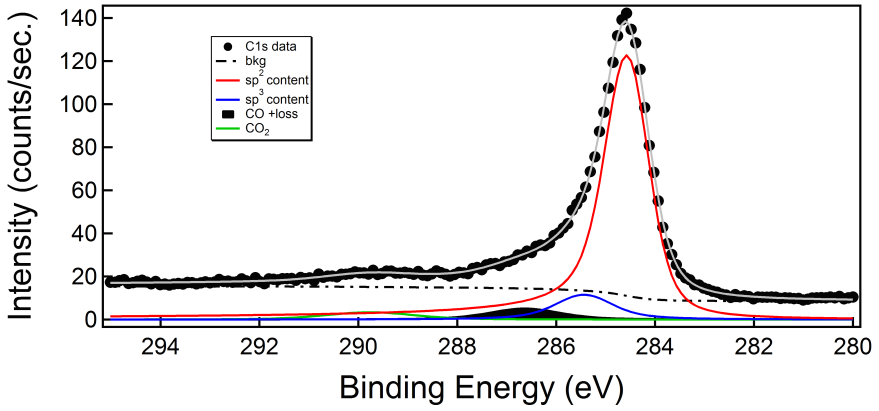

Figure 2.4: X-ray photoelectron spectroscopy and fits of the sp^2 (red), sp^3 (blue), CO (circle) and CO_2 (green) peak in the C1s peak (square).

In Fig.2.4, the C1s photoemission spectrum is shown. The fitting of the C 1s peak suggests an sp^3/sp^2 concentration ratio thereby allowing us to evaluate an upper limit of the sp^3 content [58]. The C 1s has been fitted using a

Shirley background and four components with Doniach-Sunjic lineshapes, corresponding to sp^2 C (284.5 eV), sp^3 C (285.4 eV), C-O and/or losses (286.7eV) and CO_2 (289.9eV). The lorentzian linewidth was fixed at 0.28 eV, compatible with literature values [58], while the Gaussian widths were defined as free-fitting parameters. The only component with a non-null asymmetry was that corresponding to sp^2. Our results show that the sp^3 content strongly depends on the asymmetry parameter (α) of the sp^2 component, and we were be able to obtain good fit results in an asymmetry range which includes metallic CNTs (α of 0.19) [59] and pure HOPG (α of 0.075-0.099) [60–62]. The corresponding sp^3content in these two extreme cases were, respectively, 14% and 8%. As a consequence from XPS data we can only assess that the upper limit of the sp^3 content, corresponding to the HOPG asymmetry parameter, is about 14% (fitting components shown in Fig.2.4). To refine this estimate, detailed Raman spectra were measured at 485 nm, 532 nm, 633 nm and 785 nm (x50 aperture, incident power $<$ 5mW). Figure 2.5 shows a representative Raman spectra, collected with 633 nm, 3 mW, a x20 aperture and a probe size of 1.2 μm. The two spectra suggest an I(D)/I(G) ratio of 0.40.1 (1 S.D.). For 532 nm excitation I(D)/I(G) = 0.270.05 (1 S.D.). The position of the G peak is 1578 cm^{-1}. By comparison with Fig.2.5(b), this enables us to affirm that the sp^3 content tends more toward 0% than XPS would suggest.

Considering Fig.2.5(b) [63] and the previously determined upper limit of the sp^3 content of 14% we can assert that the MWCNTs presented in this study fall the highlighted graphitic stage 1 (highlighted blue), where the sp^3 content tends toward zero and the dimension of the sp^2 clusters, dependent on the number of graphene lattice defects, is large. Detailed Raman analysis shows narrow G-peak full-width half-maxima and linear dispersion of the G and D peaks, collected at various excitation wavelengths (485, 532, 633, 785 nm). Such features are consistent with the Raman signatures of highly graphitic MWCNTs and confirms the negligible sp3 content. The mean diameter of the sp^2 clusters (10 nm) disagrees with the hypothesis of confinement effects at the origin of electronic states or gap formation in the MWCNT band structure [64].

Free-standing, well-aligned horizontal MWCNTs permit strict control over the relative angles between the MWCNTs and the incident polarization, whilst simultaneously avoiding detrimental substrate optical interference effects. Herein perpendicular-polarized is defined as the light polarization perpendicular to the

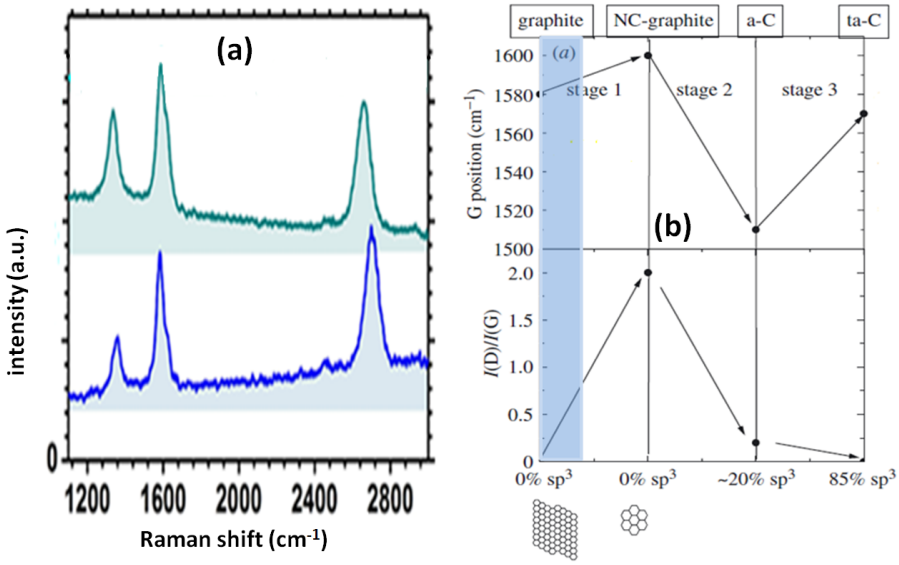

Figure 2.5: (a) Typical 633 nm Raman spectra. (b) Percentual sp^3 content as a function of I(D)/I(G) and G peak position, from [63].

MWCNT long-axis and parallel-polarized as the polarization parallel to the MWCNT long-axis.

2.3.2 Laser System

Samples were optically excited using a Ti: Sapphire cavity-dumped, mode-locked laser oscillator. Output pulses were centered at 790 nm (1.55 eV) with a full-width half-maximum of 120 fs. The output energy was 50 nJ (per pulse) with a variable repetition rate from 54.3 MHz to a single shot. Mean heating effects were obviated using tunable repetition rates. The pump fluence ranged from 0.1 to 0.8 mJ/cm^2. Low fluence measurements were obtained at 540 kHz to maximize the signal-to-noise ratio. A lock-in acquisition technique was employed to provide high resolution in the transient transmittivity signal (ΔT/T).

2.4 Results and discussion

It is known that in MWCNTs the presence of different nanotubes, each with different diameter and chirality, smooths the VHSs, resulting in an electronic structure similar to that of the HOPG [21] [48]. This is in agreement with static absorption measurements, performed using an ultraviolet-visible-near infrared spectrometer (Fig.2.6), where no particular absorption peaks, characteristic of the VHSs, are evident, in agreement with a HOPG-like electronic structure.

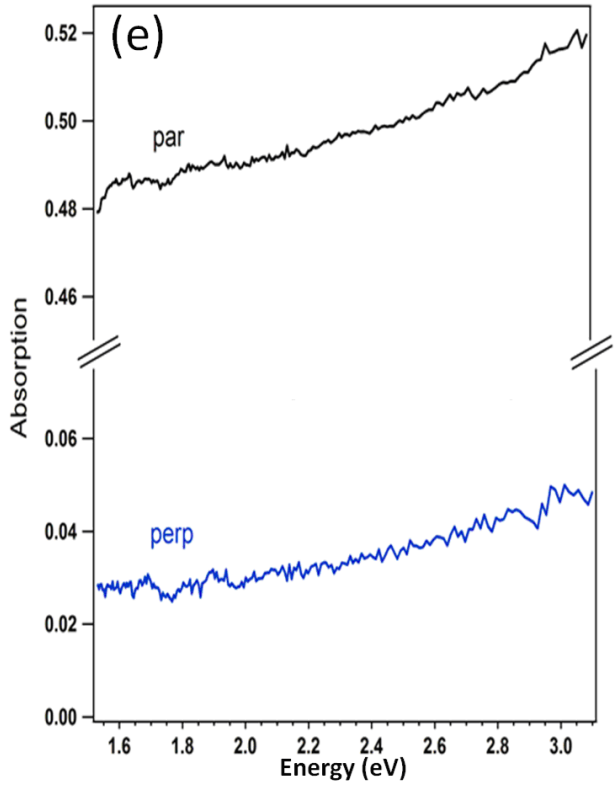

Figure 2.6: Aligned MWCNTs static absorption as a function of energy and light polarization parallel (par) or perpendicular (perp) to the tubes alignment axis

The absorption data confirms the alignment of our MWCNTs. When the

incident polarization is parallel to the MWCNT long-axis (denoted par), the absorption is larger than in the perpendicular case (denoted perp).

In order to compare the transient electronic behavior of MWCNTs and HOPG, we have performed monochromatic transient transmittivity (ΔT/T) measurements, shown in Fig.2.7, where the pump and the probe photon energy is 1.55 eV and the pump fluence is fixed at 0.25 mJ/cm^2($\approx 10^{15}$ photons/cm^2).

Figure 2.7a shows the transient transmittivity collected by rotating the probe polarization, from parallel to perpendicular to the MWCNT long-axis, with the pump polarization fixed parallel to the MWCNT long-axis. To clearly evidence the probe polarization dependence of the transient signal, in Fig.2.7a ΔT/T data have been normalized to the first ΔT/T maximum. The shape of the transient response is unmodified by the normalization procedure. Two dynamics dominate the MWCNT response. The first, observed at short delay times (<150 fs), is positive and consistent with a photo-bleaching (PB), previously observed in HOPG and SWCNTs [7, 37, 46, 65, 66]. Charge carriers are promoted by the pump from the ground state to an excited state and the absorption of the probe, at the same photon energy, decreases due to final state filling, with a corresponding enhancement of the probe transient transmission. The intensity of this PB feature, for a constant pump fluence, is affected by coherence effects that strongly enhance the signal when the pump and probe polarizations are parallel to one another [67, 68]. The second dynamic (>150 fs) occurs over a temporal range independent of any coherence effects and, unlike the first, depends strongly on the probe polarization. In particular, the sign of this second response is negative when the probe polarization is parallel to the MWCNT long-axis and positive when perpendicular to it. By rotating the probe polarization relative to the MWCNT long-axis, from 0 (parallel-polarized) to 90 (perpendicular-polarized), the second dynamic changes sign - from negative to positive. The change of sign depends exclusively on the probe polarization. To exclude a pump polarization contribution, in Fig.2.7b while keeping a fixed parallel-polarized probe, the pump polarization is rotated (at 10 increments), obtaining a variation of the second dynamic intensity. The magnitude of this second dynamic is consistently negative for all pump polarizations. Similarly, fixing the probe perpendicular-polarization (Fig.2.7c), the rotation of the pump polarization changes only the intensity of the second dynamic, maintaining the positive sign. The optical response with parallel-polarized probe (Fig.2.8a) has

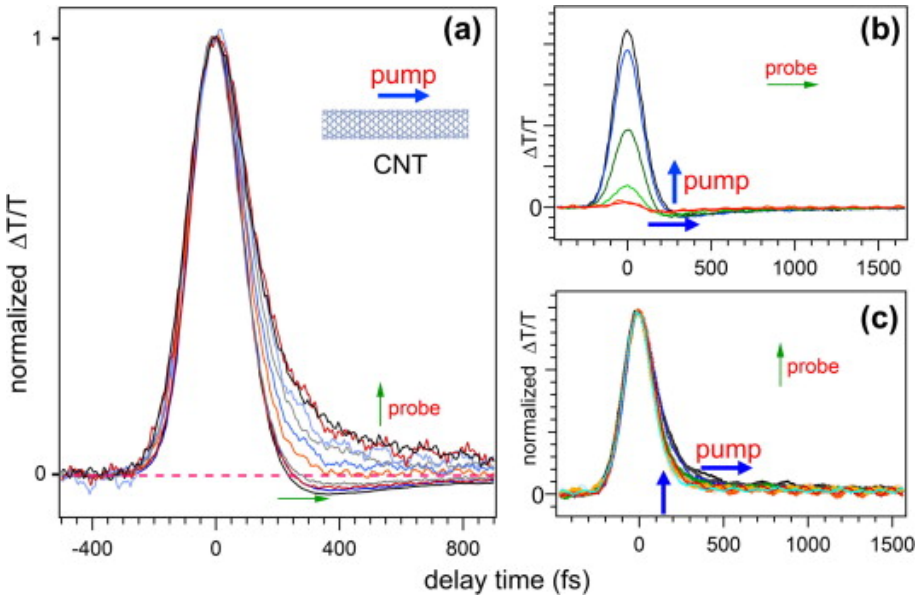

Figure 2.7: (a) Monochromatic normalized transient transmittivity (ΔT/T), at 1.55 eV, collected with a pump polarization parallel to the MWCNTs long-axis and the probe polarization varying from parallel to perpendicular. (Incident fluence = 0.25 mJ/cm^2). The sign of the second dynamic depends only on the probe polarization and varies continuously from negative (probe polarization parallel to MWCNT long-axis) to positive (probe polarization perpendicular to MWCNT long-axis). Spectra are normalized to the maximum response of the positive signal ($1.3\text{x}10^{-3}$), excluding coherence-artifacts. Non-normalized dependence of ΔT/T with probe polarization parallel (b) and perpendicular (c) to the MWCNT long-axis (alignment axis), respectively. The pump polarization rotation does not affect the sign of the second dynamic. The oscillations in (b) and (c) have an intensity below the instrument sensitivity ($\Delta T/T \approx 10^{-6}$).

been interpolated by two exponential functions, convoluted with a Gaussian representing the pulse temporal width. While the first dynamic, affected by the presence of the coherent artifact, is very fast (40 $\pm$ 15 fs), the second is an order of magnitude slower (400 $\pm$ 100 fs). The analysis of the optical response with perpendicular-polarized probe (Fig.2.8b), performed with the same fitting

procedure, gives a similarly fast first dynamics (40 ± 15 fs), while the second is 1.0 ± 0.1 ps.

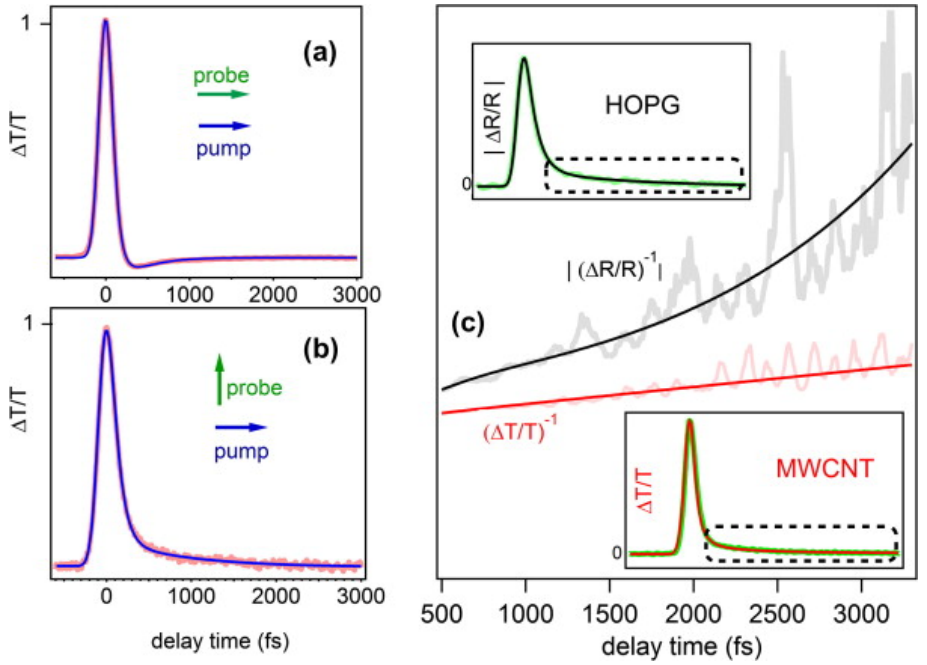

Figure 2.8: (a) ΔT/T for pump and probe polarizations parallel to the MWCNT long-axis. Fit (blue) of the experimental data (red), as modeled by eq.(2.3). (b) ΔT/T for pump polarization parallel and probe polarization perpendicular to the MWCNT long-axis. Fit (blue) of the experimental data (red) as modeled by eq.(2.3). For pump fluences 0.25 mJ/cm^2, the intensity of the second dynamic tracks the laser pump absorption that depends on the angle between the laser polarization and the MWCNT long-axis [53]. (c) Top: $\left|(\Delta R/R)^{-1}\right|$ of the HOPG (inverse of the fit extracted from the inset) as a function of the delay time (0.5-2.5 ps). Bottom: $(\Delta T/T)^{-1}$ of MWCNTs (inverse of the fit extracted from the inset) as a function of the delay time (0.5-2.5 ps). Note the linearity. Spectra collected with pump polarization parallel and probe polarization perpendicular to the MWCNTs long-axis.

The surprising dependence of the second dynamic on the probe polarization allows us to grasp, for the first time, the difference between the tran-

sient behavior of MWCNTs and HOPG. While the positive PB response, in fact, appears consistent with the HOPG-like behavior, the negative response (probe polarization parallel to MWCNT long-axis, Fig.2.8a) excludes a HOPG-like relaxation channel. With a parallel-polarized pulse only the component of the dielectric constant parallel to the MWCNT long-axis is probed, corresponding to the component of the HOPG dielectric constant perpendicular to the graphite c-axis [53, 69, 70]. Under equivalent experimental conditions, the HOPG transient response reveals only PB channels. Two exponential decays, ascribed to electron-electron and electron-phonon relaxation, in agreement with the two temperatures model [71–73], are, in fact, measured in the transient reflectivity signal (Fig.2.8c (top)). Under different experimental conditions a negative dynamic has also been reported in HOPG and ascribed to intra-band transitions (Drude model). For observing these intra-band transitions in HOPG and graphene layers, the probe photon energy is usually in the terahertz range [74–78]. In the high pump fluence regime, oscillations have been observed in the HOPG transient signal and ascribed to structural deformation of the inter-plane separation due to strongly-coupled-optical-phonons [79, 80]. However, such structural deformation can be excluded in MWCNTs since structural oscillations of the graphitic walls, observed in SWCNTs, depend strongly on the pump polarization and not on the probe polarization, as revealed in Fig.2.7. Moreover, the period of these oscillations is fast [65,81,82]. This surprising and significant difference between the transient behavior of MWCNTs and HOPG is also confirmed by the pump-probe delay dependence of the MWCNT inverse transient transmittivity ($(\Delta T/T)^{-1}$) in the range of the positive second dynamics (probe polarization perpendicular to the MWCNT long-axis, Fig.2.8b). In Figure 2.8c, the pump-probe delay dependence of the absolute value of the HOPG inverse transient reflectivity ($(\Delta R/R)^{-1}$, top) is shown together with the MWCNT $(\Delta T/T)^{-1}$ (bottom). The linear dependence, shown in Fig.2.8c (bottom), for MWCNTs suggests the non-linear character of the second dynamic. For example, the existence of a quadratic dependence implies the following relation [39, 83, 84]:

$$\frac{dN}{dt} \propto n^2 \tag{2.1}$$

and consequently:

$$(\frac{\Delta T}{T})^{-1} \propto \Delta t \tag{2.2}$$

where N is the photo-excited carriers density population and Δt is the delay time between pump and probe pulse. The linear behavior (Fig.2.8c (bottom)) of the MWCNT transient response, for delay times > 500 fs, reveals the non-linear character of the second dynamic, when the probe is perpendicular-polarized. On the contrary, the non-linear HOPG dependence of $|(\Delta R/R)|^{-1}$ on the pump-probe delay (Fig.2.8c (top)), confirms that the two dynamics in the HOPG transient signal are consistent with the two-temperature model. We assume here, as suggested by Fig.2.8c, that the second dynamic of MWCNTs was a second order process.

This unexpected difference in the transient behavior of MWCNTs and HOPG can be explained by considering localized electronic states. The presence of discrete levels in the MWCNT electronic structure permits also to justify the negative dynamic. Charge carriers, photo-excited by the pump in a previously well-defined unoccupied state, are promoted from this energy state to a higher one by the probe, resulting in a decrease of the transient transmittivity of the probe (negative signal). This process is known in literature as PA effect. At the same time, the second positive dynamic can be ascribed to a re-filling of an unoccupied state by second order processes. To account for the transient optical behavior, we propose a model of the involved optical transitions based on three discrete electronic states, as illustrated in Fig.2.9.

The pump excites ground state carriers (E_0), to a higher state (E_2), that within a few tens of femtoseconds decays to lower energy state (E_1). The probe pulse at the same pump photon energy (1.55 eV), when parallel-polarized with respect to the tube axis, reveals firstly a PB due to the filling of E_2, then, for longer delay times, promotes electrons from E_1 to a higher state (E_3). In the transient transmission spectra, this last process corresponds to an enhancement of the probe absorption (PA) thereby producing the negative ΔT/T response (Fig 2.9a and Fig.2.9b). When the probe polarization is perpendicular to the MWCNT long-axis, the probe reveals two PB channels. Charge carries are promoted by the pump from the ground state to E_2 (first PB) that relaxes within 100 fs from E_2 to E_1. The probe then, for longer delay times, reveals a second PB of E_0-E_2 due to a re-population of E_2 by second order processes

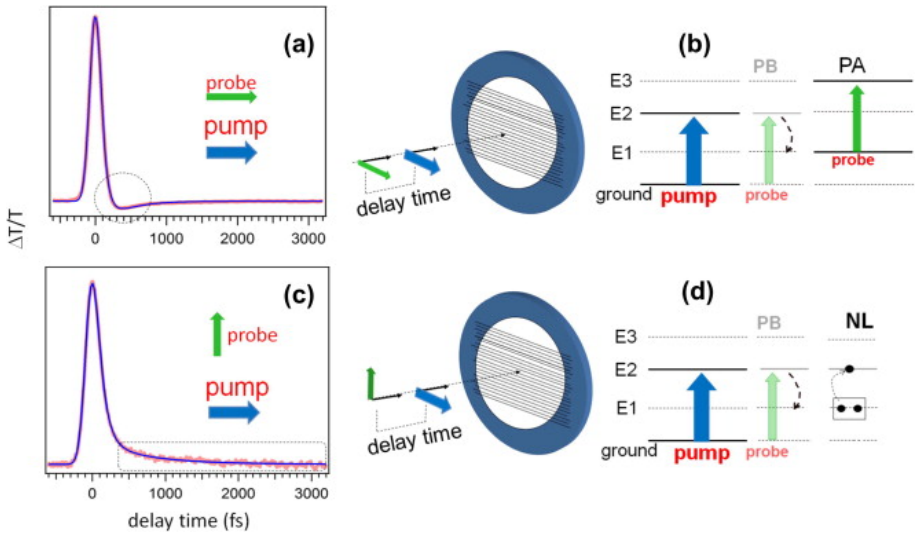

Figure 2.9: (a) $\Delta T/T$ for pump and probe polarizations parallel to the MWCNT long-axis. Fit (blue) of the experimental data (red), as modeled by eq.3. (b) Schematic of the relaxation channels (PB, and PA) as rationalized in the proposed model. (c) As in (a), $\Delta T/T$ signal (red) and fitting (blue) for pump polarization parallel and probe polarization perpendicular to the MWCNT long-axis. (d) Schematic of the relaxation channels (PB and non linear process).

(Fig 2.9c and Fig.2.9d). The strong dependence of the second dynamic on the probe polarization unambiguously suggests that the relaxation processes involve localized energy states with a well-defined symmetry [10,85] and that the optical transitions between these states observe precise selection rules. The PA channel is quenched when the probe is perpendicular-polarized. On the contrary, in this configuration, due to the high pump fluence ($10^{14}-10^{15}$ photons/cm^2) and to the long E_1 decay time (few picoseconds [10]), second order processes are favored thereby repopulating E_2. These second order processes increase the transmittivity of the probe resulting in a second PB channel. The choice of three localized energy states (E_1, E_2, E_3) is in accord with the analysis of the decay times. The PA implies a transition of the photo-excited carriers to a higher state. However, the decay time of the first state, filled by the pump,

is really very fast ($<$ 100 fs) and is inconsistent with the PA relaxation time (hundreds of fs). Therefore a third energy state, with a longer decay time, must be considered as a starting level for PA. To better rationalize our findings, we propose a rate equation model to interpret the relaxation processes depicted in Fig.2.9. The temporal evolution of the photo-excited carriers on the E_2 state (N_2) and on the E_1 (N_1) is then determined by:

$$\begin{cases} \frac{dN_2}{dt} = A \cdot G(t) - B \cdot N_2 + \frac{C}{2} \cdot N_1^2 \\ \frac{dN_1}{dt} = B \cdot N_2 - D \cdot N_1 - C \cdot N_1^2 \end{cases} \tag{2.3}$$

where E $_2$ is populated by the Gaussian pump $G(t) = (\sigma\sqrt{2\pi})^{-1} e^{-\frac{t^2}{2\sigma}}$ and depopulated by the $-BN$ term with B^{-1} corresponding to the N_2 decay time ($E_2 \rightarrow E_1$). The $C \cdot N_1^2/2$ term represents the second order process able to populate the E_2 state starting from E_1. In agreement with the first rate equation, E_1 is populated by the electron relaxation from E_2 (BN_2) and depopulated by the relaxation on the ground state ($-D \cdot N_1$) and second order processes ($-C \cdot N_1^2$). The $\Delta T/T$ signal has been interpolated, in a non-perturbative approach, via the expression:

$$\frac{\Delta T}{T} \propto N_2 - \alpha_{PA} \cdot N_1 \tag{2.4}$$

where α_{PA} is linearly proportional to the magnitude of the PA. The transient responses, given in Fig.2.9a and Fig.2.9c, for the parallel- and perpendicular-polarized probe, are well interpolated by the proposed model (blue line fit, red line data). The C parameter, that represents the second order process weight, was fixed as the pump fluence did not change throughout the measurements. The mean fitted B^{-1} value, for the different spectra, is 60 ± 20 fs. For the perpendicular-polarized probe spectra, the D^{-1} decay time is a few picoseconds, corresponding to the long decay of the lower E_1 state. In the case of parallel-polarized probe spectra (with negative PA dynamics), D^{-1} is a few hundred of femtoseconds.

In Fig.2.10, the fitted α_{PA} value, representing the PA weight, is shown as a function of the angle between the probe polarization and MWCNT long-axis. $\alpha_{PA} = 0$ when the angle is 90^o, as the selection rule prevents PA. Increasing the component of the probe polarization along the MWCNT long-axis, angle $<$ 45, the PA, again in agreement with the dipole selection rules, begins to increase, reaching the maximum value when the polarization direction is along

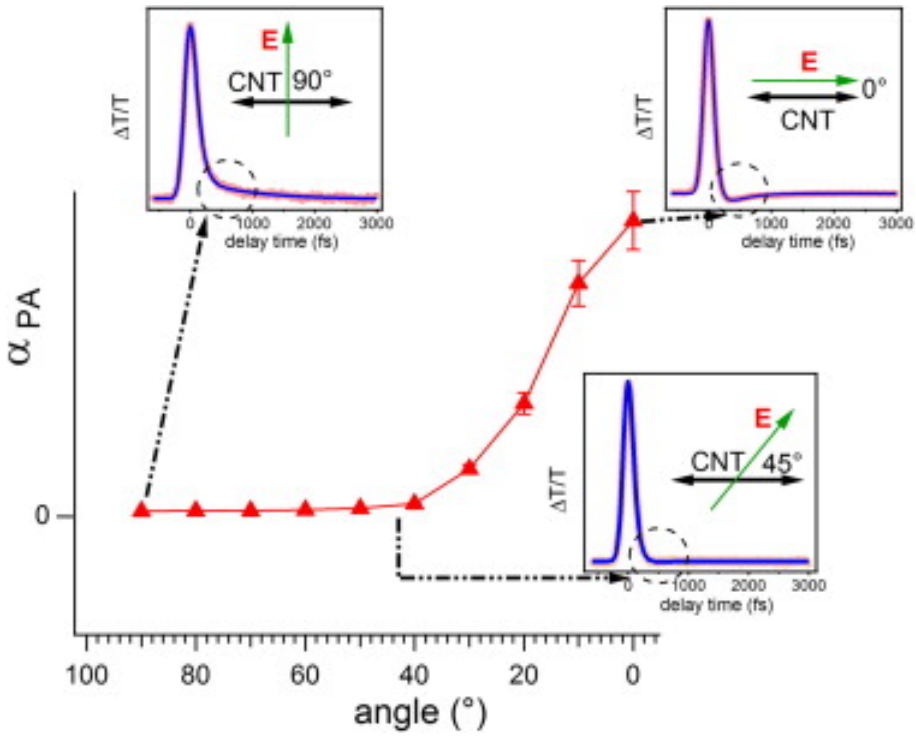

Figure 2.10: PA coefficient, α_{PA}, (eq.3, eq.4) as a function of the angle between the probe polarization and the MWCNT long-axis. When the probe polarization is perpendicular, PA is quenched (top left inset). PA becomes non-zero around 45^o (bottom right inset) and reaches a maximum when the probe polarization is parallel (top right inset).

the MWCNT long-axis. To further elucidate the PA promotion mechanism, rather than the non-linear mechanism, in the second dynamic, in Fig.2.11a the dependence of the PA channel on the pump fluence (top-left inset) is shown by fixing the probe polarization parallel to the MWCNT long-axis.

By increasing the fluence, saturation is clearly noted, as highlighted in more detail in Fig.2.11b where the PA (maximum) versus the pump fluence is plotted. This saturation effect can be explained by considering that, as the non-linear

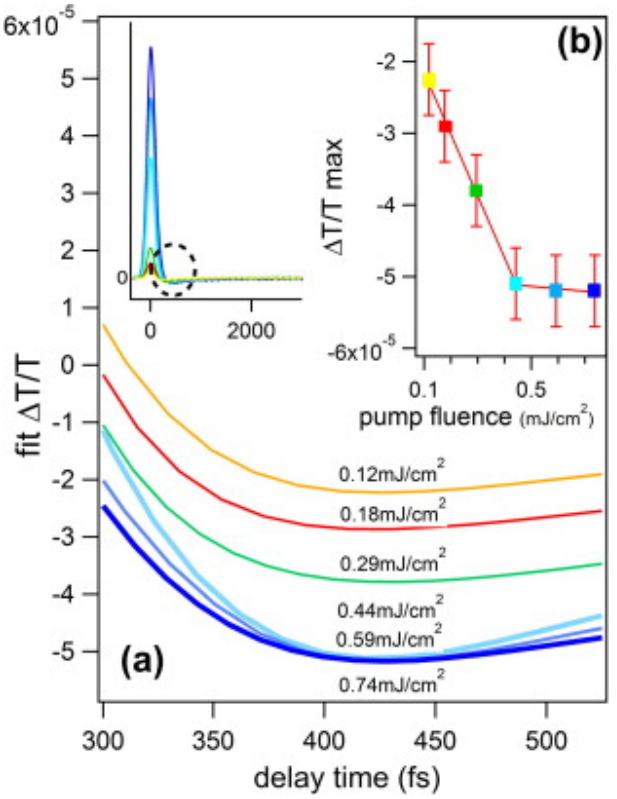

Figure 2.11: (a) Interpolated ΔT/T (inset) dependence on increasing pump fluence. The saturation effect of PA channel (second negative dynamic) is shown in (b) by plotting the maximum value of the ΔT/T relative to the PA effect versus the pump fluence.

channel quadratically increases with fluence, the resulting non-linear optical response increases much more rapidly than the linear PA of the probe. Thus, the latter saturates. PA is then quenched by rotating the probe polarization (from parallel to perpendicular) or by increasing the pump fluence. In this second case, the enhanced photo-excited charge carrier density, corresponding to an increased second order process, repopulates E_2 whose relaxation is described by the second positive dynamic (Fig.2.9c). In light of the obtained results, we emphasize that

the surprising presence of localized states in MWCNT electronic structure can be also confirmed by static photoemission and static absorption spectroscopy. The analysis of the photoemission valence band (Fig.2.12a), collected with He I radiation source (21.2 eV) clearly shows two broad features (≈1.0 eV and 3.0 eV). While the second is ascribed to the π band [39], the large feature centered at about 1.0 eV suggests the presence of occupied states under 3.0 eV. Furthermore, the absence of electronic states at the Fermi energy (inset of Fig.2.12a) indicates a semi-metallic character. This result is in agreement with transport studies, undertaken in a vacuum pumped cryostat (297 - 16 K), that show a nominal band gap of approximately 40 meV, consistent with that of other semi-metallic graphitic materials[1].

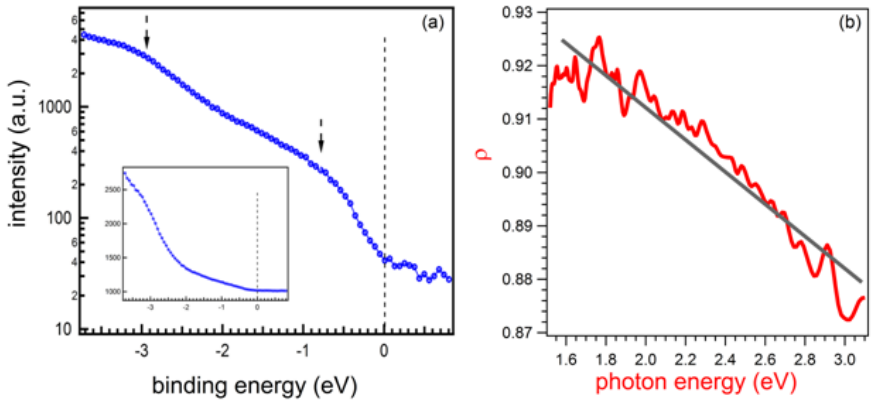

Figure 2.12: (a) UPS measurements of the valence band showing broad features at about 1.0 eV and 3 eV (log. scale). Inset: Detailed valence band , suggesting a semi-metallic character consistent with temperature dependent electron transport studies. (b) Static optical anisotropy (ρ) as a function of photon energy.

Moreover, from the optical spectra (shown in Fig.2.6), we are able to obtain

[1] Unpublished data

further insight about the presence of electronic structures in the occupied and unoccupied bands. The optical anisotropy, ρ, of the system, is defined as [53,86]:

$$\rho = \frac{\Lambda_{||} - \Lambda_{\perp}}{\Lambda_{||} + \Lambda_{\perp}} \tag{2.5}$$

where $\rho_{||}$ is the absorbance for incident beam polarization parallel and $\rho_{\perp}$ perpendicular to the MWCNT long-axis, and $I/I_0 = e^{-\Lambda}$, where $\Lambda = \Lambda_{\perp}$ or $\Lambda_{||}$, I is the intensity of the transmitted beam and I_0 is the incident intensity. As in the case of SWCNTs [86], ρ (Fig.2.12b) linearly decreases with photon energy (1.55 - 3 eV), suggesting the existence of optical transitions with a definite symmetry below 3 eV. The crucial point remains, now, to understand the origin of discrete energy levels in the electronic structure of MWCNTs. Two possible interpretations can be offered. The first is connected with the presence of amorphous carbon. sp^3 and sp^2 clusters smaller than 5 nm may very well open a gap thereby instigating the formation of originate discrete levels [87]. Indeed, the existence of electronic states associated with structural defects could represent an interesting opportunity for improving the polarization-controlled absorption in such samples. However, XPS and Raman spectroscopy (Fig. 2.4 and 2.5) seems to exclude this possibility. Moreover, there is controversy related to this interpretation. Firstly, the results reported in Fig.2.7 have been obtained at different positions on different samples grown under equivalent conditions. Furthermore, it is not clear as to how such clusters of amorphous material could give rise to electronic states with well-defined symmetry. The second interpretation is derived by considering that discrete states are present in the valence band and that the optical transitions, revealed in the transient transmittivity, involve discrete electronic states with a well-defined symmetry. In particular, it is somewhat surprising the analogy between the selection rules of the optical transitions involved in the transient response of MWCNTs and those known for the VHSs in SWCNTs. In this sense this second interpretation assumes that the electronic structure of MWCNTs is characterized, as in the case of SWCNTs, by the presence of excitonic states at the VHSs. Assuming, in fact, that the processes reported in Fig. 2.9 can be ascribed to excitonic transitions, the polarization dependence of the PA channel (Fig.2.9a and Fig.2.9b) is consistent with the selection rules that control the SWCNT optical transition. For a parallel-polarized probe, the PA corresponding to $\Delta m = 0$, where m is the quantum number identifying the VHSs sub-bands [10], is allowed. On the contrary,

when the probe is perpendicularly-polarized the PA is quenched and a second order decay process dominates (Fig.2.9c and Fig.2.9d). This alternative channel might appear similar to exciton-exciton annihilation (EEA), well studied on spatially confined systems such as nanocrystals [88] and more recently reported in SWCNTs [39, 83, 84, 89, 90]. EEA refills E_{22} and increases the transmittivity of the probe resulting in a second PB channel. The non-linear character of EEA could be compatible with the linearity of the $(\Delta T/T)^{-1}$, shown in Fig.2.8. The rate equations (3) are very similar to the rate equations model employed in literature [39, 83, 84, 90] to describe the excitonic behavior of SWCNTs in a high pump fluence regime. This SWCNT-like behavior could be also confirmed by considering the relaxation times. The first dynamic of the MWCNTs has a relaxation time (60 ± 20 fs) consistent with the E_{22}-to-E_{11} transition in SWCNTs (40 fs) [37,46]. Similarly the PA has a recovery time of the order of hundreds of femtoseconds, comparable with the E_{11}-to-E_{33} absorption channel in SWCNTs. This second interpretation, concerning the presence of excitonic states at the VHS, despite requires further confirmations, provides a more consistent depiction of the transient electronic behavior of MWCNTs. Moreover, it corroborates recent measurements reported in literature where it was shown that the VHSs play an important role in the electronic behavior of MWCNTs [20, 47, 51, 91].

2.5 Conclusions

Using high-resolution time resolved transmittivity measurements on horizontally aligned free-standing MWCNTs, we have shown that the electronic structure of these systems is different from that of HOPG. The optical response of MWCNTs is seen to be characterized by photo-bleaching and photo-absorption processes as well as second order effects. We are able to reveal these transient channels tuning the probe polarization. The obtained results suggest the existence of discrete levels with a well-defined symmetry in the electronic structure of MWCNTs. Two different interpretations have been discussed. The origin of these states appears more consistent with a SWCNT-like interpretation. It is hoped that this study will provide a deeper understanding of the so-far largely misunderstood and complex electronic structure of MWCNTs, showing, for the first time, the presence of discrete levels in these complex systems. An improved understanding of these issues, and the possibility of polarization-selective con-

trol over the optical response of MWCNTs represent important aspects in the outlook of carbon nanotube research.

Chapter 3

Transient reflectivity on vertically aligned single-wall carbon nanotubes

In this section an adapted version of the paper published in [6] is reported.

3.1 Abstract

One-color transient reflectivity measurements are carried out on two different samples of vertically aligned single-wall carbon nanotube bundles and compared with the response recently published on unaligned bundles [7]. The negative sign of the optical response for both samples indicates that the free electron character revealed on unaligned bundles is only due to the intertube interactions favored by the tube bending. Neither the presence of bundles nor the existence of structural defects in aligned bundles is able to induce a free-electron like behavior of the photoexcited carriers. This result is also confirmed by the presence of non-linear excitonic effects in the transient response of the aligned bundles.

3.2 Introduction

In these last twenty years carbon nanotubes (CNT) have played a fundamental role in the research field of nanotechnology based optoelectronics and in particular for application in solar cells and sensor devices. The outstanding and intriguing physical properties of CNT including well defined optical resonances, ultrafast non-linear response and ballistic 1D charge transport, have, in fact, stimulated both fundamental and applied research on these systems [92] and [56].

For increasing the CNT potentialities in optoelectronics, a growing effort, in these last years, has been focused in preparing single-wall CNT (SWCNT) samples with a well-defined chirality [68] and [93]. The low energy optical properties, in fact, of SWCNT are associated with the formation of electron-hole pairs described as 1D Wannier Mott excitons. The physical properties of these excitons strongly depend on the tube diameter and chirality [10] and [9].

The possibility of studying the optical response of SWCNT thin film for different architectures (unaligned, horizontally and vertically aligned tubes; isolated or bundled tubes) with a well defined electronic structure represents at the moment a challenge. Thin films of CNT, deposited, under controlled atmosphere, by using standard techniques such as chemical vapor deposition (CVD) or high pressure carbon monoxide (HiPCo), contain a broad distribution of aggregated tubes with different diameters and chiralities. The optical devices based on CNT thin film, showing the best performance, usually contain semiconducting and metallic tubes with different structures, combined with several other systems (nano-particles, molecules, metallic connector, substrate) [56] and [94]. Therefore, in order to improve the performance of the CNT based optical devices, a deeper understanding of the optical properties of thin films containing different tubes is necessary. In particular, a study of charge carriers dynamics, charge transfer and charge transport into and among the different parts of the whole system is necessary for increasing the efficiency of the carbon based devices, choosing the better configuration and the most useful components. Recently, we have shown that the architecture of CNT thin films strongly affects the charge carrier dynamics [7]. In particular, by using transient reflectivity measurements, we have demonstrated that the combination of bundling and unalignment in carbon nanotube induces strong intertube interactions favoring

the formation of short-living free charge carriers in semiconducting tubes. Some of these charge carriers decay through a charge transfer nonradiative process toward the metallic tubes within 400 fs.

Here, by using the same experimental technique, we show that the bundling alone without the unalignment as well as the presence of defects is not enough to generate this kind of free charge carriers. Performing one-color transient reflectivity measurements, in a pump probe experimental set up, on vertically aligned SWCNT, we reveal a response of the photoinduced charge carriers comparable with the exciton-like behavior observed in literature on isolated SWCNT. Photobleaching channels and non-linear effects, only measurable when the probability of creating two or more excitons per nanotube is non-negligible [89] and [83], are clearly revealed in the transient optical response.

3.3 Experimental details

Vertically aligned CNT bundles (Sample A and Sample B) were synthesized in two different laboratories. Sample A was synthesized in the Department of Engineering at the Cambridge University. The CVD process was done on sputter deposited 10 nm of Al_2O_3 on Si/SiO_2 (200 nm). Fe catalyst (1.1 nm) was thermally evaporated onto Al_2O_3. Atmospheric pressure CVD was conducted in a tube furnace at 750 ^oC in a mixture of $C_2H_2/H_2/Ar$ (30 min) after a 3 min pre-treatment in H_2/Ar. Sample B was grown in the Analytical Division of the TASC-IOM-CNR Laboratory, where the catalyst depositions and CVD processes are performed in an ultra high vacuum experimental apparatus (base pressure $< 1 \times 10^{-8}$ Pa). The CVD processes were done on thin films of 150 nm thermally grown SiO_2 support layer on polished n-type Si(100) substrates and on 10 nm thick Al_2O_3 support layers grown via magnetron sputtering on the previous film. We used Fe as catalyst, and acetylene as the precursor gas. Fe catalyst films were deposited in-situ by sublimation from heated filaments (Aldrich, 99.9% purity) at a growth rate of $\approx$ 0.6 nm/h. We operate in the following parameter window: $\approx$ 0.6-8 nm Fe film thickness, 4×10^{-6}-10^{-1} Pa C_2H_2 pressure and 580-600 ^oC growth temperature.

Both samples were characterized by micro-Raman and SEM (Scanning Electron Microscope) measurements. Micro-Raman measurements on Sample A were carried out using a Labram Dilor Raman H10 spectrometer equipped with

an Olympus microscope and with a cooled CCD camera as photodetector. The 632.8 nm light from an He-Ne laser was used as the excitation radiation. Micro-Raman measurements on Sample B were carried out using Renishaw 1000 Raman Spectrometer (Series 1000). The spectra were excited with an Ar^+ laser (514.5 nm). SEM images were acquired on both samples ex-situ, after the growth, by using a ZEISS SEM (mod. Supra 40, energy range 0.1-30 KeV).

Time-resolved reflectivity (TR) measurements have been performed with the cavity-dumped Ti:Sapphire oscillator described in chapter one , producing 120 fs, 1.55 eV light pulses. The samples have been excited with pump fluences ranging from 0.1 to 0.8 mJ/cm^2.

3.4 Results and discussion

In Fig.3.1, TR signals collected on two vertically aligned SWCNT bundles (Sample A (a), Sample B (b)) are shown together with SEM images. While the TR signal on unaligned SWCNT is positive (see ref. [7]) in agreement with the free-electron behavior of the photoinduced carriers, TR signal on aligned SWCNT is negative.

The negative signal has been interpreted as a photobleaching process [95] and [39]. When the pump photon energy is quasi-resonant with one of the optical transition between two Van Hove Singularities (VHSs), a photobleaching is usually expected in the one-color transient optical measurements. Absorption of the pump pulse excites electrons into the conduction band, creating holes in the valence band. Until these carriers relax, transient filling effects on the final states are observed. For the photobleaching effect, the transient signal is positive in trasmittivity and negative in reflectivity (such as in the absorption) [46] and [65]. The presence of the photobleaching channel in aligned SWCNT bundles suggests that the free-electron like behavior of the photoinduced carriers [7] is due to the unalignment of the bundles and not to the formation of bundles themselves.

In order to exclude that the presence of structural defects affects the charge carrier dynamics of SWCNT, in Fig. 3.1 the transient reflectivity response has been shown for two SWCNT bundles with a different content of structural defects. In Fig. 3.2 Raman spectra collected on Sample A and Sample B by using an excitation wavelength of 632.8 nm (for Sample A) and 514.5 nm

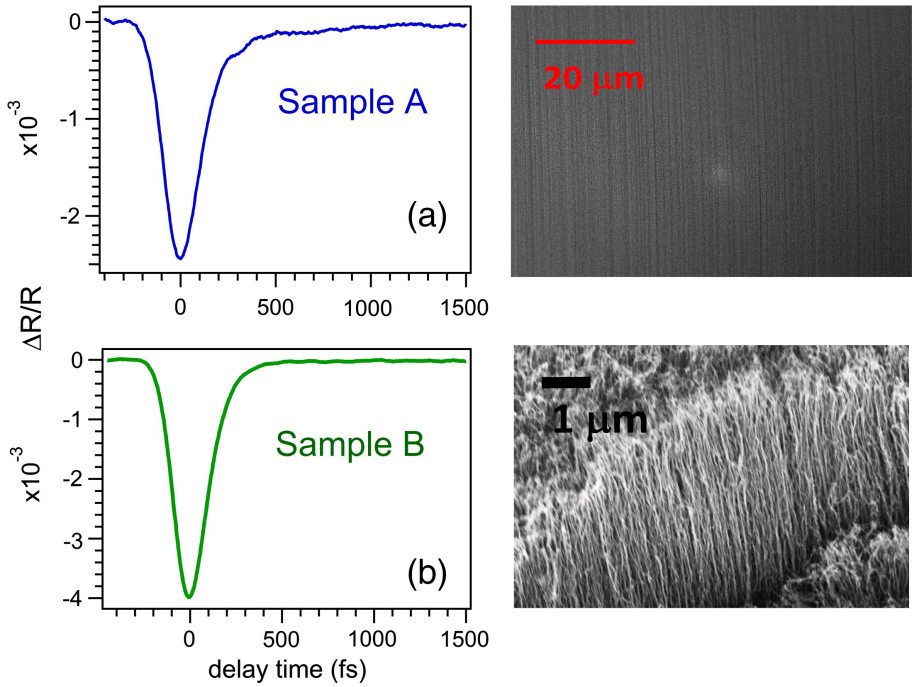

Figure 3.1: One-color (hν = 1.55 eV) transient reflectivity spectra collected on vertically aligned (Sample A (a) and Sample B (b)). The SEM images of the samples are also reported.

(for sample B) are reported. The D and the G modes are at about 1300 and 1700 cm^{-1}, the G* mode at 2600 cm^{-1} and the radial breathing modes (RBM) modes in the (150 cm^{-1}, 250 cm^{-1}) range [96]. Raman spectrum of Sample B is characterized by an intense D mode [97], because the ratio I(D)/I(G) increases with the excitation wavelength, the D mode suggests the significant presence of structural defects in this sample.

It is important to underline that in Sample B the large presence of defects is in anyway compatible with a predominant content of sp^2 hybridization of C atoms in the nanotube walls. The energy position of the G mode (about 1590 cm^{-1}) and the ratio I(D)/I(G) = 0.9, in agreement with the graph taken from ref. [63] and [98], argue that nanotubes are mainly composed of sp^2-hybridized

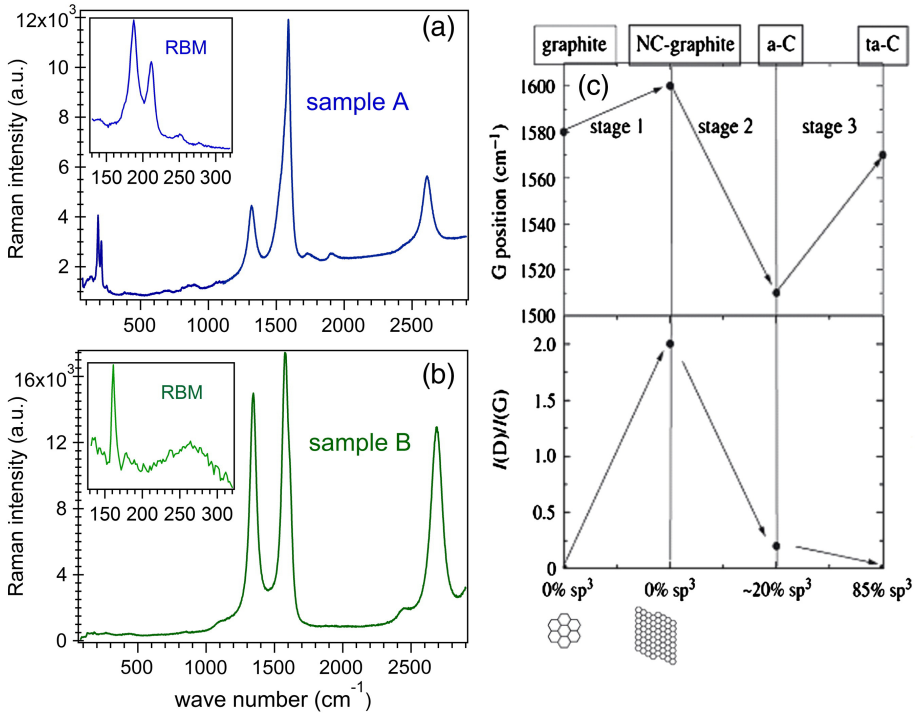

Figure 3.2: Raman spectra collected on Sample A (a) and Sample B (b) by using a laser wavelength of 632.8 nm and 514.5 nm, respectively. The intensity of the D mode in the Sample B suggests a significant presence of structural defects in this sample. (c) Graph adapted from ref. [63] to estimate the content of sp^2, sp^3 hybridization in Sample A and B.

C atoms even if the significant presence of defects clearly indicates that the wall is composed of clusters and not of homogeneous graphene sheet.

From the analysis of the RBM mode, it is possible to estimate the average diameter of the carbon nanotubes and then by using the Kataura scheme [99] to evaluate the energy positions of the VHSs in both samples. In Sample B the RBM are principally located around 160 cm^{-1} (sharp structure) and 270 cm^{-1} (broad structure) corresponding to a diameter ranging from 0.9 nm to 1.55 nm. In the Kataura scheme [99] these diameters indicate that the second VHS (E_{22})

is located at about 1.15 eV and 1.7 eV, respectively. On the contrary, in Sample A, the RBM are located around 185 cm^{-1} and 215 cm^{-1} corresponding to a diameter of 1.4 nm and 1.2 nm. From the Kataura plot, the second VHS results at about 1.2 eV - 1.45 eV. For both samples, the pump photon energy (1.5 eV) is able to populate the second VHS giving rise to a photobleaching channel in the transient reflectivity (Fig.3.1).

However, by interpolating the transient response, a difference in the reflectivity of the two aligned bundles appears. While Sample A is well fitted by two exponential decays, Sample B is interpolated only by one exponential curve (Fig.3.3a and b).

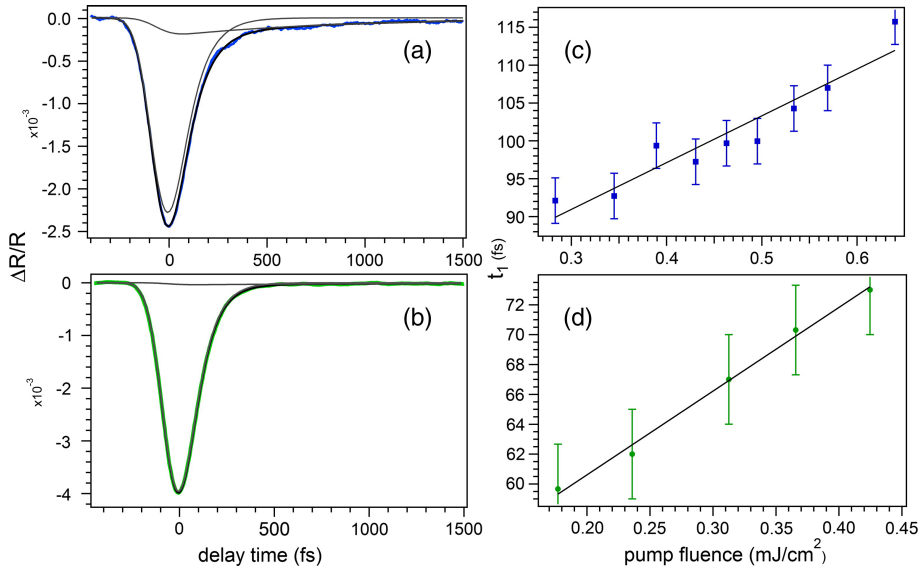

Figure 3.3: (a, b) Transient reflectivity signal collected on Sample A and B. The data result well fitted by two and one exponential decay for Sample A and B, respectively. (c,d) Decay time of the first dynamics versus the pump fluence for Sample A and Sample B.

In both samples, the resulting decay time of the first dynamics (90 ± 10 fs for Sample A (Fig.3.3c) and 65 ± 15 fs for Sample B (Fig.3.3d)) is compatible with the relaxation time from the second excitonic level E_{22} to the first one

E_{11} [100], [37] and [46]. The linear trend of the first decay time against the pump fluence (Fig. 3.3c, d) leads to exclude radiative processes [101]. Concerning the second dynamics (with a relaxation time of about 1 ps) of Sample A transient signal, it is usually ascribed in SWCNT to non-linear excitonic effects [89].

A picture of the dynamics in this case is reported in Fig. 3.4a. Excitons are promoted by the pump from the ground state GS to E_{22} (second VHS) state, inducing the first photobleaching. The excitons created in E_{22} state relax very fast (in few tens of fs) to the E_{11} state (first VHS). Due to the high pump fluence (10^{14} - 10^{15} photons/cm^2) and the long E_{11} decay time (few picoseconds [93]), excitons annihilate and repopulate E_{22}. This process, known as exciton-exciton annihilation (EEA), increases the transmittivity of the probe resulting in a second photobleaching channel.

Due to the dipole selection rules, the optical transition from the ground state to E_{22} state is likely when the pump polarization is parallel to the carbon tube [93]. In our experimental condition, the pump polarization is perpendicular to the tube. However, because of in Sample A the pump photon energy (1.5 eV) is resonant with the GS-E_{22} transition (1.3 ± 0.2 eV), a dense population is in anyway photoinduced in the E_{22} state allowing the EEA process. In Sample B, the energy of the GS-E_{22} transition is less resonant with the pump photon energy, thereby reducing the excited carrier density and preventing the EEA.

In order to verify that the positive second dynamics in Sample A is the result of an EEA process, in Fig.3.4b the inverse of the transient reflectivity, $(\Delta R/R)^{-1}$, is plotted as a function of the delay time. The quadratic dependence of the temporal evolution of the exciton population on the population itself implies that [83], [90] and [39]:

$$\left(\frac{\Delta R}{R}\right)^{-1} \propto \Delta t \tag{3.1}$$

here Δt is the delay time between pump pulse and probe pulses. The linear behavior shown in Fig.3.4b confirms the non-linear character of the second dynamics in Sample A transient signal. To rationalize our findings, a rate equation model [39] and [90] is here proposed to interpret the physical processes drawn in Fig. 3.4a. The temporal evolution of the excitons on the E_{22} state (N_2) and on the E_{11} (N_1) is then determined by:

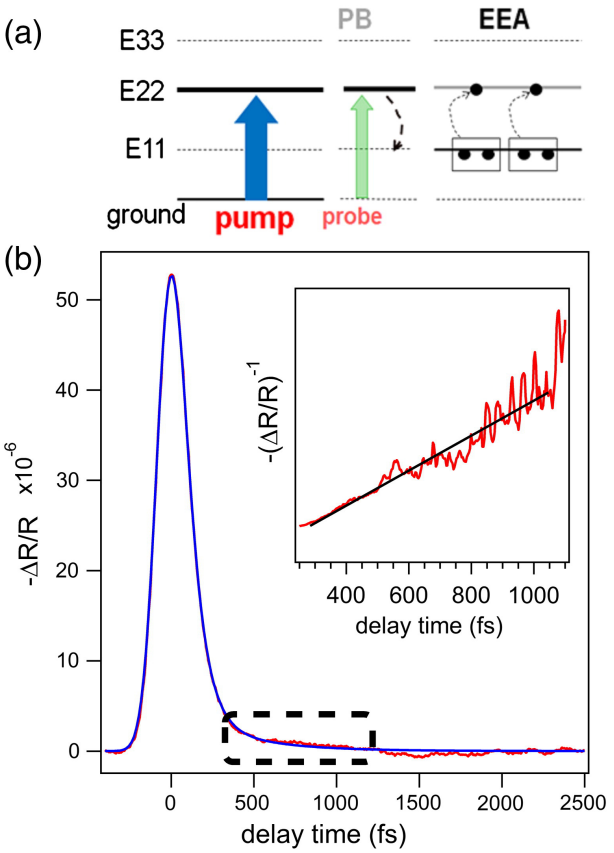

Figure 3.4: (a) Sketch of the relaxation processes of the carriers excited in Sample A. (b) Fitting of the transient signal collected on Sample A by using the rate equation model. The linear behavior of the inverse of the transient reflectivity versus the delay time confirms that the second dynamics is ascribed to the exciton-exciton annihilation process.

$$\begin{cases} \frac{dN_2}{dt} = A \cdot G(t) - B \cdot N_2 + \frac{C}{2} \cdot N_1^2 \\ \frac{dN_1}{dt} = B \cdot N_2 - D \cdot N_1 - C \cdot N_1^2 \end{cases} \tag{3.2}$$

where the Gaussian laser pump $G(t) = (\sigma 2\pi)^{-1} e^{-t^2/2\sigma^2}$ source populates

the E_{22} state that becomes depopulated by the $-BN_2$ term where B^{-1} corresponds to the N_2 decay time ($E_{22} \rightarrow E_{11}$). The $CN_{12}/2$ term represents the population of the E_{22} state due to the annihilation of the excitons on the E_{11} state. As a consequence the E_{11} state is populated by the relaxation of the excitons from the E_{22} state (BN_2) and depopulated by the relaxation into the ground state ($-DN_1$) and by the annihilation process ($-CN_{12}$). In the approximation that the static reflectivity is mainly dominated by the complex part of the dielectric function, as found for HOPG graphite [102], the $\Delta R/R$ signal is proportional to the N_2 population, the probe photon energy being resonant with the E_{22} state. As shown in Fig.3.4b, the transient response is well approximated by the proposed model. The mean fitted B^{-1} value, for the low fluence spectra, is 65 $\pm$ 15 fs. This value is consistent with the value (40 fs) reported for the $E_{22} \rightarrow E_{11}$ decay in SWCNT and with the result previously obtained by interpolating the data with two exponential curves. The fitted D^{-1} value is consistent with the relaxation time of the E_{11} state.

3.5 Conclusions

In conclusion, by performing transient reflectivity measurements on SWCNT bundles we have shown that the free-electron behavior already observed in unaligned bundles is mainly due to the unalignment. The presence of bundles and a different content of structural defects in the vertically aligned SWCNT reveal an excitonic behavior comparable with that observed in literature on isolated tubes. In order to address the second dynamic revealed in the transient response, a rate equation model involving the exciton-exciton annihilation process has been proposed.

Chapter 4

Charge carriers dynamics in ultra-pure single walled carbon nanotubes free-standing thin films

The charge carriers dynamics in an ultrapure metallic enriched single wall carbon nanotube film is investigated thought transient optical absorption spectroscopy. By a comparison of the transient transmission signals collected with an excitation photon energy in or out of resonance from the main exciton absorption peak we single out a long lived photoabsorption dynamics not ascribable to the exciton excited-state absorption. This long lived signal is not present in semiconducting enriched ultrapure films, prepared from the same parent SWCNT mixture, and thus is ascribed to be originated from the metallic SWCNT species. By estimating the equilibrium temperature of the photoexcited carriers in the metallic tubes upon laser excitation we are able to exclude a pure thermal effect as the origin of the observed photoabsorption signal. We suggest that the origin of the PA transient as to be found in optical transitions involving an hot Dirac fermion population excited in the vicinity of the Fermi level which can be promoted in higher lying electronic states upon absorption of probe photons.

Starting from this assignation and considering the pump energy and fluence dependence of the signal amplitude we found evidence of a possible carrier multiplication process taking place in the metallic carbon nanotubes.

4.1 introduction

Thin film of metallic or doped semiconducting SWCNT are good candidates to replace the conducting transparent metallic oxides in both organic or inorganic solar cells due to their superior conductivity. In particular metallic carbon nanotubes show the capability to withstand large current densities due to their low electron-phonon coupling [26] and to have large carriers mobility [27]. On the other hand semiconducting carbon nanotubes can be turned metallic via molecular charge transfer dopants where the chemically induced state filling effect is also responsible for a dramatic change of the their optical absorption spectra. Both an increased conductivity and an increased transparency in the visible or in the infrared part of the spectrum can be simultaneously archived [28], making doped SWCNT layers an ideal candidate for transparent electrodes fabrication. As we have already pointed out much of the ongoing experimental and theoretical efforts focus on the transient optical properties, and therefore on the carrier relaxation dynamics, of isolated semiconducting carbon nanotubes [3]. In particular the transient optical properties of metallic carbon nanotubes are not commonly investigated and their carrier relaxation dynamics is usually inferred from experiments performed on mixed metallic and semiconducting SWCNT samples [43, 103]. In these chapter we investigate the carriers relaxation process, within a few picoseconds time scale, in metallic enriched and semiconducting enriched ultrapure single-wall carbon nanotubes free standing films, using two-color time-resolved optical transmittivity measurements. The high level of purity of our samples allows us to disentangle the contribution of metallic and semiconducting tubes in the optical transients highlighting the different dynamical behavior of the two SWCNT species.

4.2 Ultrapure free-standing SWCNT

The samples consists in two free standing ultrapure carbon nanotubes thin films provided by the group leaded by prof. K. Kamáras from the Wigner research center for physics. Each sample is prepared starting from laser-ablated SWCNTs of 1.34 nm mean diameter using the purification procedure described in [28]. The first sample is a metallic enriched carbon nanotubes (M-SWCNT) film whilst the second one is a semiconducting enriched carbon nanotubes (S-SWCNT) film. Both samples are characterized via optical transmission experiments in a wide wavelength range, from the far infrared (0.004 eV) to the UV (6.5 eV) [104]. The static transmission spectra of the M-SWCNT enriched film is reported in fig.4.1

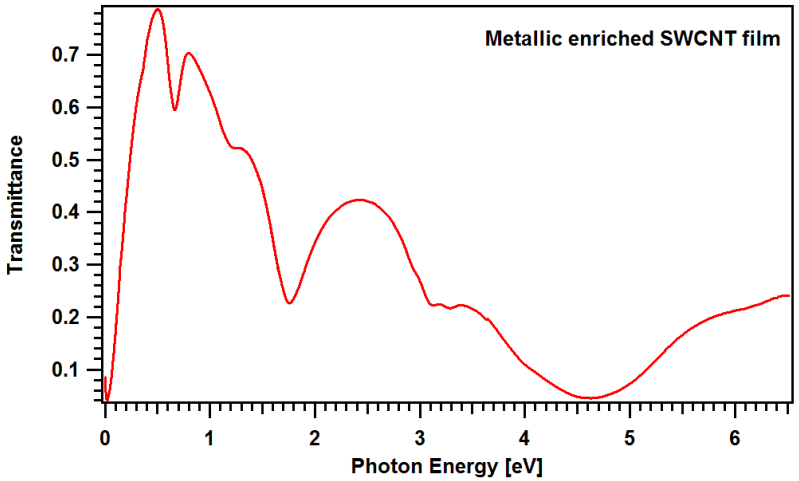

Figure 4.1: Static optical transmittance spectra for the metallic enriched SWCNT free standing film.

The characteristic peaks due to the exciton transitions can be clearly resolved. The main transition peaks are localized around 1.75 eV and between 3.11-3.28 eV. These are identified as the M11 and M33 exciton transitions arising from the metallic tubes. Residual semiconducting SWCNT are responsible for the absorption peaks localized at 0.66 eV and 1.19 eV. The high absorbance

shoulder localized at low energies is due to a combination of the SWCNT Drude conductivity and to the transitions across the curvature-induced band-gap [104]. The high purity degree of the SWCNT films is confirmed by the lack of strong background absorption in the near infrared [8, 105] and by the presence of strong exciton resonances, whilst the multiple SWCNT chiralities and solid state effects, such as intertube interactions, are responsible for the inhomogeneous broadening of the exciton transitions as well as the lineshapes structure of the absorption peaks.

The static transmittance spectra of the S-SWCNT film is reported in fig.4.2. As for the metallic tube sample a set of transitions can be clearly resolved. E11 and E22 exciton transitions are found around 0.66 and 1.19 eV. Another group of transitions is detected between 2.21 and 2.7 eV. These set of absorption lines are ascribed to the E33 exciton transitions due to the various SWCNT chiralities present in the sample.

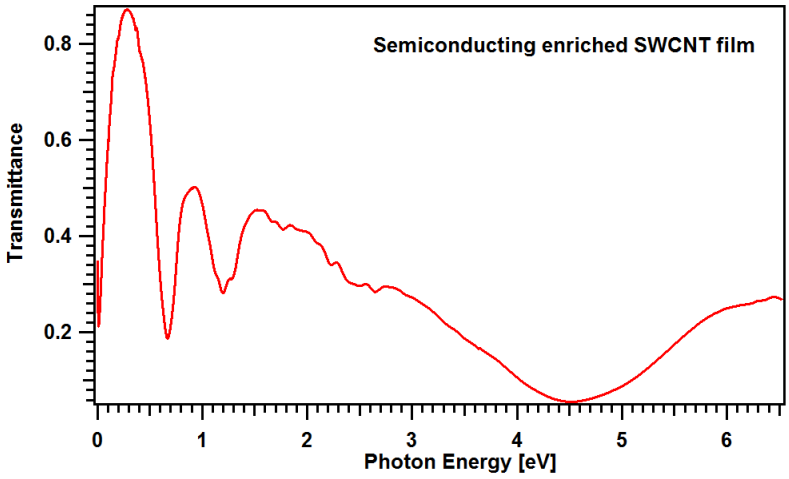

Figure 4.2: Static optical transmittance spectra for the semiconducting enriched SWCNT free standing film.

The high ratio between the semiconducting and the metallic tubes content in the semiconducting enriched film, as well as its low value for the metallic enriched one, is testified by the optical absorption measurements. From a simple

comparison among the absorption spectra (fig.4.2, Fig.4.1) the quenching of the exciton transitions due to the metallic or, conversely, to the semiconducting tubes is evident. The broad absorption feature centered at 4.6 eV, which is present in both samples, can be ascribed to the π plasmon resonance. The film thickness is 92±2 nm for the semiconducting enriched sample whilst the for metallic enriched one it is estimated in about 130 nm. For both samples we assume a density of 0.4 gr/cm^3 as measured in [104] for similar samples prepared with the same ultrapurification technique and parent nanotube mixture.

4.3 Experimental setup and laser system

Time resolved optical measurements have been performed only with the high fluence setup systems described in chapter one in a two-color transient transmittivity (TT) scheme. The most of the TT experiments are performed in a two-color variable-pump and fixed-probe configuration by using a 1 KHz amplified Ti:Sapphire laser system capable to deliver 0.5 mJ, 150 fs, 1.55 eV light pulses, together with a travelling wave optical parametric amplifier (TOPAS). The probe energy is kept fixed at 1.55 eV whilst the pump energy is tuned in the 0.75 - 1.0 eV and 1.55 - 2.05 eV energy ranges. For the latter range the TOPAS output is doubled via a BBO nonlinear optical crystal. The pump beam is focalized at the sample plane in a 100 μm spot diameter, corresponding to a 2.3 - 10 mJ/cm^2 fluence range. Cross-polarized pump and probe beam in a near normal incidence configuration are used. In order to directly access the relaxation dynamics of the first exciton state in the semiconducting carbon nanotubes a TT measurement using the TOPAS output as a probe is performed. In this inverted configuration the pump photon energy is kept fixed at 1.55 eV, the pump FWHM spot size is 200 μm and the probe spot size is increased at 100 μm. A schematic illustration of the experimental line in this alternative configuration is reported in fig.4.3.

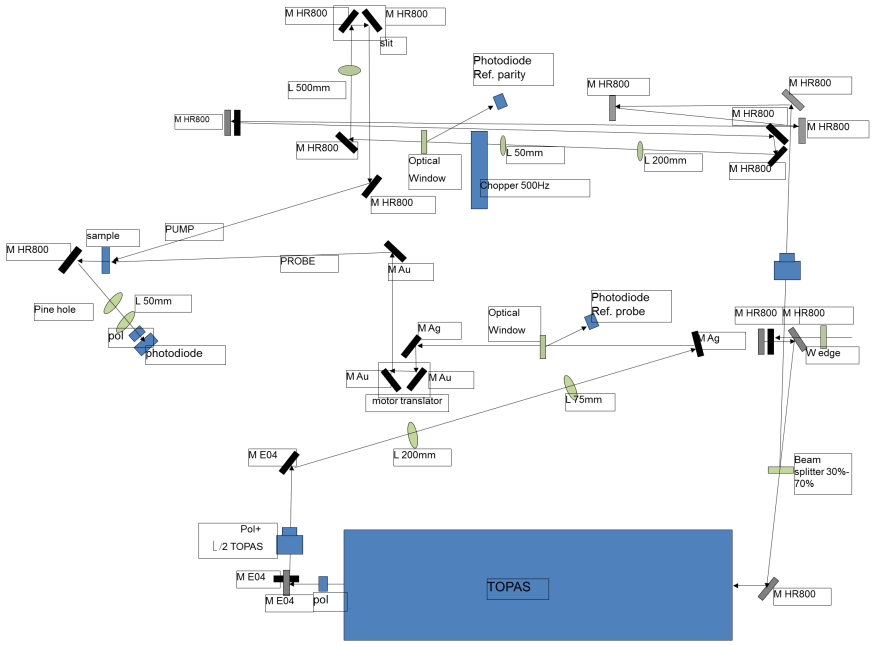

Figure 4.3: Experimental line schematic for the fixed pump - tunable probe configuration.

4.4 Metallic enriched SWCNT: results and discussion

In Fig.4.4 the transient transmittivity signals collected varying the pump photon energies in an IR interval between 0.75 eV and 1 eV are reported. The pump fluence is 22.9±0.25 mJ/cm^2 for all the measurements, whilst the probe energy is fixed at 1.55 eV. In this range the TT signal is characterized by a strong photobleaching signal near zero-delay which rapidly relax within 500 fs. For delay times longer than 500 fs a photoabsorption feature develops and slowly relax toward the equilibrium condition on a multi-picosecond time scale.

Metallic carbon nanotubes are characterized by the presence of bands with linear dispersion which directly descend from the Graphene band structure

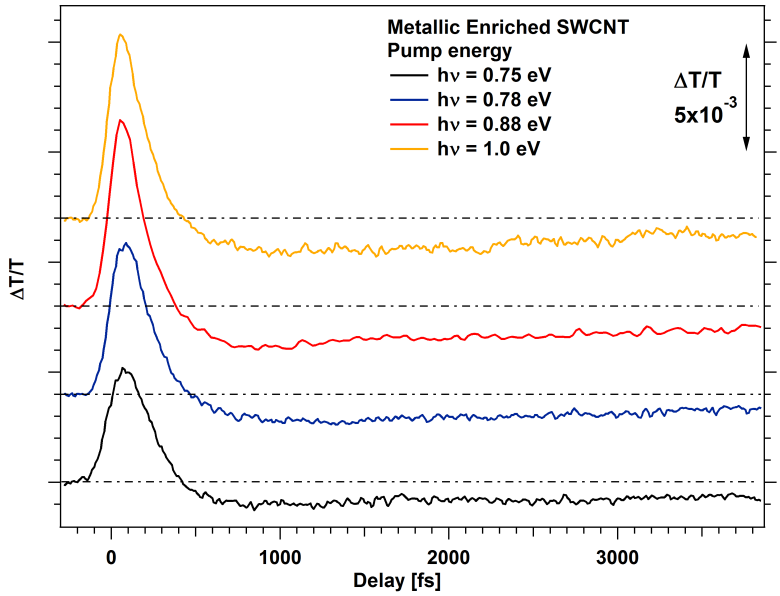

Figure 4.4: Transient transmittivity signal from the metallic enriched SWCNT film. F=22.9±0.25 mJ/cm^2. Excitation photon energies are between 0.75 and 1.0 eV. Traks are shifted for clarity.

around the K point. Direct interband transitions between states in these bands are generally allowed and give rise to an absorption continuum around the exciton absorption peak that , in our sample, is centered at 1.75 eV (Fig.4.1). The pump photon energies used in the IR range, being at most 1 eV, are well out of resonance with the main exciton transition, we thus expect to excite electron-hole pairs within the $\pi - \pi^*$ states in the absorption continuum. Relying on this consideration we ascribe the photobleaching signal near zero-delay times to a fast electron-electron scattering process which quickly broadens the photoexcited electron distribution up to the probe energy. The observed signal is due to a final state filling effect caused by this highly out of equilibrium electron distribution. Similar effects are commonly observed in HOPG and Graphene transient optical measurements. Moreover the electron-electron scattering time in HOPG is estimated to be in the order of 10 fs [106], well below the FWHM

cross-correlation time of our laser system (≈ 180 fs). The increasing amplitude of the photobleaching feature with increasing pump photon energy also support this assignment. On the contrary the long-lived photoabsorption signal which develops for longer delay times has no trivial similarities with the graphene or HOPG case. Moreover, as will be further discussed in the next paragraph, is not observed in the semiconducting enriched SWCNT sample (Fig.4.5).

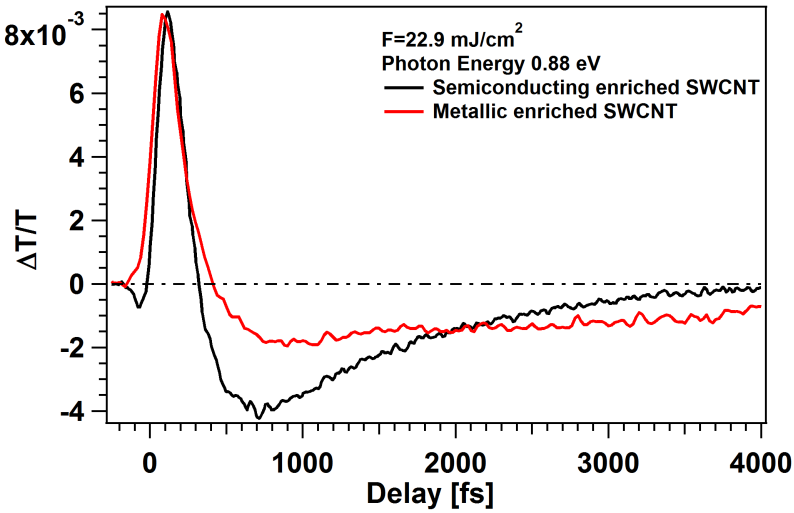

Figure 4.5: Comparison between the transient transmittivity signal from metallic enriched SWCNT (red line) and semiconducting enriched SWCNT films (black line). F=22.9±0.25 mJ/cm^2 with a 0.88 eV excitation energy.

In fig. 4.6 the TT signals collected with pump photon energies in a visible range, between 1.56 and 2.03 eV are reported.

In this case the pump fluence is 7.6±0.25 mJ/cm^2 whilst the probe photon energy is 1.55 eV. As for the previous case (4.4) the TT signal shows a fast photobleaching feature near zero-delay times followed by a long photoabsorption dynamics. For pump photon energies between 1.76 and 2.03 eV an additional intermediate relaxation in the photoabsorption signal becomes evident, together with an abrupt reduction of the photobleaching peak value. These excitation energies are resonant, or sightly above, with the M11 exciton transitions there-

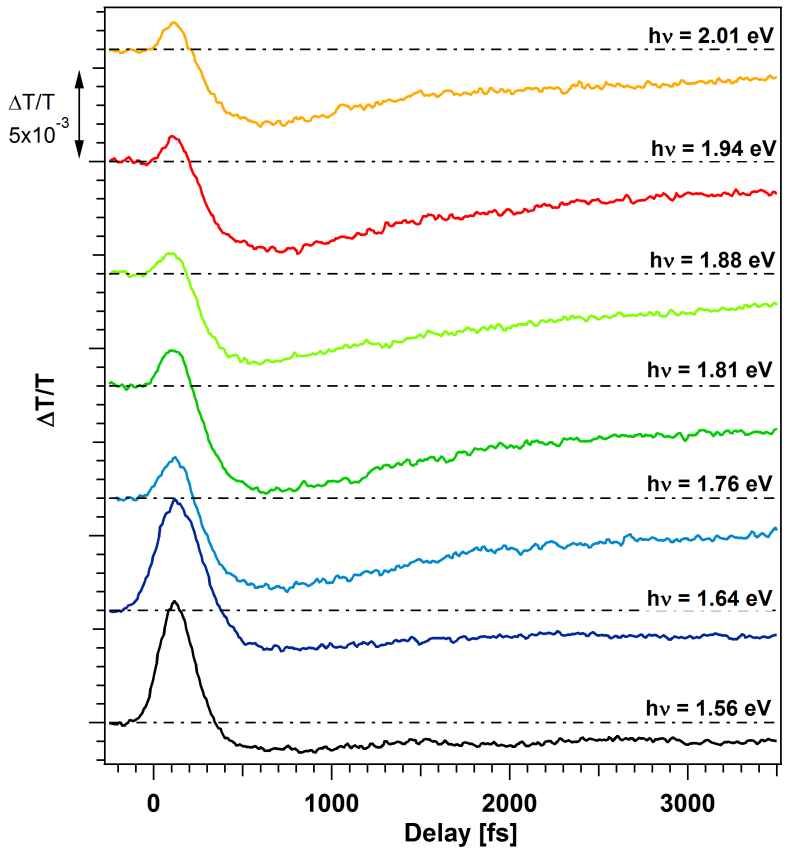

Figure 4.6: Transient transmittivity signal from the metallic enriched SWCNT film. F=7.6±0.25 mJ/cm^2. Excitation photon energies are between 1.56 and 2.03 eV. Each signal is labeled with its pump photon energy. Tracks are shifted for clarity.

fore the additional feature of the photoabsorption signal can be due to the direct exciton population. It is worth to note that the energy difference between the M11 and the M22 exciton states is of about 1.5 eV thus an additional photoabsorption channel opens up at our probe photon energy when a significant exciton population is generated by the pump pulse. In this case the reduced

photobleaching peak intensity can be due to the lower spectral weight of the interband transition near the exciton absorption peak or simply to the overlap with an increased photoabsorption signal, being the two processes independent. For long delay times only the slowest component of the photoabsorption signal is still present. Due to the high fluence used in our experiments and to the high optical density of our sample (Fig.4.1) a significative amount of energy is deposited in the pumped volume by each pump pulse so thermal effects could be at the origin of the long lived photoabsorption signal. It has been found, using resonant Raman spectroscopy, that lattice heating in semiconducting carbon nanotubes can lead to either blue-shift or red-shift of the E22 exciton absorption line, depending on the tube chirality [107]. A red-shift of the optical absorption spectra could indeed justify to the observed photoabsorption signal at long delay times. Moreover, at first glance, a multi-picosecond relaxation dynamic can be consistent with the slow heat diffusion outside the excited volume due to the electronic thermal conductivity of the SWCNT. In order to investigate this possibility we estimate the carrier equilibrium temperature using a two-temperature model [42] and analyze the dependence of the phoabsorption signal intensity (at long delay times) on the equilibrium temperature variations. Since our measurements do not allow to directly access the carrier temperature our model is based on the results reported by Hertel and Moos in [43]. In [43] the evolution of a photoexcited carrier distribution in the proximity of the Fermi level was investigated using time resolve photoemission measurements performed on a mixed metallic and semiconducting SWCNT film. From the photoemission spectra the electron temperature of the thermalized electrons was directly measured interpolating the photoemission spectra with a Fermi-Dirac function. Moreover the electronic temperature variation, due to energy transfer toward the phonon system, takes place on a picosecond time scale. From these measurements an estimation of the electron-phonon coupling term in metallic SWCNT was obtained. (See chapter one) Following [43] we estimate the carrier temperature using equation (4.1)

$$\begin{aligned} C_e \frac{dT_e}{dt} &= -H\left(T_e, T_l\right) + S\left(t\right) \\ C_l \frac{dT_l}{dt} &= H\left(T_e, T_l\right) \end{aligned} \quad . \tag{4.1}$$

where $S\left(t\right)$ is the laser pulse power, T_e and T_l are the electron and the lattice

temperature, C_e and C_l are the electronic and lattice heat capacities. The coupling term $H(T_e, T_l)$ describes the interaction between the electronic and the phononic degrees of freedom that, for electronic and phononic temepeature similar or smaller than the Debye temperature Θ_d, reads [44]

$$H(T_e, T_l) = \frac{144\zeta(5) k_b \gamma}{h} \frac{\lambda}{\Theta_d^2} \left(T_e^5 - T_l^5\right) \tag{4.2}$$

In eq.(4.2) ζ is the Riemann zeta function, k_b the Boltzmann constant, γ the electronic heat capacity coefficient, h the Planck constant and λ the electron-phonon mass enhancement factor. Dispite the large excitation anisotropy along the pump light path across the SWCNT film, caused by the high optical density of the film, for simplicity we neglect heat diffusion terms in our simulations. As source term ($S(t)$ in eq.(4.1)) we use a Gaussian function representing the laser pulse total power. Its FWHM duration is extracted from cross-correlation measurements whilst its peak intensity is calculated by multiplying the pump fluence with the sample absorption value at the pump center energy. The values of λ/θ_d^2 is taken as 4×10^{-10} $1/K^2$ [43] whilst for the electronic heat capacity a value of γ =0.035 mJ/gK is assumed. In [43] the lattice temperature variation was neglected and thus the lattice is considered as a heat bath with infinite heat capacity. Due to the high pump fluences used in our experiment we relax this approximation, keeping trak of the lattice temperature evolution as well. At 300 K the lattice heat capacity of carbon nanotubes is similar to the graphite one [108] we thus use the C_l values reported in [109] which are valid for graphite in a temperature range between 300 K and 1700 K. Since this approximation does not take into account the different SWCNT and Graphite Debye temperatures, nor the possibility of nonequilibrium optical phonons emission in the first instants after the excitation, our results should be considered only as an estimation of the carrier temperature evolution. In fig.4.7 an exemplificative simulation for a pump fluence of 7.6±0.25 mJ/cm^2 at 1.65 eV is reported.

The red line is the temperature evolution for the electron distribution whilst the blue one is the temperature evolution of the lattice. For comparison the temperature of the electrons considering $C_l = \infty$ is also reported (green line). In our fluences and photon energy ranges the maximum electron temperature is about 2100 K . Obviously this model assumes a complete electron thermalization within the pump pulse duration and cannot be used to account the effects due to

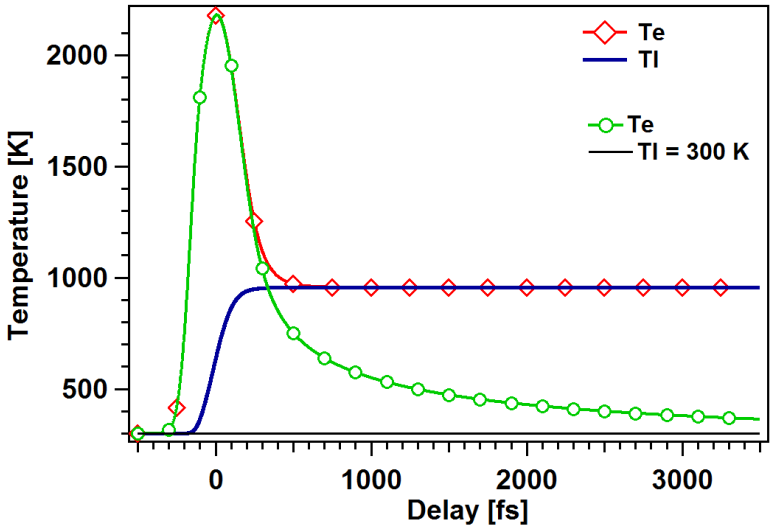

Figure 4.7: Simulation of the electronic (red line and markers) and lattice (blue line) temperature evolution using eq.(4.1). The pump fluence is 7.6±0.25 mJ/cm^2 and the excitation photon energy is 1.65 eV. The green line is the electronic temperature if an infinite lattice heat capacity is used.

the out of equilibrium electron population such as the the photobleaching signal observed near zero delay times in our TT signals (Fig.4.4 and 4.6). It is worth to note that in our simulations a complete thermalization between the electronic and the lattice degrees of freedom takes place within one picosecond. Moreover a significant lattice heating is found, being the equilibrium temperatures in the order of 1000 K. In fig.4.8 the absolute value of the photoabsorption signal amplitude versus the estimated equilibrium temperature is displayed. The reported signal amplitude is measured 3.8 ps after the excitation for all the TT signal collected in the 0.75-1.0 eV and in the 1.56-1.65 eV energy intervals, where a significant contribution from the intermediate photoabsorption dynamics (Fig. 4.6) is not present. The different equilibrium temperatures depend both on the laser pump fluence, which is 7.6±0.25 mJ/cm^2 for the 1.56-1.65 eV measurements (red triangles) and 22.9±0.25 mJ/cm^2 for the 0.75-1.0 eV measurements

(black squares), and on the sample absorption coefficient at the pump photon energy.

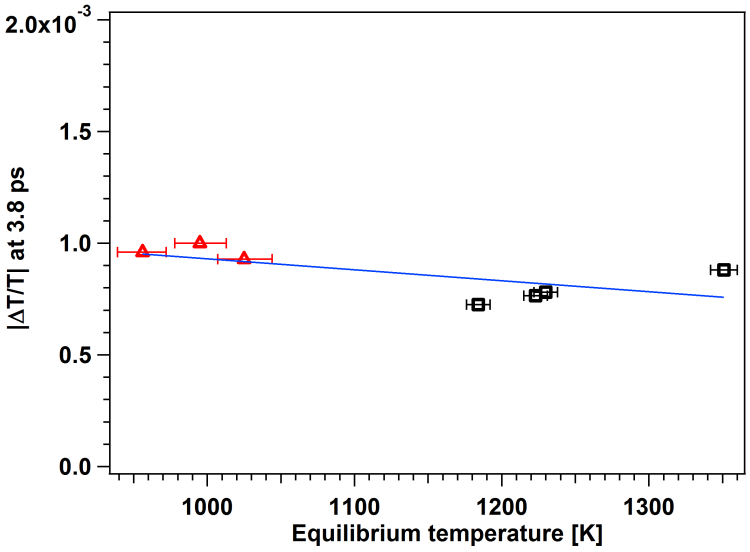

Figure 4.8: Amplitude of the PA signal 3.8 ps after the pump excitation. The black squares are relative to measurements performed in the 0.75-1.0 eV energy range and with a laser pump fluence of 22.9±0.25 mJ/cm^2. The red triangles are relative to measurements performed in the 1.56-1.64 energy range and with a laser pump fluence of 7.6±0.25 mJ/cm^2. The blue line is a linear interpolation of both dataset. The equilibrium temperature variation are due to the combined effects of fluence and sample absorption variations. The error bars on the equilibrium temperature are calculated using the fluence absolute error values.

Taking into account the results of our simulations we expect that 3.8 ps after the pump excitation the electron-lattice thermal equilibrium is well established, therefore only the eventual dependence of the slow photoabsorption amplitude on the equilibrium temperature is highlighted. From a simple inspection of graph 4.8 it is evident that the photoabsorption signal amplitude is almost constant in the whole equilibrium temperature interval ($\approx$ 950 - 1350 K). If the physical mechanism at the base of the slow photoabsorption signal had a pure

thermal origin its temperature dependence obtained by keeping a constant laser pump fluence and scanning the excitation energies or by keeping a fixed photon energy and scanning the laser fluences should be the same. In fig.4.9a the TT signals collected at 1.65 eV with three different laser fluences are reported together with the slow photoabsorption signal magnitude versus the corresponding equilibrium temperature. (fig.4.9 b). In this case the signal magnitude shows a clear linear dependence on the estimated equilibrium temperature with a slope of 2.2×10^{-7} 1/K.

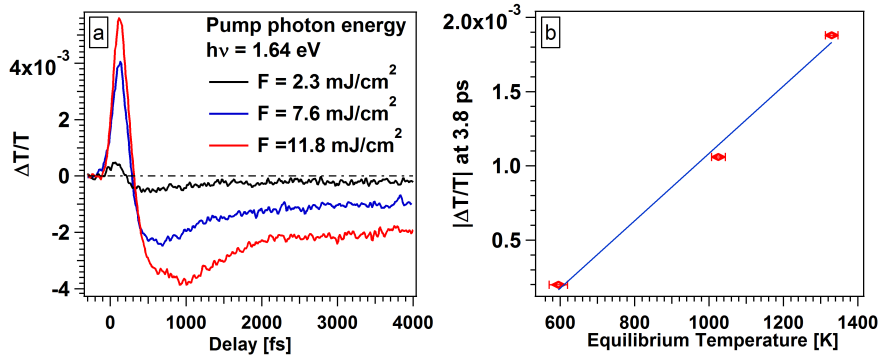

Figure 4.9: a) TT signal at 1.65 eV for 3 different pump fluences. b) PA signal amplitude at 3.8 ps after the photoexcitation versus the estimated equilibrium temperature. the blue line is a linear fit interpolation with slope of 2.2×10^{-7} 1/K

Comparing fig4.8 and fig4.9 the different photoabsorption amplitude dependence on the equilibrium temperatures is evident. This rules out a pure sample heating effect as the main source of the long photoabsorption.

Photoabsorption signals, originating from metallic carbon nanotubes, has been previously observed by Luer et al. [103] In [103], using time and energy resolved TT measurements, a photoabsorption signal band is detected and assigned to optical transitions involving hot Dirac fermions. Hot electrons in the proximity of the Fermi energy can be promoted to higher lying states upon absorption of probe photons if their polarization is perpendicular to the tube axis [110], giving rise to a PA signal. Similarly we ascribe the long photoabsorption channel to optical transitions that excite the long lived Dirac Fermions

from the bottom of the π^* band to a higher energy level. Due to our fixed probe photon energy we cannot directly determine the PA band center energy, however using the alternative setup configuration described in the laser system section, we performed an experiment with an excitation energy of 1.55 eV and a probe energy of 0.76 eV. In these conditions only a photobleaching signal is detected. (Fig. 4.10)

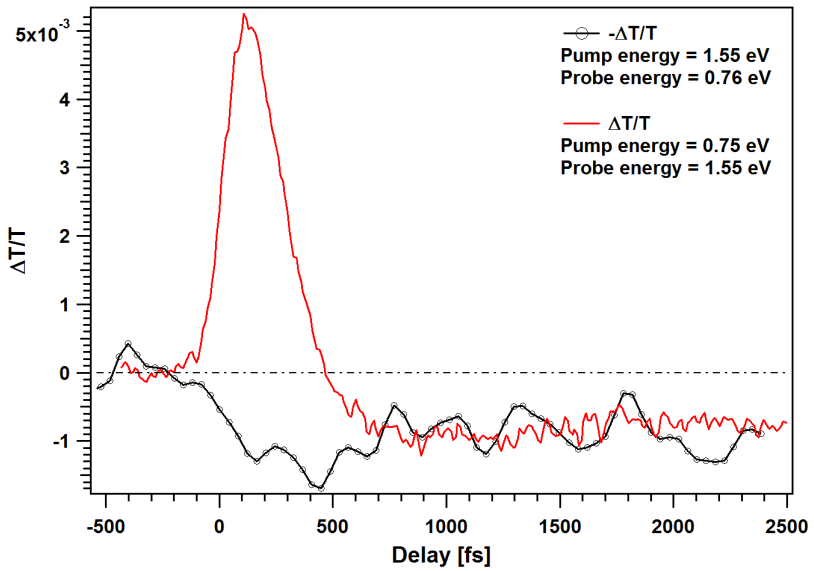

Figure 4.10: Comparison between the TT signal collected with an excitation energy of 0.75 eV and a probe energy of 1.55 eV (red line) and the TT signal collected at an excitation energy of 1.55 eV with a probe energy of 0.76 eV. (black line and markers). The latter signal is inverted in sign and rescaled in order to highlight the similar dynamics.

This result assigns a lower limit on the energy of the photoabsorption band edge indicating that the optical transitions responsible for the PA signal take place from Dirac fermions states toward band states localized at more than 0.76 eV from the Fermi energy. The PB singnal is consistent with a final state filling effect of the optical transitions between the linear bands around the Fermi edge. Despite the short delay time window used for the measurement the PB

signal shows a slow relaxation dynamics comparable to the PA signal one further supporting the idea that Dirac fermions are involved in both processes. The absence photoabsorption signal at 0.76 eV also rules out a possible Drude contribution to the PA signal detected at 1.5 eV since, in this case, a characteristic increase of the PA signal magnitude for decreasing probe energies should be observed. In order to get further insight on the process we fit our dataset with three exponential decay functions convolved with a Gaussian.

$$\frac{\Delta T}{T} = G(t) * \left(A_1 e^{-\frac{t}{\tau_1}} + A_2 e^{-\frac{t}{\tau_1}} + A_3 e^{-\frac{t}{\tau_3}} \right) \tag{4.3}$$

From now on we will refer to A_1 and τ_1 as the first photobleaching signal amplitude and decay time, to A_2 and τ_2 as the ones for the intermediate fast component, to A_3 and τ_3 as the amplitude and the decay time of the slow PA signal component.

In fig. 4.11 the TT signal collected at F=7.6±0.25 mJ/cm^2 with an excitation energy of 0.88 eV together with its best fit is reported. As can be seen the TT signal is quite well interpolated by this empirical function giving a χ^2 value of 1.7×10^{-5}.

The long delay time window (Fig.4.11) allows to determine the decay time constant of the slow PA signal component τ_3=6800±240 fs. Due to the shorter delay times windows of the other measurements we impose this τ_3 value in all the other TT signal fittings. For the measurements performed in the 0.75-1.0 eV energy range the fast photobeleching process has amplitudes, A_1, between 0.012 ± 0.0004 and 0.022 ± 0.0004 with relaxation time constants oscillating around 160 ±10 fs. A similar behavior for the τ_1 values is found in the 1.56-2.03 eV range whilst A_1 decreases from 0.04 ± 0.03 at 1.56 eV to 0.012 ± 0.0002 at 1.88 eV. The intermediate PA relaxation shows a more complex behavior having an almost vanishing amplitude, A_2, for the signals collected at 0.75 eV and 0.78 eV. The TT signal at 0.88 eV and 1 eV starts to show non negligible amplitudes (-0.0006 and -0.0005 respectively) and with about ten percent relative error. Their τ_2 values are of about 750 fs. For the measurements in the 1.56-2.01 eV range A_2 shows a significant increase for measurements equal or above 1.76 eV being in the range -0.009, -0.004 with a a relative error of about 20%. τ_2 values oscillate around a 660 fs mean value. It is worth to note that dispite the oscillation of the best fit coefficient A_2 and τ_2 the TT signal is well interpolated

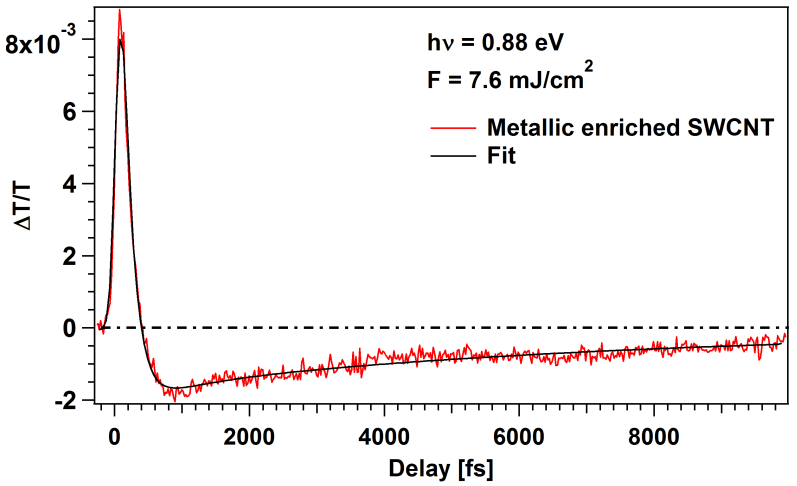

Figure 4.11: TT signal collected at an excitation energy of 0.88 eV and with a pump fluence of 7.6±0.25 mJ/cm^2 (red line). The black line is the best fit obtained using eq. (4.3)

only using the third exponential term and the variation of the A_3 value, reported in fig. 4.12, cannot be avoided by means of A_2 and τ_2 variations.

A_3 clearly increase with the the excitation energies. Its peak value is reached at 1.81 eV, about the M11 exciton resonance (at 1.75 eV). Above 1.81 eV A_2 stabilizes at 0.0025. Since during our measurements we changed both the pump laser fluence and the pulse photon energy the effective amount of energy deposited in the illuminated volume changes for each data point. We define an effective fluence as $F_{eff} = AF$ where A is the static absorption of the SWCNT film. The effective fluence can be viewed as an average fluence seen by the sample neglecting the actual excitation anisotropy of the SWCNT layer. We define this parameter in a similar manner of the average total energy per pulse used in the estimation of the equilibrium temperature. In fig.4.12a each A_3 value is labeled with is corresponding E_{eff} (see fig.4.12 caption). It is evident that the lowest amplitudes of the slow photoabsorption tail corresponds to the highest effective fluences. Moreover the smallest values of A_2 occurs for excitations at low photon energies. This behavior is highlighted in fig.4.12b where

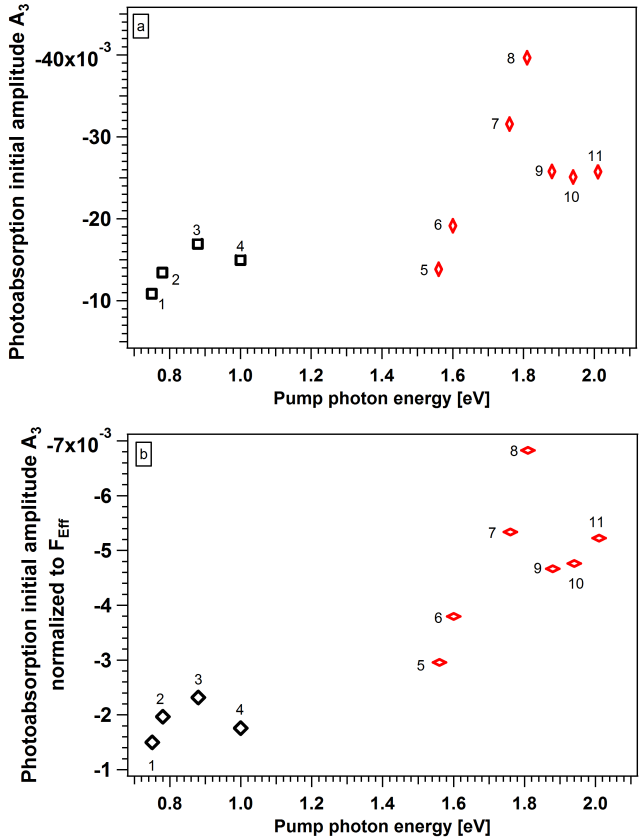

Figure 4.12: (a) A_3 excitation energy dependence. Each data point is labeled with a numerical tag for identification proposes. The effective fluence (see text) of point 1 is $F_{eff}1 = 7.2$ mJ/cm^2, and similarly $F_{eff}2 = 6.8$ mJ/cm^2, $F_{eff}3 = 7.3$ mJ/cm^2, $F_{eff}4 = 8.5$ mJ/cm^2, $F_{eff}5 = 4.6$ mJ/cm^2, $F_{eff}6 = 5.0$ mJ/cm^2, $F_{eff}7 = 5.9$ mJ/cm^2, $F_{eff}8 = 5.8$ mJ/cm^2,$F_{eff}9 = 5.5$ mJ/cm^2, $F_{eff}10 = 5.2$ mJ/cm^2, $F_{eff}11 = 4.9$ mJ/cm^2. For all the data points the statistical error given by the fitting software is within the marker width. (b) A_3 values normalized to the corresponding F_{eff} value. The difference between the two excitation energy regimes is highlighted.

the A_3 value is normalized to its F_{eff} value. If the PA signal do not comes from transitions involving hot Dirac fermions but instead is given by the exciton states absorption a similar behavior could be expected, however we tend to exclude this possibility. An exciton nature of the PA tail implicates that for low excitation energies a significant amount of excitons are populated by means of scattering processes, or by direct two photon absorption. Two photon absorption in semiconducting nanotubes was detected by F. Wang et al. using 130 fs light pulses with a fluence of 0.5 mJ/cm^2 [18]. Even if a two photon excitation process is probable at our pump fluences, this assignation does not explain the slow photobleaching signal observed with a 0.76 eV probe (fig4.10) and implies an exciton lifetime of about 7 ps. Such a long relaxation time constant is not commonly observed in SWCNT aggregates and is about 4 times slower than the exciton lifetime obtained from our TT measuraments on semiconducting enriched SWCNT, performed in similar experimental conditions (see next paragraph). Moreover the strong coupling with the underlying continuum in metallic SWCNT is commonly considered the cause of photoluminescence quenching in SWCNT aggregates. In bundled metallic and semiconducting SWCNT mixtures the carriers tunneling from S-SWCNT toward M-SWCNT reduces the carriers lifetime to about 1 ps [10].If the nature of the PA signal is indeed related to the excitation of hot Dirac fermions in SWCNT the photon energy and F_{eff} dependence of A_3 can be the signature of a carrier multiplication effect. This intriguing possibility was recently theoretically and experimentally investigated in Graphene [111,112]. In this case the photoexcited electrons in the conduction band can interact with valence band electrons giving rise to an impact ionization process (II). A sufficiently energetic electron in the conduction band looses its energy promoting another valence electron in the state continuum near the Fermi energy. The final outcome is an increased number of electrons in the conduction band with respect to the one due to the initial photoexcitation process. Impact ionization in semiconducting SWCNT was proposed by Ueda et al. [113] et al. to explain the energy and fluence dependence of their transient transmittivity signals. In this case II was observed for excitation energies in the near uv range. Due to the presence of bandgaps a high photon energy is needed to fulfill energy and momentum conservation during the II process but in metallic SWCNT the lack of bandgaps could lead to II even for lower excitation energies. If only electron-electron interaction are considered, electron

relaxation process can involves the generation of electron-holes pairs to which the energy and momentum of the decaying electron is transferred, moreover, in case of metallic armchair nanotubes, the electron-hole excitation spectrum has the same basic structure of the Graphene one. [41] The electron-hole excitation spectrum is the density of the possible electron-hole excited states at a given energy and momentum. The overlap between this spectrum with the electron energy loss spectrum defines the phase space volume where the decaying electrons can excite an electron hole pair [41]. Recent theoretical works on graphene have predicted a carrier multiplication coefficient greater then 4 at least for low excitation densities [111]. The similarities between the M-SWCNT and the graphene electron hole excitation spectrum lead us to suggest that an efficient carrier multiplication can take place in metallic tubes as well. In this case the the higher PA amplitude between 1.75 and 2.01 eV but at a "low" E_{eff} can be the signature of the carrier multiplication process since the final photoexcited population density in the vicinity of the Fermi level turns out to be greater than the one excited directly with pump pulses in the 0.75-1.0 eV range and at an higher effective fluence.

4.5 Semiconducting enriched SWCNT: results and discussion

In fig.4.13 the transient transmittivity signal collected with a probe energy of 0.76 eV and at an excitation energy of 1.55 eV is reported. In this case the probe energy is nearly resonant with the E11 transition and only a strong photobleaching signal is detected.

Despite the out of resonance excitation fast intersubband relaxation processes populates the first exciton state within the laser crosscorrelation timewidth. In order to analyze the population dynamics we fit the transient absorption variation with a set of coupled rate equations. The transient absorption (TA) ΔA can be directly calculated from the ΔT/T signal using the relation

$$\Delta A = -ln\left(1 + \frac{\Delta T}{T}\right)$$

and is interpolated using the following rate equations

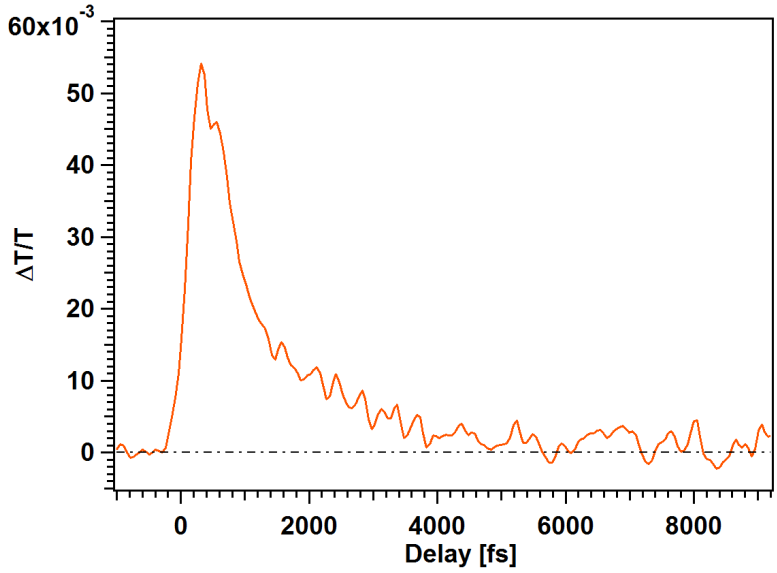

Figure 4.13: TT signal collected at an excitation energy of 1.55 eV and with a pump fluence of F=8.90±0.06 mJ/cm^2 (F_{eff}=5.00±0.03 mJ/cm^2).

$$\begin{cases} \frac{dN_0}{dt} = -p(t)\sigma_{02}N_0 + p(t)\sigma_{02}N_2 + \frac{1}{2}k_a N_1^2 + k_{10}N_1 \\ \frac{dN_1}{dt} = +k_{21}N_2 - k_a N_1^2 - k_{10}N_1 \\ \frac{dN_2}{dt} = p(t)\sigma_{02}N_0 - p(t)\sigma_{02}N_2 + \frac{1}{2}k_a N_1^2 - k_{21}N_2 \end{cases} \tag{4.4}$$

where N_0, N_1, and N_2 represents the populations of the ground state, the first exciton sate and the second exciton state respectively. In the model described in eq.(4.4) it is assumed that the pump pulse at 1.55 eV mainly excites the the second exciton level E22. The laser excitation is described by a Gaussian function $p(t)$ with the pulse crosscorrelation timewidth. The amplitude of $g(t)$ is defined by the relation $\int p(t)dt = F$ where F is the laser fluence in photons/cm^2, and the rate of the population density variation is calculated using the absorption cross-sections σ_{02} of the sample at the pump energy. Both the absorption and the stimulated emission are taken into account. Relaxation processes from E11 toward the ground state and from E22 toward E11 are described

by the rate constants k_{10} and k_{21} respectively. Simple exponential relaxation dynamics are considered and no time dependent rate constants are introduced. Due to our high excitation fluence we expect that exciton-exciton interaction can take place, to account of this phenomenon we introduce the time independent exciton-exciton annihilation rate K_a. We assume that one of the exciton pairs involved in the annihilation process is promoted in the E22 state. The absorption cross section σ_{12} is directly evaluated from the static transmission spectrum (fig.4.2) using the relation $\sigma = -ln\,(T)\,/N_c d$ where d is the sample thickness (92 nm) and n_c is the number of carbon atoms per unit volume. For our sample N_c is estimated in about 2×10^{22} atoms/cm^3. From this relation we get an absorption cross section of 4.2×10^{-18} cm^2 at 1.55 eV. The σ value for the first and the second exciton transitions are 8.9×10^{-18} cm^2 and 6.8×10^{-18} cm^2 respectively. Even if no background subtraction is attempted, the cross section value for the first exciton transition is similar to the one reported in literature for isolated (6,5) tubes which is 7×10^{-18} cm^2 [114]. Following [40] we solve the system (4.4) for the population density per unit length of the carbon nanotubes N_i (i=0,1,2). N_i is related to the carbon atom density of the sample, N_c, by the relations $N_i = n/w$ and $w = (dN_c)\,/\delta$ where n is the population density per unit area and δ is the carbon atom density per unit length of the SWCNT in the sample. For a (17,0) tube, that as a diameter of 1.33 nm, δ is 1.59×10^9 atoms/cm. w can be viewed as the total tubes length per unit area of the sample. In fig.4.14 the transient absorption of signal together its best fit using (4.4) is displayed.

The signal is interpolated using the relation $\Delta A = wN_1\sigma_{12} - wN_1\sigma_{probe}$ where σ_{probe} is the absorption cross section at the probe energy (0.76 eV) and σ_{12} is the absorption cross section for the E11→E22 transition. The positive term is introduced since the the probe energy is almost resonant with the latter transitions and thus a photoabsorption signal is expected to be superimposed on the E11 bleaching [46]. The best fitting parameters are $k_{21} = 1.2 \pm 0.4 \times 10^{-2}$ fs^{-1} , $k_{10} = 3.1 \pm 0.6 \times 10^{-4}$ fs^{-1} and $\sigma_{12} = 3.8 \pm 0.3 \times 10^{-18}$ cm^2. Surprisingly the exciton-exciton annihilation rate constant is only $2 \pm 0.8 \times 10^{-4}$ nm/fs, more than one order of magnitude smaller that the values commonly reported in literature [40]. Despite this discrepancy it is worth to note that to obtain a good interpolation the EEA term is necessary and the initial steep decay of the signal can not be recovered only by adjusting the dissipative terms k_{10} and k_{21}.

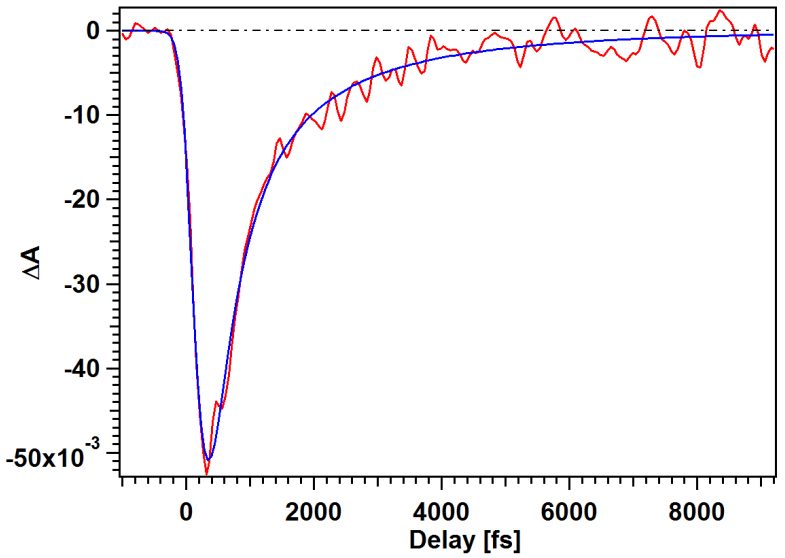

Figure 4.14: Transient absorption signal from the semiconducting enriched SWCNT film (red line). F=8.90±0.06 mJ/cm^2 (F_{eff}=5.00±0.03 mJ/cm^2). The blue line is the best fit interpolation using the rate equation model (4.4)

Moreover due to the nonresonant excitation the initial exciton density N_2 is clearly overestimated and part of the pump energy is dissipated in the phononic degrees of freedom before being converted into an exciton population. From the analysis we extract a E11 relaxation time constant of 3.2 ± 0.5 ps. This results further support the idea that the long photobelachig transient found in the metallic eneriched SWCNT film, at the same probe energy, with an estimated time constant of about 7 ps, is not due to a residual SWCNT contamination of the sample. (Fig.4.10).

In Fig.4.15 the transient transmittivity signals collected varying the pump photon energies in an interval between 1.74 and 2.04 eV are reported. For these measurements the laser pump fluence is kept at 8.1 mJ/cm^2 and the probe energy is 1.55 eV. All the spectra are characterized by a fast photobleaching signal near zero delay times followed by a slower photoabsorption tail which relax on a few picosecond time scale.

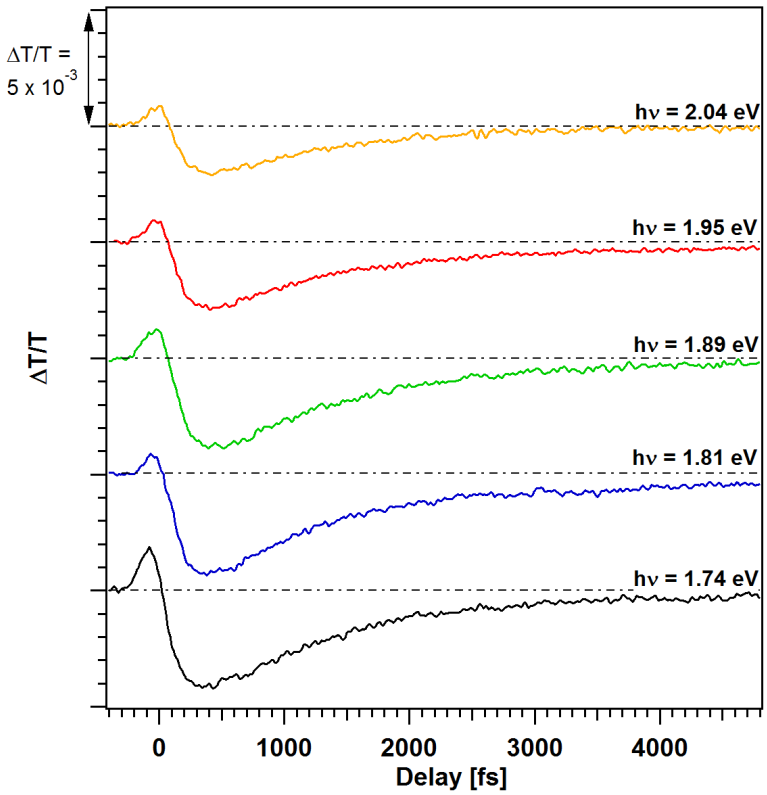

Figure 4.15: Transient transmittivity signal from the semiconducting enriched SWCNT film. F=8.1±0.25 mJ/cm^2. Excitation photon energies are between 1.74 and 2.04 eV. Each signal is labeled with its pump photon energy. Tracks are shifted for clarity.

In fig.4.16 we report the signals collected for excitation energies of 1.60 and 1.71 eV on a different sample point. Whilst the overall shape of the TT relaxation does not change, a small variation of the signal amplitude can be observed with respect to the previous dataset (fig.4.15).

These amplitude differences are due to sample inhomogeneity, possibly small thickness variation are found changing the sample point even if all the other

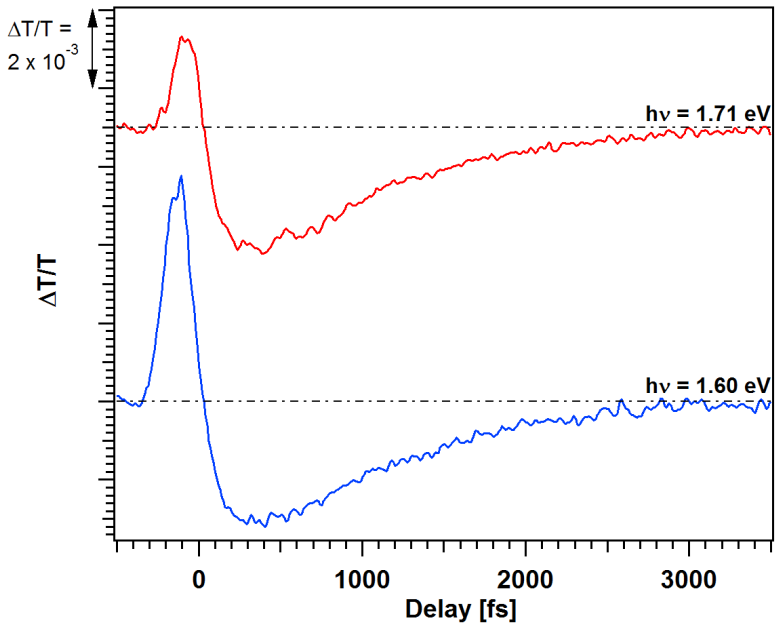

Figure 4.16: Transient transmittivity signal from the semiconducting enriched SWCNT film. F=8.1±0.25 mJ/cm^2. Excitation photon energies are between 1.71 and 1.60 eV. Each signal is labeled with its pump photon energy. Tracks are shifted for clarity.

experimental parameters are equal. It is worth to note that no significant sample point dependence of the TT signals is detected on the metallic enriched SWCNT film. As for the metallic enriched sample (fig.4.6) the weight of the photobleaching transient relative to the photoabsorption peak value increases as the excitation energy approaches the probe energy. In fig.4.17 the TT signal collected for excitation energies of 0.75 , 0.88 and 1.0 eV are reported.

As for the previous measurements the signals present both a fast photobleachig and a slower photoabsorption tail but, for this excitation energies, the photobleaching spike is shifted with respect to the beginning of the optical transient. Our pump energies are prevalently out of resonance with the exciton transition of the sample. Exciton absorption peaks for the S-SWCNT sample

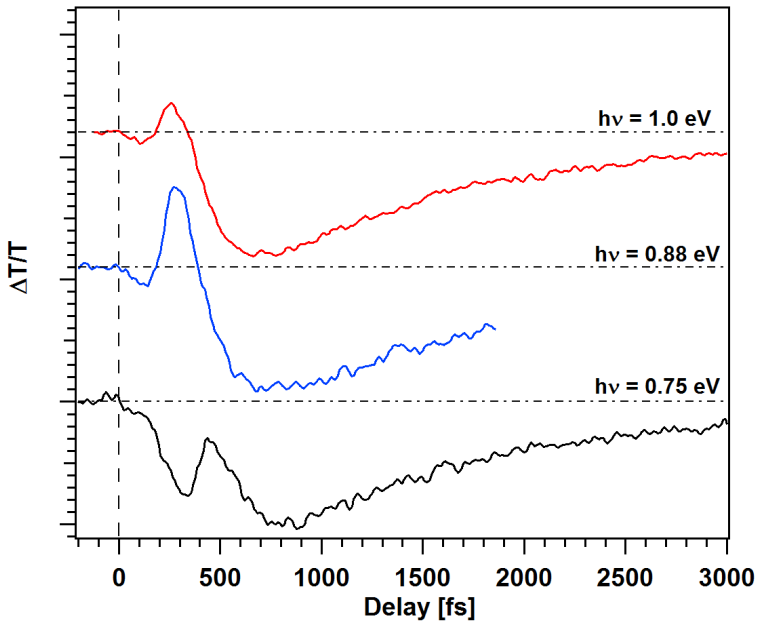

Figure 4.17: Transient transmittivity signal from the semiconducting enriched SWCNT film. F=22.9±0.25 mJ/cm^2. Excitation photon energies are 0.75, 0.88 and 1.00 eV. Each signal is labeled with its pump photon energy. Tracks are shifted for clarity and the zero delay time is arbitrarily fixed at the beginning of the optical transient and are normalized to the negative peak amplitude.

are localized at 0.66 and 1.19 eV (fig.4.2) so only the 1.0 eV and the 0.77 eV pump pulses are within the E22 and E11 linewidths. Despite the out of resonance excitation we expect that a significant exciton population is excited in our sample, as demonstrated by the strong photobleaching signal found at a probe energy of 0.76 eV (fig.4.13). Moreover off resonance population of the the exciton transitions is commonly observed in time and energy resolved transient transmittivity experiments when the pump energy is higher than the transitions energy, such as in our case. Also our 1.55 eV probe is out of resonance with the main absorption peaks, being localized between the E22 transition and the peaks due to the residual metallic SWCNTs. In this experimental condition we

expect that the TT signals mainly come from transitions between the E11 and the E33 exciton states, which will results in a photoabsorption signal, being the probe nearly resonant with the E11-E22 transition [46]. For excitation energies in the 0.77-1.0 eV range, the photobleaching spike shifts from the zero delay time. This behavior is not observed for metallic tubes (fig.4.4). Fast transients near zero-delay times under nonresonant excitations have been previously observed in isolated SWCNT by S. Tao et al in [115] and ascribed to a stark shift of the exciton transitions. Since our probe energy is in a local minim of the absorption spectra our experimental sensitivity to the exciton lineshifts is small and an accurate timing of the pump and probe crosscorrelation, using a nonlinear crystal placed at the sample point, shows that the maximum photobleaching amplitude is reached after the pulses coincidence. This is in agreement with a population induced χ^3 effect [116] and lead us to ascribe the fast transient to state filling even in the 0.77-1.0 eV energy range. In order to address the nature of the fast photobleaching transient we fit the transient absorption spectra associated with the signals reported in fig.4.15,4.16 and fig.4.17 with a rate equation model similar to the one reported in (4.4). For the measurements performed in the 0.77-1.0 eV excitation energy range the rate equation system is modified by considering resonant excitation of the E11 or the E22 transition according to the pump energy. Also two photon excitation of the E22 state and the E11 absorption of the pump photons are introduced as fitting parameters. Assuming that the fast photobleaching signal is due to an exciton population of the E22 level whilst the long PA tail is due to the E11→E33 transition, the TA signals are fitted with $\Delta A = wN_1\sigma_{13} - wN_2\sigma_{probe}$ where σ_{13} is the absorption cross section for the E11→E33 process and σ_{probe} is the absorption cross section at the probe energy (1.55 eV). Despite these modifications, the model is incapable to satisfactory interpolate all the TA signals, giving an unconfident set of absorption cross sections σ_{13}, which varies widely form one TA signal to the other. The unsatisfactory outcome of the fitting model lead us to propose that the fast photobleaching transient is due to a transient filling effect on of the state continuum below the E22 transition as proposed for the metallic enriched SWCNT. When the excitation energy is higher than the E22 transition, i.e. in the 1.60 - 2.04 eV, the direct photoexcitation of the band state is possible even for isolated semiconducting SWCNT as demonstrated in [19] moreover the tube-tube interactions and the residual bundling could increase the continuum absorption

cross section by altering the SWCNT band structure [10]. In this case the apparent shift of the PB transient (Fig.4.17) for excitation energies in the 0.77-1.0 eV range can be due to the presence of bandgaps in the semiconducting tubes. For these low energies no direct excitation of the sate continuum is possible and a build-up of the E11 population is needed before a significant population is promoted in the higher lying states upon absorption of a second pump photon. Obviously also the exciton-exciton annihilation process is capable to promote a population on an excited level, still since both these processes are included in our rate equation model we underline that the the transient bleaching is not satisfactory described taking only the exciton effects into account.

As for the previous case we interpolate all the TT signals with an empirical fitting function of the form

$$\frac{\Delta T}{T} = G(t) * \left(A_1 e^{-\frac{t-t0}{\tau_1}} + A_2 e^{-\frac{t}{\tau_2}} \right) \tag{4.5}$$

The first exponential decay, which accounts for the transient bleaching, is translated by a delay $t0$ with respect of the second one in order to describe the relative shift observed in the 0.77-1.0 eV measurements. An exemplificative fit is reported in fig.4.18

Using this empirical function the potoabsorption dynamics relaxation time constants result to be between 1100 and 1400 fs. The first photobleaching time constant oscillates around a 100 fs mean value. The difference between the PA time constant obtained with this empirical function and the E11 lifetime obtained with the rate equation model (4.4) suggests that a different mechanism aside the E11→E22 absorption may contribute to the PA signal at this probe energy (1.55 eV). Moreover from the analysis reported in fig.4.14 we found that in the intermediate delay ranges the exciton exciton annihilation term plays an important role and a good fit using the rate equations model is obtained only by introducing it. The deviation from the simple exponential relaxation is not contemplated in the empirical function (4.5) and could result in a difference between the rate constants of the PA dynamics. In order to clarify this behavior further experimental efforts are needed. It is still worth to note that no difference between the PA relaxation time constant of the metallic enriched sample are found exchanging the roles of the pump and the probe beams and comparing the measurements taken with a 1.55 eV probe a difference of about 4 times in the relaxation time constant is measured. For completeness in fig.4.19a we report

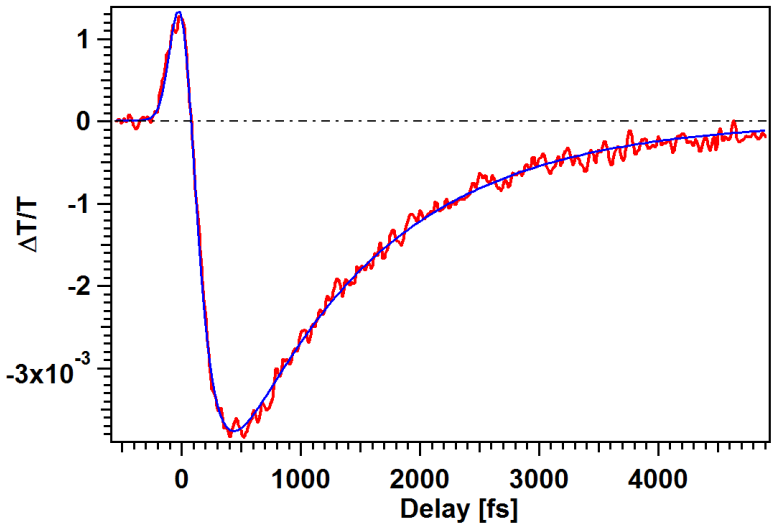

Figure 4.18: Transient transmittivity signal from the semiconducting enriched SWCNT film. F=22.9±0.25 mJ/cm^2. Excitation photon energy is 2.04 eV. The blue line is the best fit results using eq (4.5)

the fluence dependence of the PB signal amplitude for an excitation energy of 1.82 eV.

The amplitude is extracted from the fitting results using (4.5) and its values are displayed versus F_{eff}. In fig.4.19b the PA initial amplitude versus F_{eff} is reported. In both graphs the best linear fit (black line) is also displayed. The deviation from the linear behavior is evident, in particular for the PA amplitude variation. Sub-linear amplitude variations of the PA signal amplitude are expected in case of nonlinear phenomena such as exciton-exciton annihilation [40]. In fig.4.20a and fig.4.20b the F_{eff} dependance of the PB and the PA signal amplitude for an excitation energy of 0.88 eV is reported. As for the previous case the deviation from the linear behavior (black line) is evident.

The PB magnitudes show a smaller deviation from the ideal linear fluence dependence of a χ^3 process with respect to the associated PA amplitudes and the best fit slopes are different for the two excitation energies. The slope for the

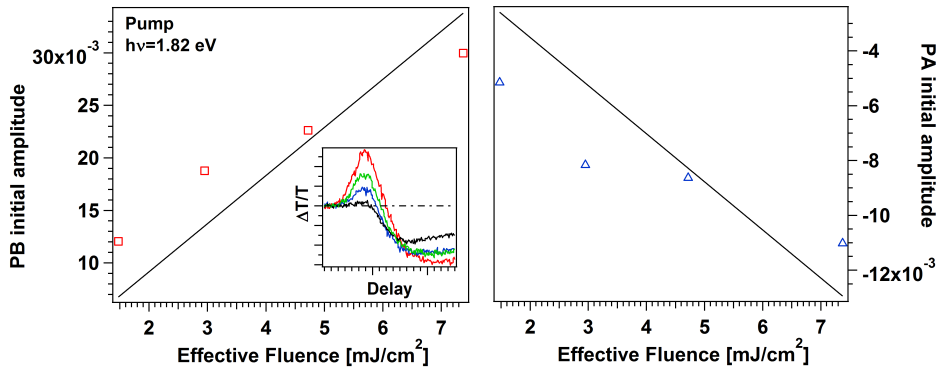

Figure 4.19: Effective fluence dependence of the photobleaching (PB) and the photoabsorption (PA) initial amplitudes at a pump photon energy of 1.82 eV. Black lines are linear interpolations with a zero intercept. On the inset the TT signals are displayed.

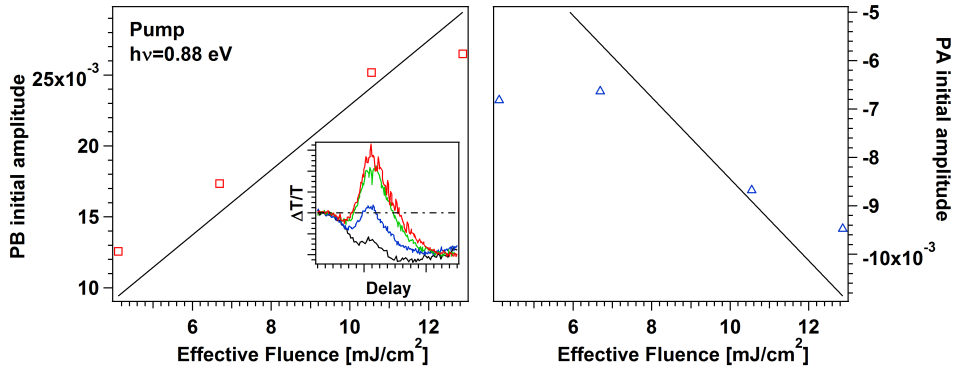

Figure 4.20: Effective fluence dependence of the photobleaching (PB) and the photoabsorption (PA) initial amplitudes at a pump photon energy of 0.88 eV. Black lines are linear interpolations with a zero intercept. On the inset the TT signals are displayed.

0.88 eV excitation is of about 2×10^{-3} cm^2/mJ whilst for the 1.82 eV pump the

changes to about 4×10^{-3} cm^2/mJ. Besides these results in order to fully clarify the nature of the photobeaching signal further experimental efforts are needed.

4.6 Conclusions

In conclusion we performed time resolved transmittivity experiments on ultarpure metallic enriched and semiconducting enriched free standing SWCNT films tuning the pump energy in a wide range. The TT signals show remarkably differences at long delay times where, for the metallic enriched sample, a slow photoabsorption dynamics with a relaxation time constant of 6.7 ps is found. This dynamics is not present in the semiconducting enriched sample where only an absorption signal with a mean time constant of 1.2 ps is present. The PA relaxation time constant of the metallic enriched sample does not show a dependance on the pump photon energy and is present even for nonresonant excitation of the M11 transition. By estimating the equilibrium temperature of the photoexcited carriers in the metallic tubes we are able to exclude a pure thermal effect, such as an exciton thermal line shift, as the origin of the observed photoabsorption signal. We suggest that the origin of the PA transient as to be found in optical transitions involving an hot Dirac fermion population excited in the vicinity of the Fermi level which can be promoted in higher lying electronic states upon absorption of probe photons with an energy greater than 0.75 eV. Starting from this assignation and considering the pump energy and fluence dependence of the PA signal amplitude we found evidence of a possible carrier multiplication process taking place in the metallic carbon nanotubes. For excitation energies above 1.6 eV the PA signal magnitude is greater then for excitation energies in the 0.75-1.0 eV range even if the total absorbed energy per pulse is about 1.5 times smaller. Carrier multiplication is currently theoretically and experimentally investigated in graphene and compelling evidences of its occurrence in semiconducting carbon nanotubes has been already found for excitation energies in the ultraviolet spectral range. If confirmed, this result has great relevance for photovoltaic application since in an opportunely designed device carrier multiplication reduces the energy losses due to phonons interactions and could potentially increase both the quantum efficiency and the effective power conversion efficency of the system.

Chapter 5

Interface-coupled relaxation dynamics in carbon nanotube-Si hybrid solar cells

The role of carbon nanotubes (CNTs) in the heterojunction solar cell based on CNTs deposited on n-Si wafer is investigated by transient optical spectroscopy. Thanks to the different optical response of these two materials, we are able to show that the holes generated in the Si depletion layer, by the femtosecond laser pump, transfer from Si to carbon nanotubes within two picoseconds, driven by the built-in heterojunction potential. Furthermore the CNTs are found to play an active role in the junction, and do not act only as nanosized channels for charge collection and transport to the electrodes. The results here reported show that transient optical spectroscopy is a powerful technique for measuring the processes occurring immediately after the photogeneration of electron-hole pairs in a SWCNT/n-Si heterojunction solar cell.

5.1 Introduction

One of the key aspects underlying the application of novel materials in photovoltaic devices is the understanding of the steps immediately following the arrival of the light. The overall efficiency of a photovoltaic device is mainly governed by two factors: absorption efficiency and its internal quantum efficiency. The former is influenced by the capability of the active material to efficiently absorb photons in the solar spectrum wavelength range. The latter is mainly determined by the diffusion, dissociation and transfer of the excited charge. These processes occur on ultrafast time scales. Information on this timescale is difficult to access and a direct measurement of charge transfer dynamics upon light excitation is matter of many of the current research efforts. In this framework, time resolved optical spectroscopy is a powerful tool for exploring the exciton dissociation processes or the dynamics following hole-electron pair excitation, and has been successfully applied, among many others, to dye-sensitized heterojunction solar cells [117] and polymer based heterojunctions [118, 119]. On the other hand, much of the current research on n-Si/SWCNT solar cell devices focuses on the time averaged properties and only a little information about processes actually occurring on fast timescales is available. In this chapter we follow the process of charge separation and injection across the n-Si/SWCNT heterojunction using time resolved optical reflectivity measurements, exploiting the different transient response of the SWCNT and the n-Si layers.

The CNT/n-Si interface has shown to be a suitable heterojunction for solar cells showing efficiencies up to 10-13% [29, 29, 120]. The solar cells consist of a semitransparent thin film of nanotubes conformally coating a n-type crystalline silicon substrate to create high-density p-n heterojunctions [120] or Schottky junctions [121] between nanotubes and n-Si to favor charge separation and extract electrons (through n-Si) and holes (through nanotubes). (See chapter one). The key point is that the role of CNTs in the CNT/n-Si heterojunction is not completely understood. The first possibility is that CNT film behaves only as a transparent coating and that, when exposed to light, photons absorbed within the underlying n-Si generate electron-hole pairs that are driven in opposite directions by the field associated with the built-in potential in the depletion layer with holes extracted on the CNT film side and electrons on the n-Si side [121]. Nonetheless, theoretical studies have predicted photoconductivity of individual

nanotubes [122,123] and appreciable photocurrent has been observed when nanotube films were irradiated by light. [51] Therefore the second possibility is that CNTs serve both as photogeneration sites and transparent coating for charge carriers (holes) transport. The goal of this work is to perform time resolved optical spectroscopy directly on a SWCNT/n-Si based solar cell, in order to clarify the role of CNTs in the SWCNT/n-Si heterojunction investigating the relaxation dynamics of the photoexcited carriers at the interface. As the laser pump fluence was selected to hinder a transient optical response from the bulk silicon, our spectroscopy set-up is tuned to excite prevalently the SWCNT layers or their electronic states involved in the junction formation. In order to single out the effects of the junction, the transient optical response from the cell has been directly compared with the ones collected on the same type of SWCNT deposited, in the same experimental conditions, on a glass substrate. Moreover, by tuning the pump photon energy across the Si absorption edge, we have extrapolated the role of SWCNT film. The results show that for excitations below the Si absorption threshold, both samples display the same behavior, and therefore the response is determined by the SWCNT layer alone. In turn, for energies above the Si absorption threshold, the SWCNT/n-Si junction displays a slow dynamics, along with an enhancement of the photobleaching effect. This is recognized as an intrinsic behavior of the junction, not found on the SWCNT/Glass interface, and is rationalized as a charge transfer (holes) from Si to SWCNT across the junction, depleting the occupied levels of SWCNT. This interface charge transfer dynamics develops within 2 ps, driven by the built-in field of the junction.

5.2 SWCNT/n-Si heterojunction

The heterojunction solar cells used in these experiments are provided by the group of Paola Castrucci at the Roma Tor Vergata University. The n-silicon substrate, obtained from FBK (Fondazione Bruno Kessler, Trento, Italy), consisted in 5×10 mm^2 slices of a SiO_2-passivated (thickness 300 nm) n-type Si(100), with a resistivity of $3-12$ Ohm·cm and an aluminum ohmic back contact. The oxide layer was patterned by a lithographic process with a positive resist and subsequent chemical etching in order to obtain a 5×5 mm^2 bare silicon window in the middle of two SiO_2 steps.The chemical etching was carried out wetting

for 5 minutes the bare SiO_2 with a HF/NH_4F buffer solution. This patterning of SiO_2 layer allows to create nanotube/n-Si multijunctions in the 5×5 mm^2 Si-n window and, at the same time, to insulate the silver paste deposited on the nanotube film from the n-Si underneath so to avoid short circuits between the metal electrode and the Si. A scheme of the fabricated device is shown in Fig.5.1a together with a picture of the cell used in these experiments (Fig.5.1b).

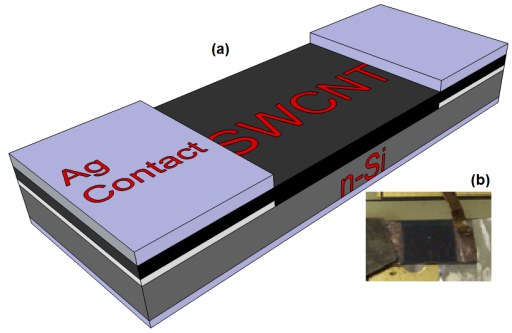

Figure 5.1: a) Schematic representation of the structure of the SWCNT/n-Si heterojunction solar cells used in this experiments. b) 5.5 ml solar cell picture.

SWCNT films on n-type silicon and on glass were obtained percolating a SWCNT dispersion in water through a cellulose acetate membrane filter (PALL corp. 0.45 μm pores). SWCNT powder (>90% in carbon, >70% in SWCNT (various chirality), diameter ranging between 0.7-1.4 nm) has been obtained from Sigma-Aldrich. In such a powder, the percentage of metallic nanotubes has been estimated to be not less than 65% [31] The nanotube dispersion was prepared sonicating about 100 μg of a SWCNT powder in a sodium dodecylsulfate (SDS) (98% Sigma Aldrich) solution in water, concentration of 3% in weight. After 1 hour of sonication, the dispersion was left to settle down and the clear supernatant containing unbundled nanotubes was separated from the precipitate and used to fabricate the film. The filtration was carried out in a vacuum filtration assembly. Once the SWCNT film is casted on the membrane, in order to remove the residual SDS, it is washed several times with deionized water and finally with an ethanol/methanol/water mixture (15:15:70 in volume). Different film thicknesses can be obtained by varying the amount of the

filtered solution. The SWCNT film is transferred on the patterned Si substrate pressing the SWCNT coated membrane onto the Si/SiO_2 surface. The procedure, though properly modified has been derived from literature. [124], [125]. The cellulose acetate membrane lying on top of SWCNT film is removed by dissolution in acetone (3-4 washes) and finally by rinsing with isopropanol. The SWCNT film was contacted creating two silver paint pads on top of the insulating SiO_2 areas. During the deposition of the SWCNT film on Si, particular care is taken to avoid the contact between the film and the side of the silicon that would eventually cause electron leakage. For the experiment reported in this chapter we used two cells characterized by different SWCNT film thicknesses labeled, by the amount of filtered solution used in their preparation, as 5.5 ml and 1.5 ml. The cells external quantum efficiency spectrum, in a static illumination condition, was measured by a dedicated set-up equipped with a 150 W Xenon lamp as light source and a monochromator. The number of the incident photons is evaluated in terms of the power density of the Xe lamp, measured by a calibrated Si photodiode and acquired by a lock-in amplifier locked to the Xe lamp modulation signal. The resulting cell current is also detected by the lock-in amplifier. In Fig5.2 a comparison between the EQE spectra for the two samples and the EQE spectra of a conventional p-n silicon solar cells is reported

The static EQE for the 5.5 ml sample varies between the 10% and 35% in the explored energy range (300-1000 nm) whilst for the 1.5 sample the EQE values are between the 30% and the 60%. The SWCNT/Si-n EQE spectra shape resemble the p-n cell one, suggesting that the photoexcited electron-hole pairs generation and dissociation process take place in the silicon depletion region of the heterojunction. It is worth to note that even if the EQE of the conventional silicon p-n junction is greater than the SWCNT/n-Si ones for wavelengths below 470 nm the 1.5 ml cell shows an enhanced EQE for wavelengths in the blue part of the visible spectrum. The spectral EQE extension in the blue part of the spectrum is analyzed in detail in the work of Del Gobbo *et al.* [31] for a set of SWCNT/n-Si built with the same materials and procedures of the samples used in this work. In the blue and UV part of the spectrum the EQE of the silicon cell is mainly limited by the high surface recombination velocity and by the high optical absorption coefficient which confines the photoexcited carriers in a thin region close to the front surface. The increased EQE of the SWCNT/n-Si junction is ascribed to a reduction of the surface recombination velocity for

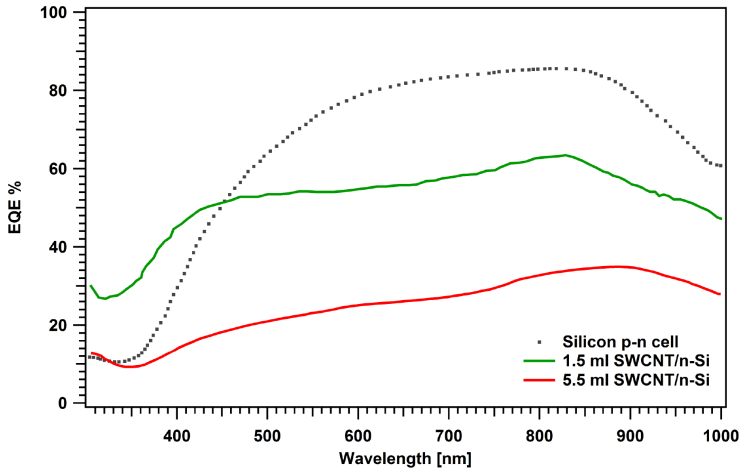

Figure 5.2: External quantum efficiency spectra of the 5.5 ml (red line), 1.5 ml (green line) SWCNT/n-Si cells and of a conventional p-n silicon solar cell (dark grey points)

charge carriers generated in the silicon underneath the SWCNT layer and to the comparable scale of the SWCNT layer thickness and the electron diffusion length in the carbon nanotubes. The latter also account for the low EQE value in the blue part of the spectrum of the 5.5 ml cell, which is characterized by a thicker SWCNT layer. The power conversion efficiency η of the two heterojunctions was determined from their I-V characteristic using a solar simulator For the 5.5 ml cell $\eta = 1.51\%$ whilst for the 1.5 ml sample $\eta = 0.26$ %. The lower value of the power conversion efficiency for the 1.5 ml sample, which has an higher EQE. Fig.5.2 could be due to the higher sheet resistance of the thin SWCNT layer, wich is in the order of 1.4 $K\Omega$, increasing the internal resistance of the device and thus lowering the maximum available voltage for an external load.

5.3 SWCNT/Glass reference sample

In order to clarify the role of the junction formation in the hybrid solar cell we have performed a set of control experiments on a SWCNT layer deposited onto a lab glass slide. In this systems no CNT/substrate heterojunctions are

expected to be present due to the high band gap of the glass and its insulating properties. The SWCNT/Glass sample has been prepared with the same type of carbon nanotubes, chemical and transfer procedure. The used amount of the parent solution is 4.5 ml, we thus expect that the average film thickness is sightly lower than the one of the 5.5 ml SWCNT/n-Si cell. This sample is also used to characterize the static optical properties of the SWCNT film via optical transmission experiments. In fig.5.3 the absorption spectra of the SWCNT layer is reported.

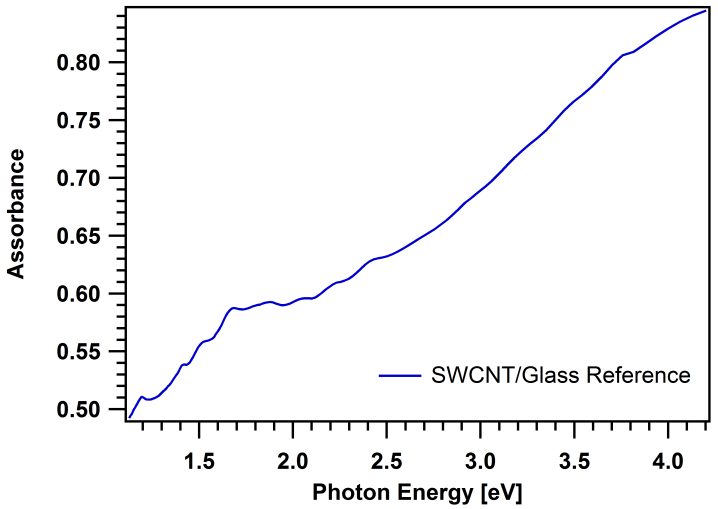

Figure 5.3: Static optical absorption spectra of the SWCNT/Glass reference sample. The absorption magnitude scale is an estimation based on transmittance measurements performed on our SWCNT/Glass reference sample and neglecting the interface reflectance.

The absorption spectra magnitude scale is only an estimation since it is obtained from the average of multiple transmittance measurements performed on several points of the reference sample and neglecting the reflectance contribution. The absorption data show the presence of the characteristic peaks due to the exciton transitions in the SWCNT. Due to the large diameter and chirality dispersion of the tubes as well as residual sulfactant and intertube interactions

sharp exciton transition cannot be clearly resolved. In [31] by crossing the absorption peaks positions with the radial breathing mode frequency (from Raman scattering measurements) a chiralty assignment is performed. The SWCNT layer is mainly composed of (8,5), (7,7), (9,9), (11,8), (9,3) metallic SWCNTs and (9,8) (11,7) (10,2) (13,6) semiconducting tubes. As reported in the previous paragraph the metallic tubes contents is no less than 65%.

Laser system Time resolved optical measurements have been performed with the two laser systems described in chapter one. One-color transient reflectivity (TR) experiments in the low fluence regime have been carried out with a cavity dumped Ti:Sapphire oscillator (Coherent Mira 900 together with an APE pulse switch), producing 120 fs, 1.55 eV light pulses. The pump beam diameter at the sample position is 50 μm, corresponding to fluences in the 0.1 - 0.5mJ/cm^2 range. TR experiments in a two-color variable-pump and fixed-probe configuration have been performed by using a 1 KHz amplified Ti:Sapphire laser system capable to deliver 0.5 mJ, 150 fs, 1.55 eV light pulses, together with a traveling wave optical parametric amplifier (TOPAS). The probe energy is kept fixed at 1.55 eV whilst the pump energy is tuned in the 0.751.01 eV and 1.7−2.0 eV energy ranges. For the latter range the TOPAS output is doubled via a BBO nonlinear optical crystal. The pump beam is focalized at the sample plane in a 100 μm spot diameter, corresponding to a 2.3 - 10 mJ/cm^2 fluence range. Cross-polarized pump and probe beam in a near normal incidence configuration are used in both the experimental setups.

Two-color time resolved reflectivity experiments As previously reported, the goal of this work is to investigate the processes of charge carrier excitation, dissociation and transport on an ultrafast time scale. In fig.5.4 a comparison between the optical absorption coefficient of the crystalline silicon (gray diamonds. From [126]). and the estimated absorption coefficient of our SWCNT/Glass reference sample is reported (blue line). The Green line are data available in literature [127] for the absorption coefficient of a free-standing carbon nanotube layer. The light blue arrow markers indicate the pump photon energies used in the present experiments.

The optical absorption coefficient for the SWCNT/Glass reference sample is calculated from the optical absorption data (Fig.5.4) assuming a film thickness of

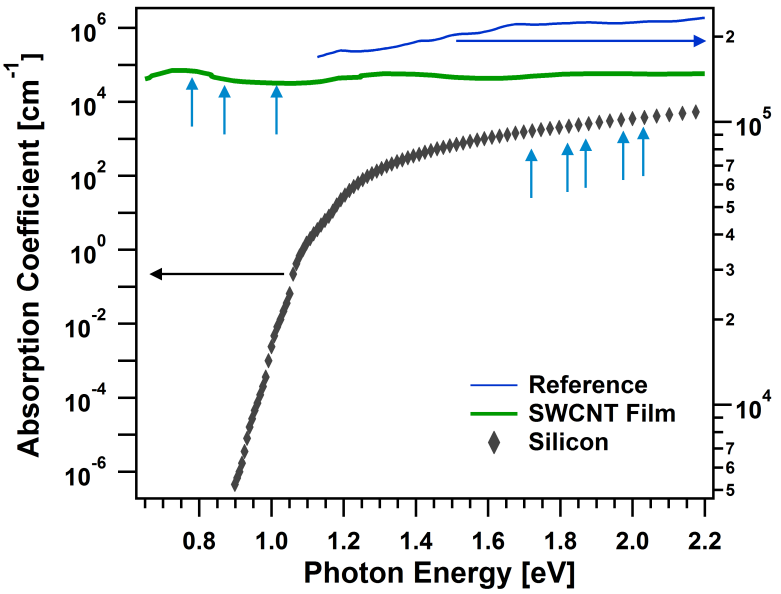

Figure 5.4: Estimated optical absorption coefficient for the metallic enriched SWCNT/Glass reference sample (blue line), for a free standing SWCNT film (Green line, adapted from [127]) and for crystalline Silicon (dark grey diamonds, adapted from [126]). The light blue arrow markers indicate the pump photon energies used in the present experiments.

40 nm. The estimated thickness is based on the values reported in [128] and obtained with angle-resolved XPS measurements performed on similar SWCNT/n-Si cells. The absorption coefficient of crystallize silicon clearly show the onset of the indirect optical interband transitions at 1.12 eV.

The silicon absorption coefficient, below 1.12 eV, strongly depends on the n-doping concentration and increases with it [129]. For a n-silicon sample with a room temperature carriers concentration of 1.4×10^{16} e^-/cm^3 the absorption coefficient in the 0.78-0.87 eV energy interval is found to be in the order of 0.11 cm^{-1} [129]. This value of doping is higher than the one of our sample, which is about 6×10^{14} e/cm^3, therefore a smaller absorption coefficient is expected.

For photon energies below 1.12 eV a negligible amount of charge carriers

can be promoted in the silicon conduction band upon light absorption. On the contrary for the SWCNT layer the optical absorption coefficient is in general higher than the silicon one and, aside for the small modulation due the exciton transitions, do not shows sharp edges in the 0.6-2.2 eV photon energy range. It important to stress that the SWCNT data that cover the full energy interval (green line) are taken from [127] and are collected on a free standing carbon nanotube film and not on our SWCNT/Glass reference sample. The agreement, at least by order of magnitude, between the absorption coefficients of the the two SWCNT layers led us to safely assume that also our reference sample will show a similar behavior also in the $0.6-1.12$ eV energy interval where a direct measurement is unavailable. While SWCNT absorb in all the explored pump energy range, n-Si wafer absorbs mainly in the visible region (from now on labeled as VIS), being the pump excitation energies in the infrared range (from now on labeled as IR) below the onset of the silicon indirect optical transition (1.12 eV). Therefore, it is expected that, in the IR range, where the absorption coefficient of SWCNT is orders of magnitude greater than the silicon ones, a significant carriers population is pumped only in the carbon nanotube leading to a non uniform excitation of the heterojunction. Moreover we also expect that the transient reflectivity signal for pump photon energies in the IR is mainly due to relaxation dynamics of carriers excited in SWCNT layer. Conversely, in the VIS region, carriers are excited both in SWCNT layer and in n-Si wafer. We will exploit the differences in the relaxation dynamics between the IR and the VIS excitation regime to highlight the roles of the SWCNT layer and the silicon substrate in the heterojunction working. We choose to perform TR experiments at the following excitation photon energies: 0.78 eV, 0.87 eV and 1.01 eV for the IR range and at 1.72 eV, 1.82 eV, 1.87 eV, 1.97 eV and 2.03 eV for the IR range. In order to further investigate the effect of the heterojunction on the carriers relaxation dynamics we also perform the same set of TR measurements on the SWCNT/Glass reference sample. In fig.5.5 the TR signals from the SWCNT/Glass reference is reported for a selected set of pump photon energies.

In both the excitation energy ranges the sign of the transient signals for the SWCNT/Glass reference sample is always negative. This in agreement with a photobleaching (PB) process as previously reported in literature for unaligned SWCNTs not arranged in bundles. [6, 7, 130]. In a PB process the absorption of the pump pulse excites electrons in the conduction band, creating holes in

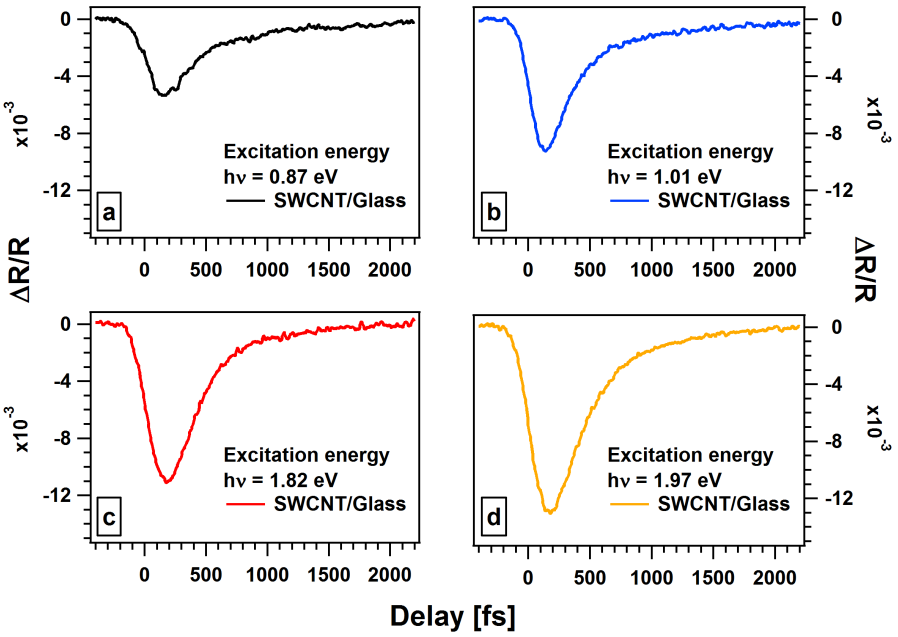

Figure 5.5: Transient optical reflectivity signals collected on the SWCNT/Glass reference sample at 4 different excitation energies. a) pump photon energy $h\nu$=0.87 eV, b) $h\nu$=1.01 eV, c) $h\nu$=1.82 eV, d) $h\nu$=1.97 eV. For all the measurements the pump fluence is kept fixed at 7.7 mJ/cm^2. The probe energy is 1.55 eV.

the valence band. Until these carriers relax, the transient filling of the available final state decrease the absorption of the probe photons because of the Pauli exclusion principle. In case of excitonic transitions the same argument holds and the optical pumping of the exciton transition leads to a reduced oscillator strength for the exciton creation [131]. This effect gives a decrease of the probe absorption inducing a positive transient signal in transmittivity and negative in reflectivity (such as in the absorption). The difference in the TR signal peak magnitude for different excitation energy can be ascribed to the absorption coefficient variation with the pump wavelength, since the pump fluence is kept constant at 7.7 mJ/cm^2 for all the measurements. Aside from the peak

value variation the TR signals show no significant difference in their relaxation dynamics for the different pump energies, as shown in fig.5.6

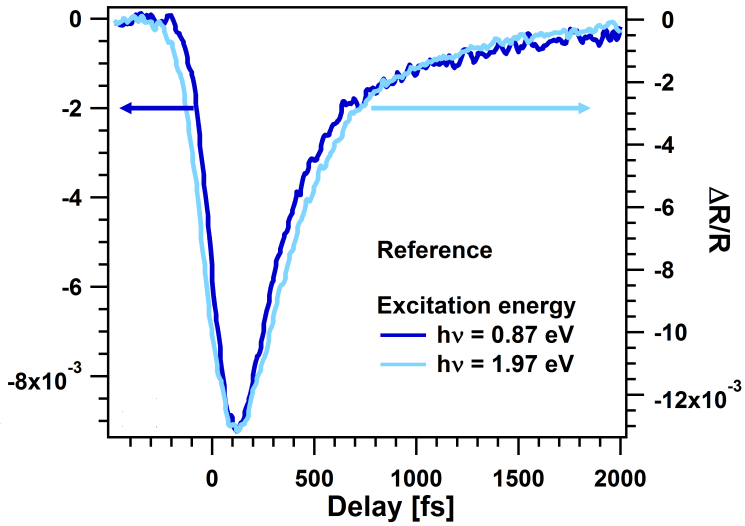

Figure 5.6: Comparison between transient reflectivity signals collected on reference sample at 0.87 eV (dark blue) and 1.97 eV (light blue) pump photon energy. The pump fluence is kept constant at 7.7 mJ/cm^2.

It is worth noting that the laser linewidth is slightly larger (about 30 fs) in the VIS then in the IR region thus justifying the symmetric broadening of the transient response around zero delay time.

In fig5.7 the TR signals from the SWCNT/n-Si is reported for a selected set of pump photon energies.

For excitation energies in the IR range the signal is always negative and with a relaxation dynamics similar to the SWCNT/Glass reference sample. In the VIS range for small and negative delay times a sharp positive transient can be observed. In the assumption that the TR signals is dominated by the sole variation of the complex part of the dielectric function a positive TR signal is usually a fingerprint of a photoabsorption process in which the pump excited electron population is made available for an higher energy optical transition that involves absorption of the probe photons. Since the positive feature is found at

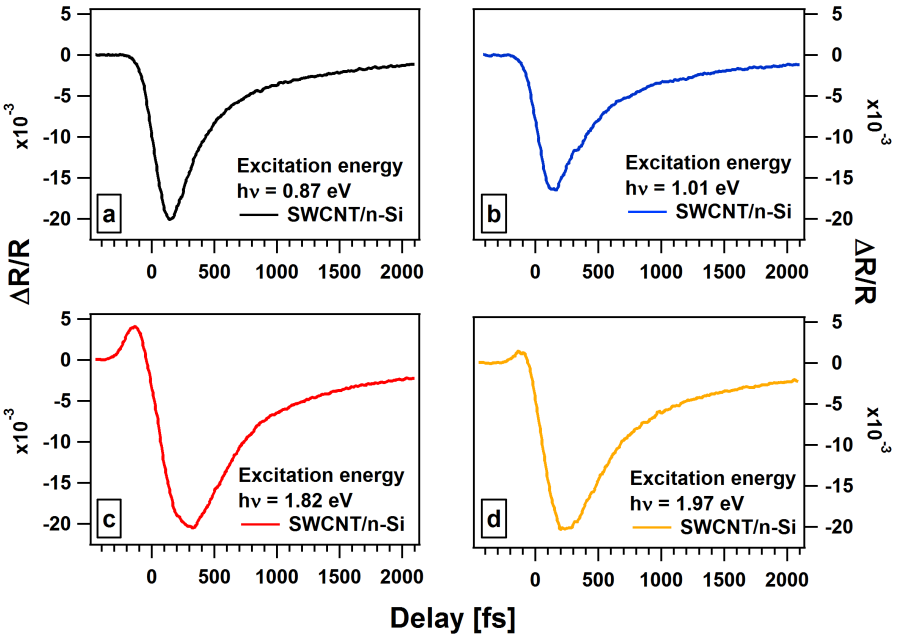

Figure 5.7: Transient optical reflectivity signals collected on the SWCNT/n-Si reference sample at 4 different excitation energies. a) pump photon energy $h\nu$=0.87 eV, b) $h\nu$=1.01 eV, c) $h\nu$=1.82 eV, d) $h\nu$=1.97 eV. For all the measurements the pump fluence is kept fixed at 7.7 mJ/cm^2. The probe energy is 1.55 eV.

negative delay times when the pump and the probe overlap is small and only a fraction of the total pump pulse energy has been absorbed by the sample this effect should be evident for smaller pump fluences. One-color 1.55 eV TR measurements, (Fig.5.14)has been performed with a different laser system in a fifty fold lower pump fluence regime but no appreciable positive feature in the TR data is found. This result seems to exclude a photabsorption process as a possible explanation for the positive transient at higher pump fluence, moreover due to the pump and probe crossed polarization geometry used in our experiments and for the large energy difference between the pump and the probe pulses energy any coherent spike effects [132] could be ruled out as

well. This positive transient is peculiar of the SWCNT/n-Si samples but since is nature need further work to be clarified we restrict our considerations only at large and positive pump-probe delays where pure nonlinear effects can be neglected due to the small dephasing times typical of solid state systems at room temperature. While with an IR pump photon energy the relaxation dynamics of the photobleaching component for SWCNT/n-Si are similar to those observed on the reference sample for both IR and VIS regime, the transient signal collected in the VIS range shows an enhancement of the relaxation dynamics. In fig5.8 an exemplificative comparison between the TR signals collected at 0.87 eV (red line) and 1.97 eV (orange line) is reported.

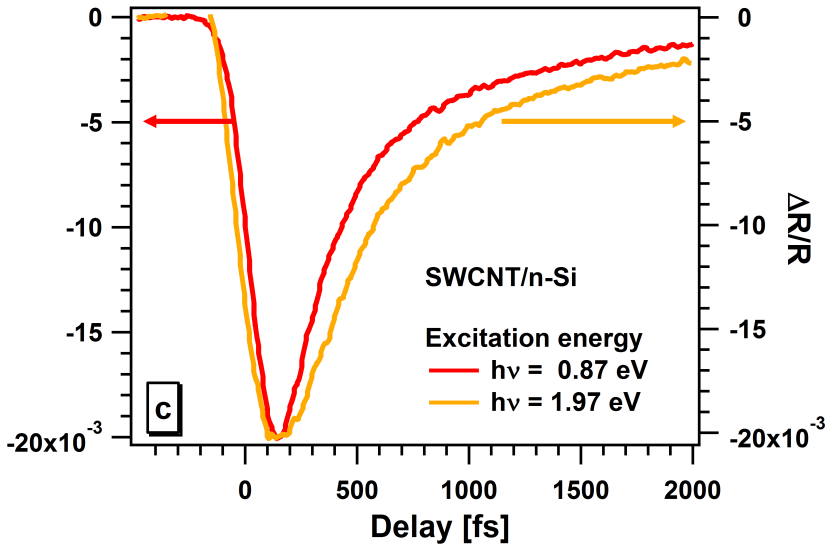

Figure 5.8: Transient reflectivity signal on SWCNT/Si-n junction at 0.87 eV (red lines) and 1.97 eV (orange lines) pump photon energy. The pump fluence is kept constant at 7.7 mJ/cm^2

It is known from literature that the transient response of crystalline Si excited above its absorption threshold [133] exhibits a negative variation with a multi-picosecond decay dynamics mainly due to the slow recombination of the photoexcited electrons and holes lying at the bands edges. Therefore, in order

to exclude that the slower relaxation dynamics found in transient signals collected in the visible region (Fig.5.8) is merely due to the superposition of the signals from the nanotubes (fast dynamic) and from the underlying substrate (slow dynamic) we have performed transient measurements on the bare n-Si substrate. As shown in Fig.5.9 (grey curve), in similar experimental conditions the response of n-Si has a step-like behavior, but from experiments performed in the two-color configuration, we checked that its ΔR/R signal is lower than our experimental resolution ($\Delta R/R \sim 10^{-4}$). This result ensures that, for all the measurements performed in the VIS range, the transient response comes from the relaxation dynamics of the carriers in SWCNT layer.

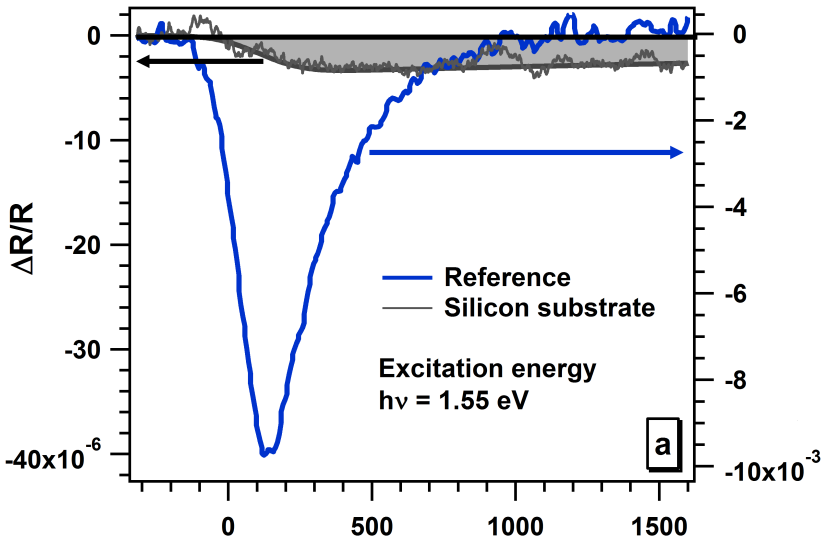

Figure 5.9: One color transient reflectivity signals collected on the reference sample (SWCNT/Glass, blue line) and on Si substrate (gray line), using a photon energy of 1.55 eV. Note the difference in the $\Delta R/R$ signal magnitude. For the one-color measurement on the n-Si crystal the low fluence setup is employed and the pump fluence is in the order of 1 mJ/cm^2.

Therefore, the enhancement of the relaxation dynamics observed in the VIS regime has to be ascribed to the response of SWCNT in contact with n-Si and it is observed when the pump photon energy is able to excite carriers in

SWCNT as well as in n-Si substrate. In order to get insights in the role of the SWCNT/n-Si junction in the relaxation dynamics, we compare the signals from the SWCNT/n-Si heterojunction to those collected on the reference sample for all the used excitation energies. The pump fluence is kept constant at 7.7 mJ/cm^2. The normalized value of ΔR/R on SWCNT/n-Si junction, together with the one from the SWCNT/glass reference is displayed in Fig.5.10. All signals are normalized to the ΔR/R maximum and in a logarithmic scale for highlighting the differences at longer delay times. In the IR range, for an excitation energy of 0.78 eV (Fig.5.10a) the junction TR signal redraws the signal of the reference sample. At 0.87 and 1.01 eV pump photon energies (Fig.5.10b and Fig.5.10c) the SWCNT/n-Si TR signal starts to manifest a longer relaxation dynamics deviating from the SWCNT/Glass one. This difference becomes much more evident for the pump excitation above the Si bandgap energy value as shown in Fig.5.10d, Fig.5.10e and Fig.5.10f collected at a pump photon energy of 1.72 eV, 1.82 eV and 1.97 eV, respectively.

This behavior unambiguously suggests that when the density of the charge carriers excited in the Si substrate is no more negligible, the transient response of SWCNT/n-Si junction deviates from the response of the reference sample. In order to quantify the difference observed in the relaxation dynamics, the transient signals of both samples are interpolated with a two-exponential decay fitting function of the form:

$$\frac{\Delta R}{R} = A_1 e^{-\frac{t-t_0}{\tau_1}} + A_2 e^{-\frac{t-t_0}{\tau_2}} \tag{5.1}$$

where A_1 and A_2 are the amplitude for the fast and the slow relaxation components of the photobleaching dynamics, characterized by a relaxation time constant τ_1 and τ_2 respectively. t_0 is fixed at 100 fs after the the peak of the TR photobleaching signal in order to minimize the effect of the pump pulse (whose time croscorrelation FWHM is in the order of 200 fs) on the signal relaxation shape. This fitting procedure is chosen in order to exclude the fast positive transient (Fig.5.7) from the data analysis. Even if this fitting function is only approximate and does not explicitly account for the pump and probe convolution effects on the relaxation dynamics, the simple double exponential form of the relaxation dynamics allows to analytically calculate the correction for the extracted time constants at least for the slower relaxation component. For simplicity we report in fig.5.11 the calculated time constant as given by the

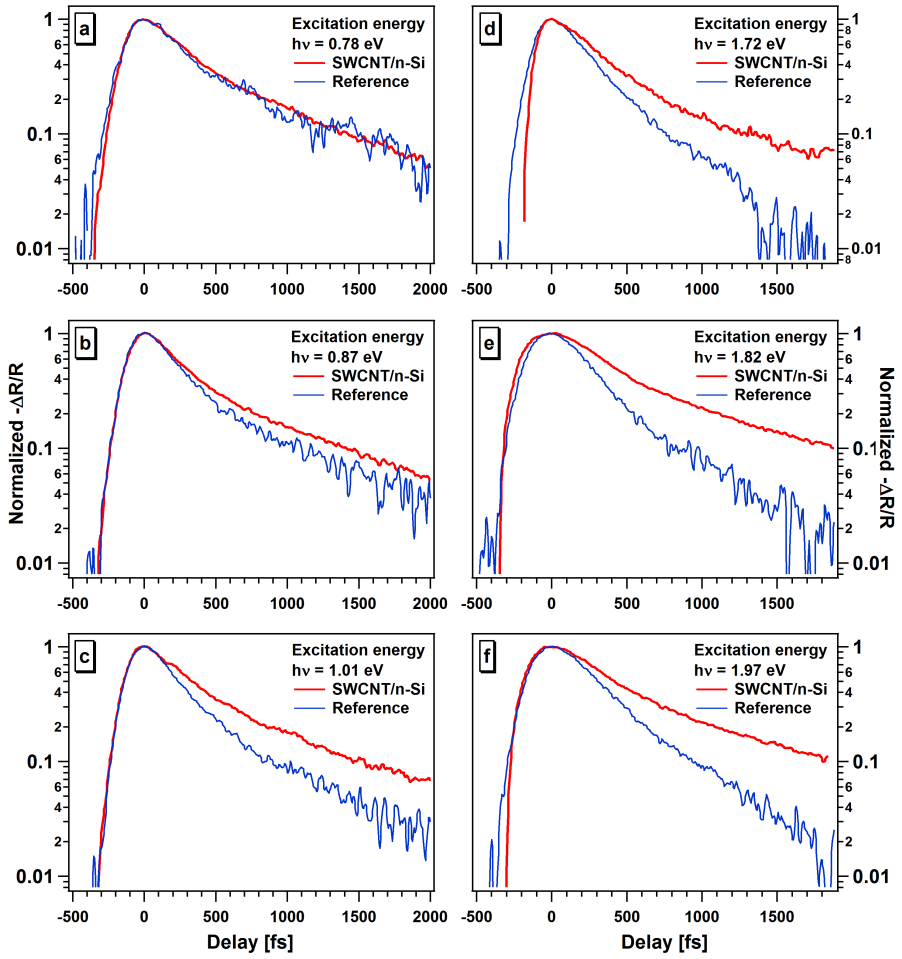

Figure 5.10: Comparison between selected TR signals from the SWCNT/Glass reference sample (blue line) and from the SWCNT/n-Si junction (red line) in logarithmic scale. All TR signals are peak-value normalized and reversed in sign. Pump photon energies are (a) 0.78 eV, (b) 0.87 eV, (c) 1.01 eV, (d) 1.72 eV, (e) 1.82 eV, (f) 1.97 eV respectively. For all the collected signals the pump fluence is kept fixed at 7.7 mJ/cm^2

fitting function without any analytical corrections.

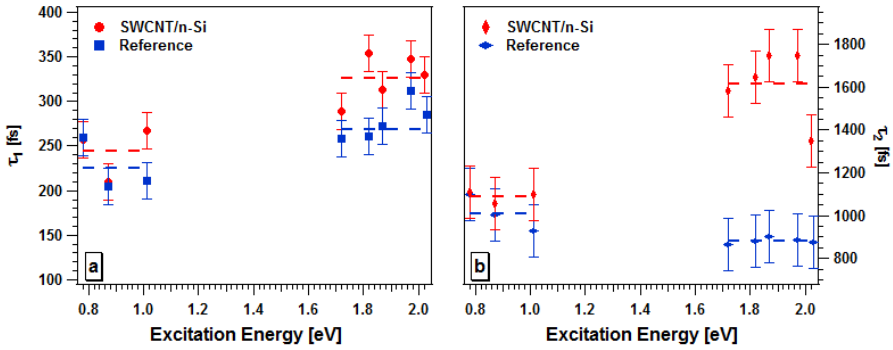

Figure 5.11: Comparison between the fast (a) and slow (b) relaxation time constants of the SWCNT/Glass reference sample (blue squares) and SWCNT/n-Si junction (red circles) upon the variation of pump photon energy as given by a bi-exponential interpolation of the TR signals. Error bars are estimated on a statistical basis by the fitting software

Considering the statistical error, wich is directly calculated by the fitting software on a statistical basis, in the IR region both the fast (about 225 fs) and the slow (about 1000 fs) decay of the SWCNT/n-Si junction are comparable with those of SWCNT/Glass reference sample. Conversely, in the visible region where carriers are excited also in n-Si wafer, while the fast decay of the two samples can be considered still comparable (about 300 fs), the slow relaxation time of the SWCNT/n-Si junction is about twice than the reference sample. The value of the fast decay time is in agreement with the data available in literature [41,46] on similar systems and is ascribed to the rapid thermalization, via electron-electron scattering, of the laser-excited carrier population in carbon nanotubes. The hot electron population thermalizes then with the lattice via phonon emission processes giving rise to the slow component of the relaxation dynamics. The value of this slow decay reported in literature on metallic enriched SWCNT films [41] is about 1 ps in accordance with the value measured on SWCNT on glass. In Fig.5.12a and Fig.5.12b a comparison among the amplitude values , A_1 and A_2 obtained by the same fitting procedure is reported.

For both samples, the amplitude of the fast relaxation dynamics increases

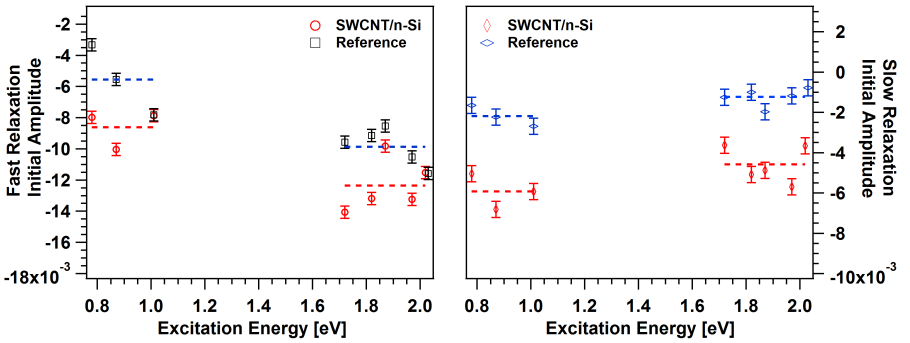

Figure 5.12: Comparison between the SWCNT/Glass (blue squares) and SWCNT/n-Si (red circles) fast (c) and slow (d) relaxation dynamics initial values. Both the numerical values and the error bars magnitude are extracted by the interpolation of the bare TR signals with a double exponential decay fitting function.

from the IR to the visible energy range. As observed earlier in ths section this variation could be ascribed to the increasing of the absorption coefficient of the SWCNT as the excitation photon energy get closer to the resonance with the optical transitions in the metallic tubes, which, for tubes with this diameter distribution, are localized among 1.7 and 2 eV (Fig.5.3 and 5.4). Moreover, the mean value of the signal amplitudes is lower in the reference sample than in SWCNT/n-Si. This happens for all the explored pump photon energies suggesting that this difference is almost certainly due to a different density of SWCNT in the area investigated by the laser beams or to the sightly different thickness of the SWCNT films for the two samples. From this analysis of the data, we can argue that the different optical response observed in the VIS region between the SWCNT/n-Si junction and the reference sample has to be mainly ascribed to an increase of the slow relaxation dynamics and that the origin of the slow dynamics enhancement observed for SWCNT/n-Si heterojunction in the VIS region has to be found in the presence of the carriers excited in the n-Si wafer.

In the SWCNT/n-Si junction formation, the balance of the chemical potentials requires a net transfer of electrons from the n-Si towards the metallic tubes via ionization of the silicon donor impurities in a region close to the junction region. This process leads to the creation of a Schottky barrier in which the

depleted region extends almost entirely into the semiconductor for a depth of a few microns. [14] In the metallic tubes the excess electrons form a charge layer that can induce a significant band bending in the semiconductor substrate and the subsequent formation of a potential barrier that gives to the junction its characteristic current-rectifying and light-to-electric current conversion properties. In this simple scheme is possible to construct a diagram from the energy levels at the heterojunction interface starting from the workfunction of the carbon nanotubes (W_{CNT}), the Silicon electron affinity (χ_{Si}), its bandgap and its n-doping level, which determines the position of the chemical potential inside the bandgap. The energy level scheme constructed taking $W_{CNT} = 4.8$ eV is reported in fig.5.13. For the Silicon crystal the values of χ_{Si} and the bandgap energy are taken from literature whilst the position of the chemical potential is inferred from the n-silicon parameters and from the interpolation of the I-V curves of the heterojunction cell (measurements not reported here).

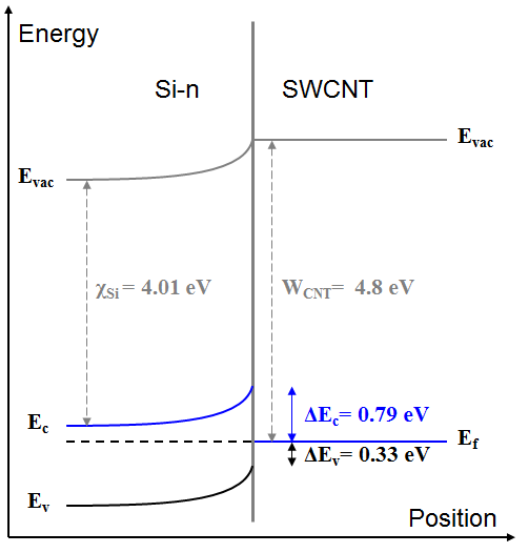

Figure 5.13: Band diagram at the SWCNT/n-Si heterojunction interface

The large built-in potential ($\approxeq 0.5$ eV) permits the charge separation. Recently, a thin SiO_2 SiO_x layer has been found between the SWCNT and the n-Si

substrate using angle-resolved XPS measurements. [128] The oxide layer, whose thickness is between 1 and 2 nm, slightly alters the band alignment at the junction interface (Fig.5.13). Whilst it has been reported that a particular thickness of the oxide layer can lead to an increased power conversion efficiency [128,134], for sake of simplicity, neglecting it, we model SWCNT/n-Si interface as a simple Schottky junction. The electron-hole pairs generated in the n-Si depleted region upon absorption of the pump photons are quickly separated by the built-in field, $E = -\nabla\phi(x)$. Whilst the electrons are swept away from the junction by the built-in field, the holes are forced towards the metallic SWCNT layer where they can easily cross the junction and become trapped in.

This simple picture suggest the possibility that the increased relaxation time observed in the VIS range (Fig.5.10) can be primarily due to a net flux of photoexcited holes that, under the effect of the built-in field in the device, drift from the n-Si depleted region into the valence band of the SWCNT layer.

Since the magnitude of the light absorption coefficient depends on the difference between the density of initial and final states available for the optical transitions weighted by their occupation number [14, 106] injected holes, could lead to a transient bleaching in the SWCNT transient signals. The slow relaxation time of the excited carriers in the n-Si substrate together with the low mobility of the holes in doped crystalline silicon [135] make the hole injection, at the junction interface, acting as a slow source for the photobleaching signal, accounting for the enhancement of the slow relaxation dynamics in SWCNT/n-Si heterojunction. When the pump photon energy is below the absorption edge of the n-Si substrate, such as in the IR range measurements, only a small amount of electron-holes pairs are excited in the silicon giving rise to a negligible hole flux and the measured transient signals from the SWCNT layer resembles those collected on the SWCNT/Glass reference sample. Conversely, in the VIS regime, due to the similar absorption coefficient value of SWCNT and n-Si wafer a high density of carriers is excited by the pump pulse in both materials. The fast electron-electron relaxation process rapidly thermalizes the carrier population in the SWCNT layer without being significantly influenced by the silicon substrate. On longer time scale the hole drift current from the substrate starts to alter the carrier relaxation in the SWCNT film leading to the observed increase of the slow relaxation time constant. The thickness d of the depletion layer has been estimated by using the following equation (5.2)

$$d = \left(\frac{2\epsilon_e \epsilon_0 \phi}{ne} \right)^{\frac{1}{2}} \tag{5.2}$$

where ϕ is the build-in potential, n is the density of the Si doping (wich in our case is $n \sim 6 \times 10^{14}$ e$^-$/cm^3) , ϵ_r and ϵ_0 are the silicon and the vacuum dielectric constants and e the elementary charge. The depletion layer thickness results about 1 μm. Equation (5.2) is valid for ideal metal-semiconductor junction and for a constant density of ionized impurities across the depleted region. For these reasons the calculated d value must be considered only as a crude estimation since the actual structure of the heterojunction, on a micrometric scale, is more similar to disordered network of parallel connected nano-junctions formed by each tube in contact with the n-silicon substrate. From this value, considering the built-in potential of $\phi \cong 0.5$ V and the value of the hole mobility for the n-Silicon $\mu_h \sim 264$ cm^2/V [135] is possible to estimate the time scale of the hole drift time from the edge of the depleted region towards the SWCNT layer. The time scale turns out to be in the order of 75 ps. Obviously this transit time represent only an upper limit to the process time scale.

In order to estimate the value of electron-hole pairs density excited in the depletion layer, we have calculated, starting from the laser pump fluence, the photon numbers that, after crossing the SWCNT layer arrive in the Si depletion region. For this estimation we make use of the average transmittivity T_{CNT} measured on the SWCNT/Glass reference sample which is in the order of 40% (Fig.5.3) in the VIS energy range. Due to the different thickness of the two SWCNT layers, the resulting value is slightly overestimated. The average density of the photoexcited pairs n_{EXC} is then given by the relation:

$$n_{EXC} = \frac{F_s - F_s e^{-\alpha d}}{h\nu d} \tag{5.3}$$

where $F_s = F \cdot T_{CNT}$,$T = 40\%$, α is the silicon absorption length at the pump wavelength and F is the pump fluence. For a pump fluence of 7.7 mJ/cm^2, and at a pump photon energy of 2 eV, the average density of the pairs excited in the n-Si depletion layer (calculated by assuming that 1 photon generates 1 e-h pair) is 3.4×10^{19} pairs/cm^3. This photoexcited carrier density greatly exceed the carrier concentration due to the n-doping. In such an high excitation condition the simple band diagram shown in fig.5.13 no longer holds and a com-

plex interplay between the drift and the diffusion terms at the heterojunction interface can arise. In order to check the stability of our results we perform a set of TR experiments on the 5.5 ml cell with o one-color, 1.55 eV low fluence setup. The details about this setup are reported in the laser system paragraph. A typical TR signal from the 5.5 ml solar cell collected at 1.55 eV and for a pump fluence of 0.15 mJ/cm^2 is reported in fig.5.14a. This fluence is more than 50 times smaller than the one used for the two-color TR experiment.

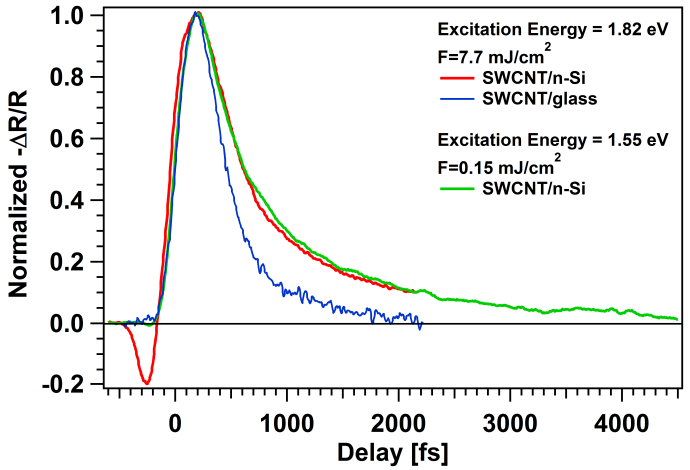

Figure 5.14: Comparison between the TR signals from the SWCNT/n-Si at two different fluences (and excitation energies). The SWCNT/glass TR signal is also reported (blue line)

Also in this case the TR signal is compatible with a photobleaching process and exhibit a two exponential relaxation dynamics. In fig.5.14b a direct comparison with the TR signal collected at 1.82 eV and for a pump fluence of 7.7 mJ/cm^2 (black line) is shown. Both signals are normalized at their photobleaching signal maximum and reversed in sign. The similarity between the two TR signals is evident and the fitting procedure gives similar values of the relaxation time constants for both the the fluences regimes. It is noteworthy that by decreasing the pump laser fluence down to a value nearly 50 times more weak the relaxation times of the transient response in the VIS range remains

unchanged. For a pump fluence of 0.15 mJ/cm^2 the average density of photoexcited carriers in the n-Silicon layer, estimated with the eq.(5.3) is 2.3×10^{17} pairs/cm^3. Since this value still greatly exceed the carriers concentration due to the n-doping we measure the external quantum efficiency of the cell under fs-pulsed light illumination in order to check for its proper operation. The EQE values are reported in fig.5.15.

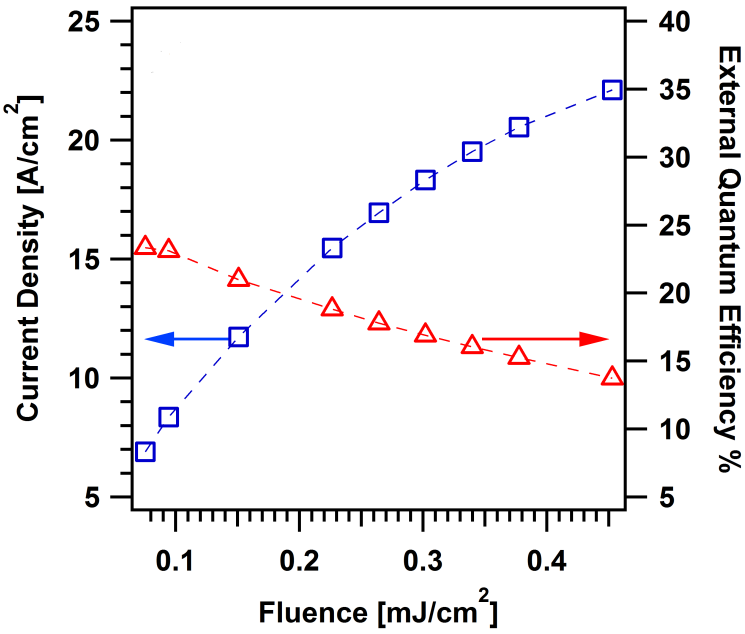

Figure 5.15: EQE values (red triangles) and the corespondent current density (blue squares) measured on the SWCNT/n-Si under femtosecond pulsed illumination.

The EQE measurements are performed shunting the solar cell on a current amplifier acquired with a lock-in technique similar to the one used for the continuous-wave EQE measurements. The light source is the same laser oscillator used for the low fluence TR measurements. The EQE is calculated by taking the ratio between the average photon number of the laser beam and the average current from the cell, whilst the average current density in the device can be

calculated considering the laser spot size (radius = 25 μm). The static EQE for the 5.5 ml cell (Fig.5.15) at 1.55 eV is 32.5% whilst for pulsed illumination varies between 20.5 % at 0.15 mJ/cm^2 and 15 % at 0.47 mJ/cm^2. Even for this relatively high level of photoexcitation the EQE is reduced only at about the 50% of its static value whilst the expected carrier density in the silicon layer exceed of about one hundred times the n-doping density. This results, combined with the overall constancy of the relaxation time constant in a wide fluence range, support our hypothesis on the role of the drift current in the slower relaxation dynamics. Using the EQE value (20.5%) at 0.15 mJ/cm^2 (Fig.5.15), to estimate the pair density density contributing to the photocurrent the results turns out to be 1.2×10^{18} pairs/cm^3 per pulse, that is about 5 times higher with respect to the average pair density excited in the n-Si depletion layer taking the SWCNT layer transmission into account (using formula (5.3)). This somewhat surprising result suggests that a contribution at the photocurrent seems also to come from the carriers excited in the carbon nanotubes that, in the working solar cell, may behave as photogeneration sites, in agreement with the results reported in [31]. In order to fully clarify this behavior a continuous-wave EQE measurement, combined with a careful determination of the carbon nanotube layer transmission coefficient, is more suitable than our experimental setup, so further investigation is needed. One of the key factor witch determines the *internal* quantum efficiency of a photocell is the ability to generate and separate the photoexcited charge carriers. An increased internal quantum efficiency can reflect on an increased external external quantum efficiency of the device. Leaded by this consideration we have performed a set of TR experiments on the 1.5 ml heterojunction, which is characterized by a lower power conversion efficiency but with an higher EQE. A comparison between the TR signals from the 1.5 ml (green line) and the 5.5 ml (red line) cell is reported in fig.5.16

Both signal are collected at 1.55 eV and with a pump fluence of 0.45 mJ/cm^2. The more efficient cell (static EQE at 795nm (1.55 eV) =60%) shows an enhancement of the second dynamics, whose relaxation time is about twice (3700$\pm$100 fs) the value (1640$\pm$100 fs) obtained on the less efficient cell (static EQE at 1.55 eV =30%). In accordance with our picture, a greater external quantum efficiency means a larger number of electron-hole pairs excited and efficiently separated in the depletion layer and then a larger hole injection rate in the SWCNT layer, that we reveal through an enhancement of the second slow dy-

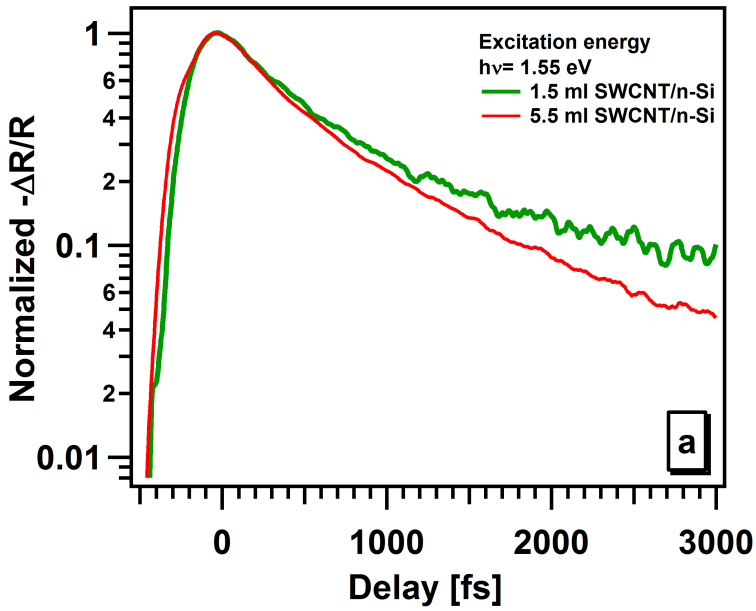

Figure 5.16: Comparison between the 1.5 ml SWCNT/n-Si (green line) and 5.5 ml SWCNT/n-Si (red line) TR signals. The relaxation dynamics for the higher EQE cell is slower.

namics in the SWCNT transient response. As for the 5.5 ml cell, the relaxation time constant of the TR signal collected on the 1.5 ml cell do not present a significant variation over the entire low fluence range (0.15−0.47 mJ/cm^2).

5.4 Conclusions

The goal of the present work was to clarify the role of SWCNT in hybrid SWCNT/n-Si heterojunctions, by investigating the relaxation dynamics of the photoexcited carriers at the interface. The relaxation dynamics of the TR signals from the photocells was compared with the dynamics of SWCNT/glass reference sample, where no heterojunction effects are present. As the laser pump fluence was selected to hinder a transient optical response from the bulk

silicon, our spectroscopy set-up was properly tuned to excite prevalently the SWCNT layer or both sides of the heterojunction. The results showed that for excitations below the Si optical absorption threshold, both samples display the same behavior, and therefore the response is determined by the SWCNT layer alone. In turn, for energies above the Si absorption threshold, the SWCNT/n-Si junction displays a slower relaxation dynamics, along with an enhancement of the photobleaching effect. This was recognized as an intrinsic behavior of the junction, not found on the SWCNT/Glass interface, and was rationalized as a charge transfer of holes from n-Si to SWCNT across the junction, depleting the occupied levels of the SWCNT. This interface charge transfer dynamics was shown to develop on a multi picosecond time scale, possibly driven by the hole drift current at the heterojunction interface. These results here reported show that transient optical spectroscopy is a suitable tool for investigating the processes occurring immediately after the photogeneration of electron-hole pairs in a CNT/n-Si solar cells and, by extension, in a wider class of heterojunction devices presenting similar optical characteristic. The analysis of the TR signals combined with a quantitative theoretical model of the heterojunction can, in principle, provide information on the heterojuncion parameters and clarify the role of the heterostructure components on the carrier generation, dissociation and transport.

Chapter 6

Conclusions

In the first part of this thesis the carriers relaxation dynamics in carbon nanotubes aggregates with potential application in solar cells devices is investigated by means of ultrafast time resolved optical spectroscopy. Three different kind of CNT aggregates are considered: Aligned multi-walled carbon nanotubes, vertically aligned single-walled carbon nanotubes bundles and free standing films of ultrapure metallic and semiconducting enriched single-walled carbon nanotubes. From one-color transient transmittivity measurements the complex behavior of the carriers dynamics in aligned multi walled carbon nanotubes is revealed. The optical response is characterized by photo-bleaching and photo-absorption channels with a remarkable dependance on the probe polarization with respect to the tubes axis. Our results indicate that the MWCNT electronic structure is different from the highly oriented pyrolytic graphite one, and suggest the existence of discrete levels with a well-defined symmetry in the electronic structure of MWCNT. One-color transient reflectivity experiments are performed on aligned SWCNT bundles in order to clarify the effect of structural defects on the carriers relaxation dynamics and on the transient optical properties of bundled SWCNT. In one of our previous work [7], using a broadband probe, a dramatic dependance of the transient reflectivity on the bundles alignment was detected. Whilst aligned bundles shows only a fast transient photobleaching of their optical transitions, unaligned bundles present a broadband transient enhancement of their reflectivity which extends in a broad energy region above

and below the exciting laser pulse center energy (at 1.55 eV). This behavior was rationalized in terms of an enhanced conductivity of the sample induced by the unalignment of the SWCNT bundles. This result is of particular interest for the design of CNT based optoelectronic devices since seems to point toward growth architecture dependent effects on the bundled SWCNT optical and electronic properties. The results reported in this thesis exclude that the conductivity enhancement can be simply ascribed to the presence of structural defects in the SWCNT bundles and confirm the bundles unalignment as the more probable cause of the transient reflectivity enhancement. However the defect content influence the carriers relaxation characteristic times leading to the suppression of a slower relaxation dynamics, which take place on a picosecond time scale, and that is present in the sample with a lower defect content. The presence of this slower decay dynamics may be the fingerprint of strong exciton interaction effects (exciton-exciton annihilation) and therefore reveal the stability of the excitons even in the CNT bundles. In the study of the properties of carbon nanotubes aggregates, such the the former SWCNT bundles, the samples are usually a mixture of various SWCNT with different chiralities and with metallic and semiconducting character. For this reason the carriers relaxation dynamics in metallic carbon nanotubes is not commonly investigated despite their potential application as charge collector and transparent conductive films in optoelectronic devices. In order to overcome this limitation we study the transient optical properties of metallic enriched ultrapure SWCNT free-standing films. From a direct comparison with an ultrapure semiconducting enriched free-standing film we are able to highlight a 6.7 ps photoabsorption dynamics, which is present only in the metallic enriched sample and that is detected even for non-resonant pumping of the main exciton absorption line. From the analysis of the pump power and excitation photon energy dependence of the transient signal we are able to exclude a pure thermal effect as the responsible physical mechanism. Following the consideration reported in [103] we ascribe the slow photoabsorption transient to optical transitions involving an hot Dirac fermion population excited in the vicinity of the Fermi level and which can be promoted toward higher lying electronic states upon absorption of probe photons with an appropriate energy. Moreover, if this assignation is confirmed, our results seem to indicate that a carriers multiplication process can take place in the metallic tubes. Aside from the theoretical interest this

result can have a great relevance for photovoltaic application since in an opportunely designed device carriers multiplication reduces the energy losses due to phonons interactions and could potentially increase both the quantum efficiency and the effective power conversion efficiency of the system. The aforementioned studies deals mainly on the intrinsic carriers dynamics in SWCNT aggregates and must be regarded as a starting point in the study of more complex systems such as CNT based heterojunction solar cells. In the last part of this thesis the process of carriers separation and transport in a n-Si/SWCNT hybrid solar cell is investigated with two-color time resolved reflectivity experiments. The hole injection in the carbon nanotube layer of the junction manifests as an increased relaxation time for the transient photobleaching signal. The charge transfer, possibly mediated by an hole drift current from the n-Silicon depleted region, takes place on a few picosecond time scale and its relaxation time constant increases with the external quantum efficiency of the solar cells. The increased relaxation time is detected only for excitation energies above the onset of the Silicon indirect interband transition pointing toward a rather passive role of the SWCNT as light harvesting element. However external quantum efficiency measurements performed under femtosecond pulsed illumination indicates that an electron transfer from SWCNT toward the n-Si substrate may take place. In future transient reflectivity experiments using a broadband probe pulse will be performed in order to follow the population dynamics in a wider energy range and possibly follow the charge transfer process in both ways across the heterojunction. The analysis of the transient reflectivity signals combined with a quantitative theoretical model of the heterojunction will provide information on the heterojuncion parameters, clarify the physical processes involved in the carriers generation, dissociation and transport phenomena and the role of the heterostructure components.

Acknowledgments

Here I would like to thanks all the people involved in the research activities that I performed in these three years

A special thanks goes, of course, to my Supervisor Dr. Stefania Pagliara who made this research possible.

Thanks to Dr. Stephan Hofmann (Cambridge University, Department of Engineering) who provided us of the aligned multi walled carbon nanotubes samples.

Thanks to Dr. Cinzia Cepek (CNR - Istituto Officina dei Materiali - Laboratorio TASC) who provided us of the aligned single wall carbon nanotubes samples.

Thanks to Prof. Katalin Kamarás (Wigner Research Centre for Physics, Hungarian Academy of Sciences) who provides us the ultrapure free standing single wall carbon nanotubes films.

Thanks to Prof. Paola Castrucci (University of Rome Tor Vergata, Physics Department) who provides us of the n-Si/SWCNT heterojunction solar cells and of the related SWCNT samples.

Un ringraziamento speciale va anche al Dr. Gianluca Galimberti per l'aiuto e il supporto che mi ha offerto in questi anni. Desidero ringraziare tutti gli amici che lavorano nei laboratori del Dipatimento di Matematica e Fisica dell' Universitá Cattolica di Brescia, in particolare Chiara, Federica, Silvia, Giovanni,

Emanuele e Gabriele. Anche grazie a voi questi tre anni sono stati un' esperienza meravigliosa.

Bibliography

[1] Ijima S. Helical microtubules of graphitic carbon. *Nature*, 354:56–58, 1991.

[2] F. Wang, D. J. Cho, B. Kessler, J. Deslippe, P. J. Schuck, S. G. Louie, A. Zettl, T. F. Heinz, and Y. Ron Shen. Observation of excitons in one-dimensional metallic single-walled carbon nanotubes. *Phys. Rev. Lett.*, 99:227401–4, 2007.

[3] M. S. Arnold, J. L. Blackburn, J. J. Crochet, S. K. Doorn, J. G. Duque, A. Mohite, and H. Telg. Recent developments in the photophysics of single-walled carbon nanotubes for their use as active and passive material elements in thin film photovoltaics. *Phys. Chem. Chem. Phys.*, 15:14896–14918, 2013.

[4] X. Wang, L. Zhi, and K. Mllen. Transparent, conductive graphene electrodes for dye-sensitized solar cells. *Nano Lett.*, 8:323–327, 2008.

[5] Eda B.G., Lin Y.Y., Mattevi C., Yamaguchi H., Chen H.A., Chen I.S., and et al. Probing the electronic structure of multi-walled carbon nanotubes by transient optical transmittivity. *Carbon*, 57:50–58, 2013.

[6] G. Galimberti, Stefano Ponzoni, G. Ferrini, S. Hofmann, M. Arshad, C. Cepek, and S. Pagliara. Transient reflectivity on vertically aligned single-wall carbon nanotubes. *Thin Solid Films*, 543(0):51 – 55, 2013.

[7] Galimberti G., Pagliara S., Ponzoni S., Dal Conte S., Cilento F., Ferrini G., and et al. The photoinduced charge transfer mechanism in aligned and unaligned carbon nanotubes. *Carbon*, 49:5246–52, 2011.

[8] Zhao X., Liu Y., Inoue S., Suzuki T., Jones R. O., and Ando Y. Smallest carbon nanotube is 3 angstrom in diameter. *Phys. Rev. Lett.*, 92:125502–3, Mar 2004.

[9] M.S. Dresselhaus, G. Dresselhaus, and Ph. Avouris. *Carbon Nanotubes. Synthesis, Structure, Properties, and Applications.* Springer, 2001.

[10] Reich S., Thomsen C., and Maultzsch J. *Carbon Nanotubes.* Wiley, 2004.

[11] A. Thess, R. Lee, P. Nikolaev, H. Dai, P. Petit, J. Robert, C. Xu, Y. Hee Lee, S. Gon Kim, A. G. Rinzler, and D. T. Colbert et al. Crystalline ropes of metallic carbon nanotubes. *Science*, 273:483–487, 1996.

[12] X. Liu, T. Pichler1, M. Knupfer, M. S. Golden, J. Fink, H. Kataura, and Y. Achiba. Detailed analysis of the mean diameter and diameter distribution of single-wall carbon nanotubes from their optical response. *Phys Rev B*, 66:045411, 2002.

[13] F. Wooten. *OPTICAL PROPERTIES OF SOLIDS.* Academic Press, 1972.

[14] G. Grosso and G. Pastori-Parravicini. *Solid state physics.* Academic Press, 2000.

[15] A. Zarifi and T. G. Pedersen. Universal analytic expression of electric-dipole matrix elements for carbon nanotubes. *Phys. Rev. B*, 80:195422–7, 2009.

[16] H. Ajiki and T. Ando. Carbon nanotubes: Optical absorption in aharonov-bohm flux. *Jpn. J. Appl. Phys.*, 34-1:107, 1994.

[17] L. X. Benedict, S. G. Louie, and M. L. Choen. Static polarizabilities of single-wall carbon nanotubes. *Phys. Rev. B*, 52:8541, 1995.

[18] F. Wang, G. Dukovic, L. E. Brus, and T. F Heinz. The optical resonances in carbon nanotubes arise from excitons. *Science*, 308:838–41, 2005.

[19] A. D. Mohite, P. Gopinath, H. M. Shah, and B. W. Alphenaar. Exciton dissociation and stark effect in the carbon nanotube photocurrent spectrum. *Nano Lett.*, 8:142–146, 2008.

[20] Castrucci P., Tombolini F., Scarselli M., Speiser E., Del Gobbo S., Richter W., and et al. Large photocurrent generation in multiwall carbon nanotubes. *Appl. Phys. Lett.*, 89:253107–9, 2006.

[21] Lin M.F. Optical spectra of single-wall carbon nanotube bundles. *Phys. Rev. B*, 62:13153–9, 2000.

[22] V. Zolyomi, J. Koltai, A. Rusznyak, J. Kurti, A. Gali, H. Kuzmany F. Simon, A. Szabados, and P. Surjan. Intershell interaction in double walled carbon nanotubes: Charge transfer and orbital mixing. *Phys. Rev. B*, 77:245403, 2008.

[23] V. Zolyomi, J. Koltai, A. Rusznyak, J. Kurti, A. Gali, H. Kuzmany F. Simon, A. Szabados, and P. Surjan. M. e. brennan and j. n. coleman and a. drury and b. lahr and t. kobayashi and w. j. blau. *Optics Letters*, 28:266–4, 2003.

[24] A. Pratap, L. Shah, R. Singh, S. Pal, R. K. Tyagi, L. Dawar, P. Chaturvedi, S. Lamba, and M. Bal. Linear and non-linear optical transmission from multi-walled carbon nanotubes. *Journal of Materials Science*, 40:4185–4188, 2005.

[25] S. Barazzouk, S. Hotchandani, K. Vinodgopal, and P. V. Kamat. Single wall carbon nanotube films for photocurrent generation. a prompt response to visible light irradiation. *J. Phys. Chem. B*, 108:17015–17018, 2004.

[26] S. Hong and S. Myung. Nanotube electronics: A flexible approach to mobility. *Nature Nanotech.*, 2:207–208, 2007.

[27] L. Javey, H. Kim, M. Brink, Q. Wang, A. Ural1, J. Guo, P. McIntyre, P. McEuen, M. Lundstrom, and H. Dai1. High k dielectrics for advanced carbon-nanotube transistors and logic gates. *Nature Materials.*, 1:241–246, 2002.

[28] Z. Wu, Z. Chen, X. Du, J. M. Logan, J. Sippel, M. Nikolou, K. Kamaras, J. R. Reynolds, D. B. Tanner, A. F. Hebard, and A. G. Rinzler. Transparent, conductive carbon nanotube films. *Science.*, 305:1273–1276, 2004.

[29] Y. Jia, J. Wei, K. Wang, A. Cao, Q. Shu, X. Gui, Y. Zhu, D. Zhuang, G. Zhang, B. Ma, L. Wang, W. Liu, Z. Wang, J. Luo, and D. Wu. Nanotubesilicon heterojunction solar cells. *Adv. Mat.*, 20:45944598, 2008.

[30] D.l D. Tune, F. Hennrich, S. Dehm, M. F. G. Klein, K. Glaser, A. Colsmann, J. G. Shapter, U. Lemmer, M. M. Kappes, R. Krupke, and B. S. Flavel. The role of nanotubes in carbon nanotubesilicon solar cells. *Adv. Energy Mat.*, 3:1091–1097, 2013.

[31] Del Gobbo S., Castrucci P., Fedele S., Riele L., Convertino A., Morbidoni M., Scarselli M., and Camilli L. De Crescenzi M. Silicon spectral response extension through single wall carbon nanotubes in hybrid solar cells. *J. Mater. Chem. C*, 1:6752–6758, 2013.

[32] V. Lucarini, K. Peiponen, J. J. Saarinen, and E. M. Vartiainen. *Kramers Kronig Relations in Optical Materials Research.* Springer, 2005.

[33] A. Jorio, G. Dresselhaus, and M. S. Dresselhaus. *Carbon Nanotubes: Advanced Topics in the Synthesis, Structure, Properties and Applications.* Springer-Verlag, 2008.

[34] Y.-Z. Ma, L. Valkunas, S. L. Dexheimer, and G. R. Fleming. Ultrafast exciton dynamics in semiconducting single-walled carbon nanotubes. *Mol. Phys.*, 104:11791189, 2006.

[35] M. J. O Connell, S. M. Bachilo, C. B. Huffman, V. C. Moore, M. S. Strano, E. H. Haroz, K. L. Rialon, P. J. Boul, W. H. Noon, C. Kittrell, J. P. Ma, R. H. Hauge, R. B. Weisman, and R. E. Smalley. Band gap fluorescence from individual single-walled carbon nanotubes. *Science*, 297:593–596, 2002.

[36] Y.Z. Ma, C. D. Spataru, L. Valkunas, S. G. Louie, and G. R. Fleming. Spectroscopy of zigzag single walled carbon nanotubes: Comparing femtosecond transient absorption spectra with ab initio calculations. *Phys. Rev. B*, 74:085402, 2006.

[37] Manzoni C., Gambetta A., Menna E., Meneghetti M., Lanzani G., and Cerullo G. Intersubband exciton relaxation dynamics in single-walled carbon nanotubes. *Phys. Rev. Lett*, 94:207401–4, 2005.

[38] F.Wang, G. Dukovic, E. Knoesel, L. E. Brus, and T. F. Heinz. Observation of rapid auger recombination in optically excited semiconducting carbon nanotubes. *Phys. Rev. B*, 70:241403, 2004.

[39] Ma Y-Z., Stenger J., Zimmermann J., Bachilo S.M., Smalley R.E., Weisman R.B., and et al. Ultrafast carrier dynamics in single-walled carbon nanotubes probed by femtosecond spectroscopy. *J. Chem. Phys.*, 120:3368–73, 2004.

[40] L. Luer, S. Hoseinkhani, D. Polli, J. Crochet, T. Hertel, and G. Lanzani. Size and mobility of excitons in (6,5) carbon nanotubes. *Nat. Phys.*, 5:54–58, 2008.

[41] Hertel T. and G. Moos. Electron-phonon interaction in single-wall carbon nanotubes: A time-domain study. *Phys. Rev. Lett.*, 84:5002–5005, 2000.

[42] S.I. Anisimov, B.L. Kapeliovich, and T.L. Perelman. Electron-emission from surface of metals induced by ultrashort laser pulses. *Zh. Eksp. Teor. Fiz.*, 66:776, 1974.

[43] G. Moos, R. Fasel, and T. Hertel. Temperature dependence of electron to lattice energy- transfer in single-wall carbon nanotube bundles. *J. Nanosci. Nanotech*, 3:145–149, 2002.

[44] P. B. Allen. Theory of thermal relaxation of electrons in metals. *Phys. Rev. Lett.*, 59:1460–1463, 1987.

[45] S. Frank, P. Poncharal, Z. L.Wang, and W. A. de Heer. Carbon nanotube quantum resistors. *Science*, 280:17441746, 1998.

[46] Korovyanko O.J., Sheng C-X., Vardeny Z.V., Dalton A.B., and Baughman R.H. Ultrafast spectroscopy of excitons in single-walled carbon nanotubes. *Phys. Rev. Lett*, 92:017403–6, 2004.

[47] Castrucci P., Scilletta C., Del Gobbo S., Scarselli M., Camilli L., Simeoni M., and et al. Light harvesting with multiwall carbon nanotube/silicon heterojunctions. *Nanotechnology*, 22:115701–9, 2011.

[48] Lin M.F., Shyu F.L., and Chen R.B. Optical properties of well-aligned multiwalled carbon nanotube bundles. *Phys. Rev. B*, 61:14114–8, 2000.

[49] Agrawal S., Raghuveer M.S., Ramprasad R., and Ramanath G. Multishell carrier transport in multiwalled carbon nanotubes. *IEEE Trans. Nanotechnol.*, 6:722–6, 2007.

[50] Agrawal S., Raghuveer M.S., Li H., and Ramanath G. . defect-induced electrical conductivity increase in individual multiwalled carbon nanotubes. *Appl. Phys. Lett.*, 90:193104–6, 2007.

[51] Scarselli M., Scilletta C., Tombolini F., Castrucci P., Diociaiuti M., and Casciardi S. Multiwall carbon nanotubes decorated with copper nanoparticles: Effect on the photocurrent response. *Phys. Chem. C*, 113:5860–4, 2009.

[52] Ngo Q., Petranovic D., Krishnan S., Cassell A.M., Ye Q., Li J., and et al. Electron transport through metalmultiwall carbon nanotube interfaces. *IEEE Trans. Nanotechnol.*, 3:311–7, 2004.

[53] Ni C. and Bandaru P.R. Enhanced optical absorption cross-section characteristics of multi-wall carbon nanotubes. *IEEE Trans. Nanotechnol.*, 47:2898–903, 2009.

[54] Bao H., Ruan X., and Fisher T.S. Optical properties of ordered vertical arrays of multi-walled carbon nanotubes from fdtd simulations. *Opt. Express .*, 18:6347–59, 2010.

[55] Lidorikis E. and Ferrari A.C. Photonics with multiwall carbon nanotube arrays. *ACS Nano*, 3:1238–48, 2010.

[56] Kamat P.V. Meeting the clean energy demand: Nanostructure architectures for solar energy conversion. . *J. Phys. Chem. C*, 111:2834–60, 2007.

[57] Jiang K., Li Q., and Fan S. Spinning continuous carbon nanotube yarns. *Nature*, 49:5246–52, 2002.

[58] Diaz J., Paolicelli G., Ferrer S., and Comin F. Separation of the sp3 and sp2 components in the c1s photoemission spectra of amorphous carbon films. *Phys. Rev. B*, 54:8064–9, 1996.

[59] Goldoni A., Larciprete R., Gregoratti L., Kaulich B., Kiskinova M., and et al. X-ray photoelectrion microscopy of the c1s core level of free-standing single-wall carbon nanotubes bundles. *Appl. Phys. Lett.*, 80:2165–7, 2002.

[60] Sette F., Wertheim G.W., Ma Y., Meigs G., Modesti S., and Chen C.T. Lifetime and screening of the c1s photoemission in graphite. *Phys. Rev. B*, 31:9766–70, 1990.

[61] Van Attekum P.M. and Werthein G.K. Excitonic effects in core-hole screening. *Phys. Rev. Lett.*, 43:1896–8, 1979.

[62] Yang D-Q. and Sacher E. Carbon 1s x-ray photoemission line shape analysis of highly oriented pyrolytic graphite: The influence of structural damage on peak aymmetry. *Langmuir*, 22:860–2, 2006.

[63] Ferrari A. and Robertson J. Raman spectroscopy of amorphous, nanostructured, diamond-like carbon, and nanodiamond. *Phyl. Trans. R. Soc. London A*, 362:2477–512, 2012.

[64] Eda B.G., Lin Y.Y., Mattevi C., Yamaguchi H., Chen H.A., Chen I.S., and et al. Blue photoluminescence from chemically derived graphene oxide. advanced materials. *Phyl. Trans. R. Soc. London A*, 22:505–9, 2010.

[65] Kato K., Ishioka K., Kitajima M., Tang J., Saito R., and Petek H. Coherent phonon anisotropy in aligned single-walled carbon nanotubes. *Nano Lett.*, 8:3102–8, 2008.

[66] Hasimoto H., Murakami Y., Maruyama S., and Kono J. Anisotropic decay dynamics of photoexcited aligned carbon nanotube bundles. *Phys. Rev. B*, 75:245408–12, 2007.

[67] Brito-Cruz C.H., Gordon J.P., Becker P.C., Fork R.L., and Shank C.V. Dynamics of spectral hole burning. *IEEE J. Quantum Electron*, 24:261–9, 1988.

[68] Luer L., Crochet J., Hertel T., Cerullo G., and Lanzani G. Ultrafast excitation energy transfer in small semiconducting carbon nanotube aggregates. *ACS Nano*, 4:4265–73, 2010.

[69] Garcia-Vidal F.J., Pitarke J.M., and Pendry J.B. . effective medium theory of the optical properties of aligned carbon nanotubes. *Phys. Rev. Lett.*, 78:4289–92, 1997.

[70] Lu W., Dong J., and Li Z-Y. . optical properties of aligned carbon nanotube systems studied by the effective-medium approximation method. *Phys. Rev. B.*, 63:033401–4, 2000.

[71] Pagliara S., Galimberti G., Mor S., Montagnese M., Ferrini G., Grandi M.S., and et al. Photoinduced p* band gap renormalization in graphite. *J. Am. Chem. Soc.*, 113:6318–22, 2011.

[72] Seibert K., Cho G.C., Kutt W., Kurz H., Reitze D.H., Dadap J.I., and et al. Femtosecond carrier dynamics in graphite. *Phys. Rev. B*, 42:2842–51, 1990.

[73] Anisimov S.I., Kapeliovich B.L., and Perel'man T.L. Electron emission from metal surfaces exposed to ultrashort laser pulses. *Sov. Phys. JETP*, 39:375–7, 1974.

[74] Parrott E.P.J., Zeitler J.A., McGregor J., Oei S-P., Unala H.E., Milne W.I., and et al. The use of terahertz spectroscopy as a sensitive probe in discriminating the electronic properties of structurally similar multi-walled carbon nanotubes. *Adv. Mat.*, 21:3953–7, 2009.

[75] George P.A., Strait J., Dawlaty J., Shivaraman S., Chandrashekhar M., Rana F., and et al. Ultrafast optical-pump terahertz-probe spectroscopy of the carrier relaxation and recombination dynamics in epitaxial graphene. *Nano Lett.*, 8:4248–51, 2008.

[76] Kampfrath T., Von Volkmann K., Aguirre C.M., Desjardins P., Martel R., Krenz M., and et al. Mechanism of the far-infrared absorption of carbon-nanotube films. . *Phys. Rev. Lett.*, 101:267403–6, 2008.

[77] Dawlaty J.M., Shivaraman S.H., Chandrashekhar M.V.S., and Rana F. Spencer M.G. Measurements of ultrafast carrier dynamics in epitaxial graphene. *Appl. Phys. Lett.*, 92:042116–9, 2008.

[78] Newson R.W., Dean J., Schmidt B., and Van Driel H.M. Ultrafast carrier kinetics in exfoliated graphene and thin graphite films. *Opt Expr.*, 17:2326–33, 2009.

[79] Carbone F., Baum P., Rudolf P., and Zewail A.H. Structural preablation dynamics of graphite observed by ultrafast electron crystallography. *Phys. Rev. Lett.*, 100:035501–4, 2008.

[80] Carbone F. The interplay between structure and orbitals in the chemical bonding of graphite. *Chem. Phys. Lett.*, 496:291–5, 2010.

[81] Gambetta A., Manzoni C., Menna E., Meneghetti M., Cerullo G., Lanzani G., and et al. Real-time observation of nonlinear coherent phonon dynamics in single-walled carbon nanotubes. *Nature*, 2:515–20, 2006.

[82] Lim Y-S., Yee K-J., Kim J-H., Haroz E.H., Shaver J., Kono J., and et al. Coherent lattice vibrations in single-walled carbon nanotubes. *Nano Lett*, 6:2696–700, 2006.

[83] Ma Y.Z., Valkunas L., Dexheimer S.L., Bachilo S.M., and Fleming G.R. Femtosecond spectroscopy of optical excitations in single-walled carbon nanotubes: Evidence for exciton-exciton annihilation. . *Phys. Rev. Lett.*, 94:157402–5, 2005.

[84] Valkunas L., Ma Y-Z., and Fleming G.R. Exciton-exciton annihilation in single-walled carbon nanotubes. *Phys. Rev. B*, 73:115432–43, 2006.

[85] Damnjanovic M., Milosevic I., Vukovic T., and Sredanovi R.M. Full symmetry, optical activity, and potentials of single-wall and multiwall nanotubes. . *Phys. Rev. B*, 60:2728–39, 1999.

[86] Murakami Y., Einarsson E., Edamura T., and Maruyamaet S. Polarization dependence of the optical absorption of single-walled carbon nanotubes. *Phys. Rev. Lett.*, 94:087402–5, 2005.

[87] Eda B.G., Lin Y.Y., Mattevi C., Yamaguchi H., Chen H.A., Chen I.S., and et al. Blue photoluminescence from chemically derived graphene oxide. *Advanced Materials*, 22:505–9, 2010.

[88] Beard M.C., Knutsen K.P., Yu P., Luther J.M., Song Q., Metzger W.K., and et al. Multiple exciton generation in colloidal silicon nanocrystals. *Nano Lett.*, 7:2506–12, 2007.

[89] Wang S., Khafizov M., Tu X., Zheng M., and Krauss T.D. Multiple exciton generation in single-walled carbon nanotubes. *Nano Lett.*, 10:2381–6, 2010.

[90] Murakami Y. and Kono J. Existence of an upper limit on the density of excitons in carbon nanotubes by diffusion-limited exciton-exciton annihilation: Experiment and theory. *Phys. Rev. B*, 80:035432–41, 2009.

[91] Shyu F.L. and Lin M.F. Loss spectra of graphite-related systems: A multiwall carbon nanotube, a single-wall carbon nanotube bundle, and graphite layers. *Phys. Rev. B*, 62:8508–16, 2000.

[92] Avouris P. and Chen J. Nanotube electronics and optoelectronics. *Materials Today*, 9:46–54, 2006.

[93] Zheng M. and Semke E.D. Enrichment of single chirality carbon nanotubes. *J. Am. Chem. Soc.*, 129:6084–5, 2007.

[94] Eder D. Carbon nanotube-inorganic hybrids. *Chem. Rev.*, 110:1348–1385, 2010.

[95] G. Ostojic, S. Zaric, J. Kono, V. Moore, R. Hauge, and R. Smalley. Stability of high-density one-dimensional excitons in carbon nanotubes under high laser excitation. *Phys. Rev. Lett.*, 94:097401–4, 2005.

[96] M.S. Dresselhaus, G. Dresselhaus, R. Saito, and A. Jorio. Raman spectroscopy of carbon nanotubes. *Phys. Rep.*, 409:47–99, 2005.

[97] E.F. Antunes, A.O. Lobo, E.J. Corat, V.J. Trava-Airoldi, A.A. Martin, and C. Verissimo. Comparative study of first- and second-order raman spectra of mwcnt at visible and infrared laser excitation. *Carbon*, 44:2202–2211, 2006.

[98] Robertson J. Diamond-like amorphous carbon. *Mater. Sci. Eng.*, 37:129–281, 2002.

[99] Kataura H., Kumazawa Y., Maniwa Y, Umezu I., Suzuki S., Ohtsuka Y., and Achiba Y. Optical properties of single-wall carbon nanotubes. *Synthetic Metals*, 103:2555–2558, 1999.

[100] J.S. Lauret, C. Voisin, G. Cassabois, C. Delalande, Ph. Roussignol, O. Jost, and L. Capes. Ultrafast carrier dynamics in single-wall carbon nanotubes. *Phys. Rev. Lett.*, 90:057404–4, 2003.

[101] G.N. Ostojic, S. Zaric, J. Kono, M.S. Strano, V.C. Moore, R.H. Hauge, and R.E. Smalley. Interband recombination dynamics in resonantly excited single-walled carbon nanotubes. *Phys. Rev. Lett.*, 92:117402–4, 2004.

[102] K. Seibert, G. C. Cho, W. Ktt, H. Kurz, D. H. Reitze, J. I. Dadap, H. Ahn, M. C. Downer, and A. M. Malvezzi. Femtosecond carrier dynamics in graphite. *Phys. Rev. B*, 42:2842–2851, 1990.

[103] L. Luer, G. Lanzani, J. Crochet, T. Hertel, J. Holt, and Z. Valy Vardeny. Ultrafast dynamics in metallic and semiconducting carbon nanotubes. *Phys. Rev. B*, 80:205411–5, 2009.

[104] Borondics F. and Kamaras K. Charge dynamics in transparent single-walled carbon nanotubes films from optical transmission measurements. *Phys. Rev. B*, 74:045431–6, 2006.

[105] M. E. Itkis, D. E. Perea, S. Niyogi, S. M. Rickard, M. A. Hamon, H. Hu, B. Zhao, , and R. C. Haddon. Purity evaluation of as-prepared single-walled carbon nanotube soot by use of solution-phase near-ir spectroscopy. *Nano lett.*, 3:309–314, 2003.

[106] Breusing M., Ropers C., and Elsaesser T. Ultrafast carrier dynamics in graphite. *Phys. Rev. Lett.*, 102:086809–4, 2009.

[107] C. Fantini, A. Jorio, M. Souza, M. S. Strano, M. S. Dresselhaus, and M. A. Pimenta. Optical transition energies for carbon nanotubes from resonant raman spectroscopy: Environment and temperature effects. *Phys. Rev. Lett.*, 93:147406–4, 2004.

[108] J. Hone, B. Batlogg, Z. Benes, A. T. Johnson, and J. E. Fischer. Quantized phonon spectrum of single-wall carbon nanotubes. *Science*, 289:1730–1733, 2000.

[109] R. A. McDONALD. Heat content and heat capacity of an extruded graphite. *journal of chemical and engineering data*, 10:243, 1965.

[110] Z. Wang, D. Psiachos, R. F. Badilla, and S. Mazumdar. Electronelectron interaction effects on the photophysics of metallic single-walled carbon nanotubes. *J. Phys. Condens. Matter*, 21:095009–8, 2009.

[111] T. Winzer, A. Knorr, and E. Malic. Carrier multiplication in graphene. *Nano Lett.*, 12:48394843, 2010.

[112] Brida D, Tomadin A, Manzoni C, Kim YJ, Lombardo A, Milana S, Nair RR, Novoselov KS, Ferrari AC, Cerullo G, and Polini M. Ultrafast collinear scattering and carrier multiplication in graphene. *Nano Lett.*, 12:48394843, 2010.

[113] A. Ueda, K. Matsuda, T. Tayagaki, and Y. Kanemitsu. Carrier multiplication in carbon nanotubes studied by femtosecond pump-probe spectroscopy. *App. Phys. Lett.*, 92:233105, 2008.

[114] Zheng M. and Diner A. Solution redox chemistry of carbon nanotubes. *J. Am. Chem. Soc.*, 126:1549, 2004.

[115] S. Tao, Y. Miyata, K. Yanagi, H. Kataura, and H. Okamoto. Subpicosecond coherent nonlinear optical response of isolated single-walled carbon nanotubes. *Phys. Rev. B*, 80:201405, 2009.

[116] C. Rulliere. *Femtosecond Laser Pulses*. Springer, 2005.

[117] U. Bach, Y. Tachibana, J-E. Moser, S. A. Haque, J. R. Durrant, M. Gratzel, and David R. Klug. Charge separation in solid-state dye-sensitized heterojunction solar cells. *J. Am. Chem. Soc.*, 121:7445–7446, 1999.

[118] A. A. Bakulin, A. Rao, V. G. Pavelyev, P. H. M. van Loosdrecht, M. S. Pshenichnikov, D. Niedzialek, J. Cornil, D. Beljonne, and R. H. Friend. The role of driving energy and delocalized states for charge separation in organic semiconductors. *Science*, 335:13401344, 2012.

[119] A. A. Bakulin, J. C. Hummelen, M. S. Pshenichnikov, and P. H. M. van Loosdrecht. Ultrafast hole-transfer dynamics in polymer/pcbm bulk heterojunctions. *Adv. Funct. Mater*, 20:16531660, 2010.

[120] Li Z., Kunets V. P., Saini V., Xu Y., Dervishi E., Salamo G. J., Biris A. R., and A. S Biris. Light-harvesting using high density p-type single wall carbon nanotube/n-type silicon heterojunctions. *ACS Nano*, 3:1407–1414, 2009.

[121] Wadhwa P., Liu B., McCarthy M., Wu Z., and A. G. Rinzler. Electronic junction control in a nanotube-semiconductor schottky junction solar cell. *Nano Lett.*, 10:5001–5005, 2010.

[122] Robel I., Bunker B. A., and Kamat P. V. Single-walled carbon nanotubecds nanocomposites as light-harvesting assemblies: Photoinduced charge-transfer interactions. *Adv. Materials*, 17:2458–2463, 2005.

[123] X. Y., Yang Q., and Muntwiler M. Charge-transfer excitons at organic semiconductor surfaces and interfaces. *Acc. Chem. Res.*, 42:1779–1787, 2009.

[124] Chew S. Y., Ng S. H., Wang J., Novak P., Krumeich F., Chou S. L., Chen J., and Liu H. K. Flexible free-standing carbon nanotube films for model lithium-ion batteries. *Carbon*, 47:2976–2983, 2009.

[125] Nasibulin A. G., Kaskela A., Mustonen K., Anisimov A. S., Ruiz V., Kivist S., Rackauskas S., and Timmermans M. Y. Pudas M. Aitchison B. et al. Multifunctional free-standing single-walled carbon nanotube films. *ACS Nano*, 5:3214–3221, 2011.

[126] Green M. A. and Keevers M. J. Optical properties of intrinsic silicon at 300 k. *Progress in photovoltaics*, pages 189–192, 1995.

[127] Pekker A. and Kamaras K. A. General figure of merit for thick and thin transparent conductive carbon nanotube coatings. . *J. Appl. Phys.*, 108:054318, 2010.

[128] Pintossi C., Salvinelli G., Drera G., Pagliara S., Sangaletti L., Del Gobbo S., Morbidoni M., Scarselli M., De Crescenzi M., and Castrucci P. Direct evidence of chemically inhomogeneous, nanostructured, si-o buried

interfaces and their effect on the efficiency of cnt/si photovoltaic heterojunctions. *J. Chem. Phys. C.*, 3:1091–1097, 2013.

[129] W. SPITZER and H. Y. FAN. Infrared absorption in n-type silicon. *Phys. Rev.*, 15:268, 1957.

[130] Huang L., Pedrosa H. N., and Krauss. Ultrafast ground-state recovery of single-walled carbon nanotubes. *Phys. Rev. Lett.*, 93:017403–4, 2004.

[131] Schmitt-Rink S., Chemla D. S., and D. A. B. Miller. Theory of transient excitonic optical nonlinearities in semiconductor quantum-well structures. *Phys. Rev. B*, 32:6601–6609, 1985.

[132] Z. Vardeny and J. Tauc. Picosecond coherence coupling in the pump and probe technique. *Optics Comm.*, 39:396–400, 1981.

[133] Doany F. E. and Grishkowsky D. Measurement of ultrafast hot-carrier relaxation in silicon by thin-film-enhanced, time-resolved reflectivity. *Appl. Phys. Lett.*, 52:36–38, 1988.

[134] Jia Y., Cao A., Kang F., Li P., Gui X., Zhang L., Shi E., Wei J., Wang K., Zhu H., and Wu D. Strong and reversible modulation of carbon nanotubesilicon heterojunction solar cells by an interfacial oxide layer. *Chem. Phys.*, 14:83918396, 2012.

[135] Wang C. H.and Misiakos K.and Neugroschel A. Minority-carrier transport parameters in n-type silicon. *IEEE Trans. on electron devices*, ED-37:1314–1322, 1990.